

# From Microscopic Models of Damage Accumulation to the Probability of Failure of Gas Turbines

## Dissertation

submitted to the Faculty of Mathematics and Science



**BERGISCHE  
UNIVERSITÄT  
WUPPERTAL**

By: Nadine Moch

Faculty: School of Mathematics and Science

First Supervisor: Prof. Dr. Hanno Gottschalk

Second Supervisor: Prof. Dr. Matthias Ehrhardt

© 2018

The PhD thesis can be quoted as follows::

urn:nbn:de:hbz:468-20190704-105554-3

[<http://nbn-resolving.de/urn/resolver.pl?urn=urn%3Anbn%3Ade%3Ahbz%3A468-20190704-105554-3>]

DOI: 10.25926/mfaj-nq46

[<https://doi.org/10.25926/mfaj-nq46>]

## Contents

<b>1. Introduction</b>	<b>1</b>
1.1. Motivation and Objectives . . . . .	1
<b>2. Material Structure and Mechanical Behaviour of Polycrystalline Metal</b>	<b>4</b>
2.1. Crystal Structures and Material Characteristics . . . . .	4
2.2. Elastic and Plastic Behaviour of Polycrystalline Metal . . . . .	7
2.2.1. Deformation . . . . .	10
2.2.2. Types of Displacements and Yield Criteria . . . . .	12
2.2.3. Stress-Strain-Relation and Yield Criteria . . . . .	14
2.2.3.1. Von Mises Yield Criterion . . . . .	16
2.2.3.2. Schmid Factors and Modified Yield Criteria . . . . .	21
<b>3. Fatigue</b>	<b>27</b>
3.1. Types of Resistance and Fatigue Testing . . . . .	27
3.2. Experimental Data . . . . .	32
3.2.1. Schmid factors . . . . .	35
3.3. Damage Accumulation . . . . .	37
3.3.1. Rainflow Counting - General and Slip System Based Approach . . . . .	38
3.3.1.1. Slip System Based Rainflow Counting . . . . .	40
<b>4. Mathematical Basics</b>	<b>43</b>
4.1. Stochastical Fundamentals and Haar Measure . . . . .	43
4.2. Recurrence Relations . . . . .	47
<b>5. Grain Orientation and Probabilistic Schmid Factors</b>	<b>49</b>
5.1. Random Grain Orientation and Probabilistic Schmid Factors . . . . .	49
5.1.1. Probabilistic Schmid Factors . . . . .	49
5.2. Anisotropic Elasticity . . . . .	57
5.2.1. Probabilistic Schmid Factor . . . . .	58

# Microscopic Damage Accumulation Models

## *Contents*

---

<b>6. Probabilistic LCF Life for Single Grains</b>	<b>65</b>
6.1. Single Grain Life for fcc Crystals . . . . .	69
<b>7. Crack Propagation and Grain Morphology</b>	<b>78</b>
7.1. Modified Percolation Models . . . . .	80
7.1.1. Recurrence Relation of Crack Probability . . . . .	82
7.2. Approach for Circuit Structures . . . . .	99
7.3. Voronoi Polycrystal Model . . . . .	115
<b>8. Fitting to Experimental LCF Lifetime Data</b>	<b>125</b>
<b>9. Finite Elements Discretization and Transfer to Component</b>	<b>131</b>
9.1. Example: Application to a Blisk-Geometry . . . . .	133
<b>10. Probabilistic Damage Accumulation and Rainflow Counting</b>	<b>137</b>
<b>11. Conclusion and Outlook</b>	<b>147</b>
<b>Bibliography</b>	<b>I</b>
<b>A. Appendix</b>	<b>i</b>
A.1. Further Definitions . . . . .	ii

# 1. Introduction

## 1.1. Motivation and Objectives

The knowledge about the probability of failure plays an important role in the development and safe operation of gas turbine components. They are subject to high mechanical and thermic loads with strongly deviating cyclic loading conditions, since changes from part load to full load or abrupt cold starts are usual. In this context low-cycle fatigue of components is of high relevance.

To estimate the fatigue life, material-specific key figures are required. Therefore, standardized specimen tests are performed to derive strength values or deformation behaviour [1]. The LCF life scatters widely and mechanical components often fail, before the deterministic failure time is reached. Hence, safety factors are applied to consider uncertain or unknown factors such as grain size or local temperature and loading conditions. Thereby, the local grain structure and the relation between loading and grain orientation has the most important physical impact on fatigue life.

There are several statistical studies on fatigue and the underlying causes, see e.g. [25; 17; 11]. In [27; 13], a probabilistic model for low-cycle fatigue life, considering the Ramberg-Osgood and Coffin-Manson-Basquin equation combined with a local hazard approach, was introduced. Additionally, the impact of Schmid factors of the crack initiating grain on LCF was empirically demonstrated and the size effect could be taken into account.

In [12], the modelling approach, using a Poisson process and the local strain field, was also used for notched specimen. With both investigations, the impact of local grain structure and the relation between loading state and grain orientation could not be considered.

A similar stochastic model for the time until crack initiation under high-cycle

# Microscopic Damage Accumulation Models

## 1. Introduction

---

fatigue, using maximum principal stress, was presented in [32]. Physical models for scatter in low-cycle fatigue lifetime were investigated in [9]. The impact of the combination of the statistical and the geometrical size effect on fatigue life for notched specimen was considered in [34].

In this thesis, an approach based on the physical damage mechanisms of Nickel-based superalloys is presented. We investigate the impact of the local grain structure and focus on the size and orientation between grains and loading state. We present a probabilistic LCF life model using probabilistic Schmid factors, where multi-axial loading states and anisotropic elasticity can also be considered. We discuss two different approaches for a percolation model to compute the crack propagation and fatigue, depending on different failure criteria.

The models are statistically validated on real data and the fitted results are applied to the geometry of a Bladed Disk. In addition, an approach is introduced, which allows us to transfer a common cycle counting method, combined with an appropriate damage accumulation assumption to the probabilistic LCF life model.

In chapter 2, we discuss the material characteristics of polycrystalline metal and its elastic and plastic behaviour, in particular with regard to deformation. We closely follow [28; 3].

In chapter 3, we introduce fatigue mechanisms under cyclical loading and show the concept of Wöhler curves and the Coffin-Manson Basquin equation. Then, we give some details on the experimental data, also given in [8]. At the end of the chapter, we show an approach for damage accumulation on slip system level.

In chapter 4, we introduce the mathematical basics to describe the random orientation and give numerical insight to solve the recurrence relation of the percolation models in chapter 7.

In the following chapter 5, probabilistic maximum shear stresses are presented, which are resulting from the random orientation of grains. We show methods to obtain the distributions based on the level of multi-axiality. In addition, anisotropic elasticity is also considered and the results are compared to the isotropic ones.

# Microscopic Damage Accumulation Models

## 1. *Introduction*

---

With the probabilistic shear stress distributions, we calculate probabilistic LCF life for single grains in chapter 6, following [19; 27]. The results for different levels of multi-axiality of the loading states as well as for isotropic and anisotropic elasticity are compared.

We introduce an analytical approach, using a percolation model to simulate the crack propagation within a specimen, in chapter 7. Hereby, different grain morphologies and failure criteria are considered and compared to each other. The model is enlarged to circuit structures to also consider the geometry of specimen. Additionally, we show the probabilistic LCF life for different crack and grain sizes for both models.

Afterwards, a different approach, a Voronoi polycrystal approach, is presented. At the end of the chapter, the results of the analytical and the Voronoi model are compared.

The analytical percolation model is fitted to experimental LCF lifetime data in chapter 8, where we calibrate the parameters of the statistical lifetime distribution with a maximum likelihood method. The results are transferred to a Bladed Disk in chapter 9.

In chapter 10, we present an approach for probabilistic damage accumulation and rainflow counting for variable stress amplitudes. We use the introduced random grain orientation and probabilistic maximum shear stresses. This allows us to also consider loading states with different levels of multi-axiality. We obtain probabilistic damage parameters for these scenarios.

Note that all considered material and test data are either provided by TU Kaiserslautern or by Siemens AG Energy. This work has been supported by the German federal ministry of economic affairs BMWi via an AG Turbo grant, also consider the final report [26] of the corresponding AG Turbo project "Von Mikroskopischen Modellen der Schadensakkumulation zur Ausfallwahrscheinlichkeit von Gasturbinen".

## **2. Material Structure and Mechanical Behaviour**

There are numerous materials having different mechanical properties and therefore with various possible applications. These characteristics result from the arrangement of atoms at which we will look at first. We focus on metals, in particular Nickel, as we are dealing with Nickel-base alloys.

### **2.1. Crystal Structures and Material Characteristics**

As metals are well deformable and can be very resistant when alloyed, they are preferred construction materials, used in many engineering applications. Metals represent a group of solid-states having good thermal and electrical conductivity as well. As it can withstand large fluctuations of temperature as well as high stress levels, it is predestined, amongst other possible applications, for the design of gas turbines.

The kind of bonding of metals is attributable to the fact that they have only few electrons on the outer shell being just weakly bound to individual atoms. The so-called ionisation energy, being the energy with which the least bonded electron is bound to the atom, is low in general. Thus the positively charged atomic cores form a lattice with freely moving valence electrons in between, also referred to as electronic gas. Due to the specific grid structure each atom has a large number of nearest neighbours, which leads to higher bonding energy.

To encourage the spread of the electrons over as many atoms as possible, different kinds of metal form varying periodic crystal structures, which can be understood as three-dimensional grids. The elementary cell is the smallest unit

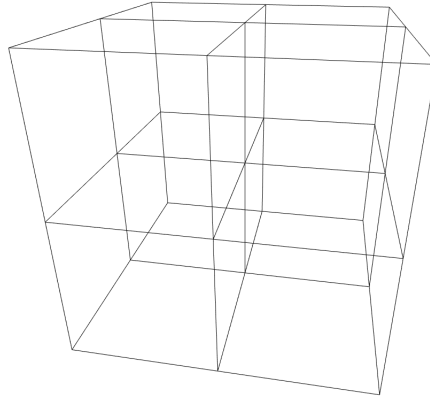


Figure 2.1.: Cubic Crystal System

showing the appropriate characteristic building the crystal. There are 14 kinds of so-called Bravais lattices that are distinguishable from each other by the specific structure and symmetry<sup>1</sup> of their elementary cells, which are the basic components the crystals are consisting of. Figure 2.1 shows the basic lattice structure for cubic crystals.

As we are mainly interested in the mechanical behaviour of Nickel, we especially observe the so-called face centered cubic lattice (fcc). Notwithstanding, other crystal structures are of interest as well, as there are 3 forms being characteristic for metal such as the body centered cubic we look at in the next chapter. In the fcc case there are half atoms at the surfaces of each elementary cell, respectively eighth in the edges being shared with their neighbour cells as noticeable in figure 2.2a and 2.2b.

We focus on a preferred composition of metal in form of a Nickel-base superalloy, which i.e. has a high mechanical strength and a strong resistance to creep at high temperatures. The microstructure is given by the  $\gamma$ -matrix composed of Nickel atoms and various amounts of different chemical elements. The  $\gamma'$ -phase in the form of intermetallic precipitates increases the resistance against dislocations. The kind of composition of chemical elements leads to differing mechanical properties.

---

<sup>1</sup>The symmetry properties are discussed more precisely in chapter 3.

# Microscopic Damage Accumulation Models

## 2. Material Structure and Mechanical Behaviour

---

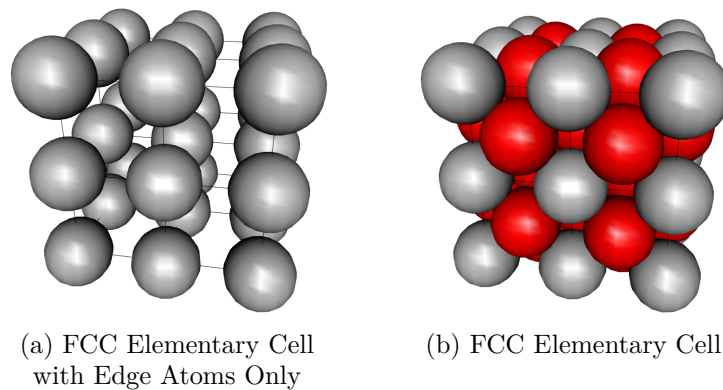


Figure 2.2.: Elementary Cell of a Face Centered Cubic Crystal

Subsequently to melting, the metal is cooled down building crystalized areas also referred to as grains, which sizes depend on the appropriate cooling time. Figures 2.3a and 2.3b show cross sectional areas of metal rods with unequal grain sizes. There are grain boundaries between each grain and its neighbours connecting the areas of different grain orientations and being considered as lattice defects. As well as within these boundaries not every grain shows a complete crystal structure, as vacancies, random replacements of substitution atoms or even more complex dislocations possibly occur. These structural defects are described more precisely in chapter 2.2.1, since they decisively induce deformations.

The chemical composition of the material influences the assorted characteristics of these structural defects directly, wherefore various compounds result in diverging mechanical properties.

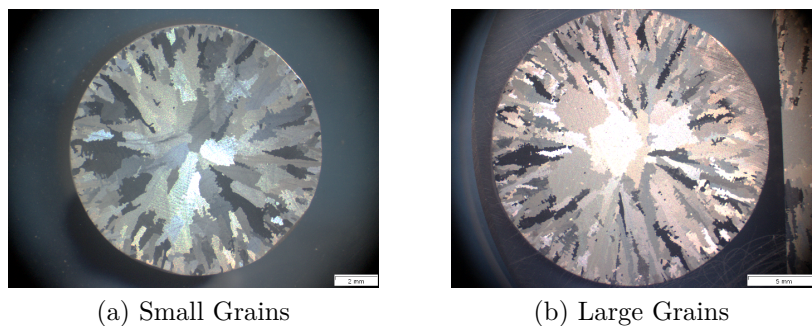


Figure 2.3.: Cross Sectional Area of Metal Rods with Different Grain Sizes, see [8]

## **2.2. Elastic and Plastic Behaviour of Polycrystalline Metal**

Let us consider a metallic component being exposed to an acting force resulting in a relocation of the atoms, on which the mechanical behaviour of the material is depending. At a certain point, the deformation passes from an elastic to a plastic one, which, in contrast to the former case, remains after decreasing the stress again.

Stress and deformation are normalized with regards to length and surface, respectively, to obtain characteristic values, which describe the behaviour and properties of the material. These values can be determined on the basis of experiments with standard specimen and can be transferred to various shapes and sizes of components. The values are specified locally for small volume elements to enable a characterization of fluctuations within the component. We consider a continuum mechanical approach and therewith a size scale comparatively large to the distance of the atoms obtaining continuous values, as the material is regarded as blurred. In the following we follow the presentation in [28; 3].

Let us consider forces acting on the material in form of surface loads  $g$  and volume forces  $f$ . The stress vector at one point of a cross sectional area through the observed subject with force  $\Delta F$  acting on surface  $\Delta A$  is the lower limit of average surface load

$$g = \lim_{\Delta A \rightarrow 0} \frac{\Delta F}{\Delta A} = \frac{dF}{dA}. \quad (2.1)$$

Since the influence of the surface size  $\Delta A$  on  $\Delta F$  is eliminated, one obtains information on the stress at each point locally, as we have described above. The force can be subdivided into normal stress acting perpendicular and shear stress in tangential direction of the surface of the cross section.

In the three-dimensional case the stress state is attained building three cross sections, which is shown for the most simple case in form of those being perpendicular to coordinate axes in figure 2.4.

Therefore consider 3 cross section surfaces  $A_i$ ,  $i = 1, 2, 3$  and the respective forces  $F_j^i$ , where  $j = 1, 2, 3$  represent the components of the force vector. The

# Microscopic Damage Accumulation Models

## 2. Material Structure and Mechanical Behaviour

---

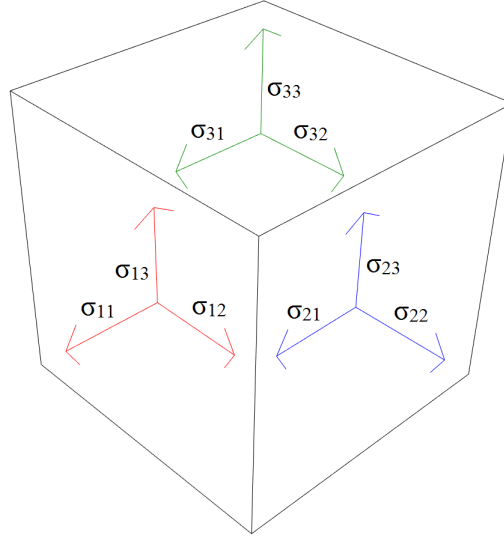


Figure 2.4.: Visualization of the Stress Tensor with its Components

stress values can be calculated via  $\sigma_{ij} = \frac{F_j^i}{A_i}$ , and can be represented in form of a so-called stress tensor  $\sigma$  of second order with

$$\sigma = \begin{pmatrix} \sigma_{11} & \sigma_{12} & \sigma_{13} \\ \sigma_{21} & \sigma_{22} & \sigma_{23} \\ \sigma_{31} & \sigma_{32} & \sigma_{33} \end{pmatrix} \quad (2.2)$$

As  $\sigma_{ij} = \sigma_{ji}$  for  $i, j = 1, 2, 3$ , the stress tensor contains 6 independent components and determines a stress state uniquely for each point. The components of  $\sigma$  give the appropriate stress values with  $i$  standing for the direction of the cross section normal on which the stress acts, which direction in turn is signed by the second index  $j$ . We consider stress vectors  $g_1, g_2$  and  $g_3$  being assigned to these axes and therewith representable via

$$g_j = \sigma_{ji}e_i = \sigma_{j1} \cdot e_1 + \sigma_{j2} \cdot e_2 + \sigma_{j3} \cdot e_3 \quad (2.3)$$

with appropriate basis vectors  $e_i$  for  $i = 1, 2, 3$ . The diagonal entries are the normal stress values and the off-diagonal components are the values of shear stress.

# Microscopic Damage Accumulation Models

## 2. Material Structure and Mechanical Behaviour

---

It can be useful to consider the stress state in a system being rotated from the standard coordinate system, such that the stress vectors  $g_i$  and regarding normal vectors  $n_i$  have the same direction respectively. This form is also regarded as principal axes form with transformed stress tensor

$$\sigma = \begin{pmatrix} \sigma_I & 0 & 0 \\ 0 & \sigma_{II} & 0 \\ 0 & 0 & \sigma_{III} \end{pmatrix} \quad (2.4)$$

containing normal stress only, which simultaneously constitute the extreme values of normal stress of each direction. It is common to arrange the absolute values in a descending order and identify them by Roman numerals, such that  $|\sigma_I| \geq |\sigma_{II}| \geq |\sigma_{III}| \geq 0$ .

As the principal stress values are the eigenvalues of the stress tensor one obtains  $\sigma_I, \sigma_{II}$  and  $\sigma_{III}$  solving

$$\det(\sigma_{ij} - \sigma_e \delta_{ij}) = 0, \quad e = I, II, III, \quad (2.5)$$

where

$$\delta_{ij} = \begin{cases} 1, & \text{if } i = j \\ 0, & \text{if } i \neq j. \end{cases} \quad (2.6)$$

This leads to

$$\sigma_e^3 - I_1 \sigma_e^2 - I_2 \sigma_e - I_3 = 0 \quad (2.7)$$

with

1.  $I_1 = \sigma_{11} + \sigma_{22} + \sigma_{33}$ ,
2.  $I_2 = \sigma_{12}^2 + \sigma_{23}^2 + \sigma_{13}^2 - (\sigma_{11}\sigma_{22} + \sigma_{22}\sigma_{33} + \sigma_{11}\sigma_{33})$ ,
3.  $I_3 = \det(\sigma)$ .

The solutions of equation (2.5) are independent of the coordination system, they are called invariants of the stress tensor. Using principal stress we obtain

1.  $I_1 = \sigma_I + \sigma_{II} + \sigma_{III}$ ,
2.  $I_2 = -(\sigma_I \sigma_{II} + \sigma_I \sigma_{III} + \sigma_{II} \sigma_{III})$ ,
3.  $I_3 = \sigma_I \sigma_{II} \sigma_{III}$ .

# Microscopic Damage Accumulation Models

## 2. Material Structure and Mechanical Behaviour

---

### 2.2.1. Deformation

Having introduced some basic technical terms and designations regarding stress we focus on the dependencies between stress and according deformation, especially for the case of polycrystalline metal.

Therefore, let us consider the shape of a mechanical component made of polycrystalline metal in form of a bounded region  $\Omega \subseteq \mathbb{R}^3$  with boundary  $\partial\Omega$  and closure  $\bar{\Omega}$ . As mentioned at the beginning of chapter 2.2, we consider forces  $f : \Omega \rightarrow \mathbb{R}^3$  in form of external loads spread over volume  $\Omega$  as well as surface loads  $g : \partial\Omega \rightarrow \mathbb{R}^3$ .

These forces result in a deformation represented by  $u : \bar{\Omega} \rightarrow \mathbb{R}^3$  being also referred to as displacement field with according stress tensor  $\sigma : \Omega \rightarrow \mathbb{R}^{3 \times 3}$ , whereas we assume the component to be fixed at some points,  $u(x) = 0$ ,  $x \in \partial\Omega_D \subseteq \Omega$ .

For the (linearized) strain tensor  $\epsilon : \Omega \rightarrow \mathbb{R}^{3 \times 3}$  describing the displacements relatively when external loads are applied to the component it holds that

$$\epsilon_{ij} = \frac{1}{2} \left( \frac{\partial u_i}{\partial x_j} + \frac{\partial u_j}{\partial x_i} \right) \quad (2.8)$$

and therewith  $\epsilon_{ij} = \epsilon_{ji}$ ,  $i, j = 1, 2, 3$ . Thereby the strain tensor is symmetric as well and contains 6 independent strain components. In the uniaxial case the relation between strain and according perpendicular strain is given by Poisson ratio  $\nu$ , which is a material specific constant, via

$$\epsilon_{per} = -\nu\epsilon. \quad (2.9)$$

Obviously, stress and strain tensors are closely connected to each other and one can note that stress can result in strain in normal direction as well as in perpendicular strain. So, each component of  $\sigma$  influences several components of  $\epsilon$ . Since we consider linear elastical material and small displacements only, the following relationship holds for multiaxial stress states

$$\sigma_{ij} = C_{ijkl}\epsilon_{kl} = C_{ij11}\epsilon_{11} + C_{ij12}\epsilon_{12} + C_{ij13}\epsilon_{13} + C_{ij21}\epsilon_{21} + \dots + C_{ij33}\epsilon_{33}, \quad (2.10)$$

# Microscopic Damage Accumulation Models

## 2. Material Structure and Mechanical Behaviour

---

where  $C$  is the so-called elasticity tensor of fourth order, which describes the stiffness of the material containing material depending characteristic values for the elastic behaviour. We also applied Einstein's convention on summation. The components of the elasticity tensor can also be calculated via

$$C_{ijkl} = \frac{\partial \sigma_{ij}}{\partial \epsilon_{kl}}. \quad (2.11)$$

The elasticity tensor consists of  $9^2 = 81$  components, whereas  $6^2 = 36$  of them are independent due to these symmetry properties. Therefore we can use a simplified matrix notation, which is known as the Voigt notation, where  $(\sigma_\alpha) = (\sigma_{11}, \sigma_{22}, \sigma_{33}, \sigma_{23}, \sigma_{13}, \sigma_{12})$  and  $(\epsilon_\beta) = (\epsilon_{11}, \epsilon_{22}, \epsilon_{33}, \gamma_{23}, \gamma_{13}, \gamma_{12})$ , such that we obtain

$$\begin{pmatrix} \sigma_{11} \\ \sigma_{22} \\ \sigma_{33} \\ \sigma_{23} \\ \sigma_{13} \\ \sigma_{12} \end{pmatrix} = \begin{pmatrix} C_{11} & C_{12} & C_{13} & C_{14} & C_{15} & C_{16} \\ C_{12} & C_{22} & C_{23} & C_{24} & C_{25} & C_{26} \\ C_{13} & C_{23} & C_{33} & C_{34} & C_{35} & C_{36} \\ C_{14} & C_{24} & C_{34} & C_{44} & C_{45} & C_{46} \\ C_{15} & C_{25} & C_{35} & C_{45} & C_{55} & C_{56} \\ C_{16} & C_{26} & C_{36} & C_{56} & C_{56} & C_{66} \end{pmatrix} \cdot \begin{pmatrix} \epsilon_{11} \\ \epsilon_{22} \\ \epsilon_{33} \\ \gamma_{23} \\ \gamma_{13} \\ \gamma_{12} \end{pmatrix} \quad (2.12)$$

where  $\gamma_{ij} = 2\epsilon_{ij}$  and matrix  $C_{\alpha,\beta}$ .

If we consider the material to be isotropic, i.e. having equivalent mechanical properties in each direction, the components of the elasticity matrix need to be invariant under rotations.  $C_{\alpha,\beta}$  as given in (2.12), can be reduced due to the invariance under rotations using the isotropy assumption, as the mechanical properties are then equal in all directions. We obtain

$$C_{\alpha,\beta} = \begin{pmatrix} C_{11} & C_{12} & C_{12} & 0 & 0 & 0 \\ C_{12} & C_{11} & C_{12} & 0 & 0 & 0 \\ C_{12} & C_{12} & C_{11} & 0 & 0 & 0 \\ 0 & 0 & 0 & C_{44} & 0 & 0 \\ 0 & 0 & 0 & 0 & C_{44} & 0 \\ 0 & 0 & 0 & 0 & 0 & C_{44} \end{pmatrix} \quad (2.13)$$

where

$$C_{44} = \frac{C_{11} - C_{12}}{2}. \quad (2.14)$$

# Microscopic Damage Accumulation Models

## 2. Material Structure and Mechanical Behaviour

---

For a more common notation we introduce the material related Lamé coefficients  $\mu$  and  $\lambda$  with

$$\mu = \frac{E}{2(1 + \nu)}, \quad \lambda = \frac{E\nu}{(1 + \nu)(1 - 2\nu)}, \quad (2.15)$$

where  $E$  is the elasticity module, indicating the stiffness of the material, and Poisson ratio  $\nu$ . In the isotropic linear case it holds that

$$\sigma_{ij} = \lambda \epsilon_{kk} \delta_{ij} + 2\mu \epsilon_{ij}, \quad (2.16)$$

so

$$\sigma = \lambda \text{tr}(\epsilon) I + 2\mu \epsilon. \quad (2.17)$$

Conversly, it holds that

$$\epsilon = -\frac{\nu}{E} \text{tr}(\sigma) I + \frac{1 + \nu}{E} \sigma, \quad (2.18)$$

where we use the definition of Lamé coefficients as given in A.6.

For a face-centered cubic crystal structure the material constants for a single crystal in general depend on its orientation<sup>2</sup> as it is the case for most crystal types. The constants are then identified by additional indices [3].

We consider polycrystalline metals and in general a large number of grains in comparison to the size of the component with each grain showing a random orientation, many effects of anisotropic properties are compensated looking at the component in total. As this is not always the case, we will introduce an approach for including possible anisotropic effects of medium and large sized grains in chapter 5.2.

### 2.2.2. Types of Displacements and Yield Criteria

Before investigating the different possibilities and criteria to identify dislocation motions, some basics on mechanical resistance are introduced. The aim is to make use of relocation mechanisms and their load depending triggers

---

<sup>2</sup>The material is anisotropic.

# Microscopic Damage Accumulation Models

## 2. Material Structure and Mechanical Behaviour

---

to specify appropriate yield criteria and to recognize serious damage of mechanical components. To obtain yield criteria, which will be introduced in the following subsection, it is necessary to determine specific conditions. We subdivide deformations into plastical and elastical parts, whereas the former ones are irreversible in controvension to the latter.

As plastical deformations are accompanied by relocations of atoms or even entire atom layers, the crystal structure types are of great importance. Mainly due to the existence of these (linear) lattice defects being either screw or edge dislocations, irreversible distortions occur which eventually lead to damage of a component.

A dislocation can be identified by its line vector  $t$  in the direction of the dislocation line and by its Burger vector  $b$ .

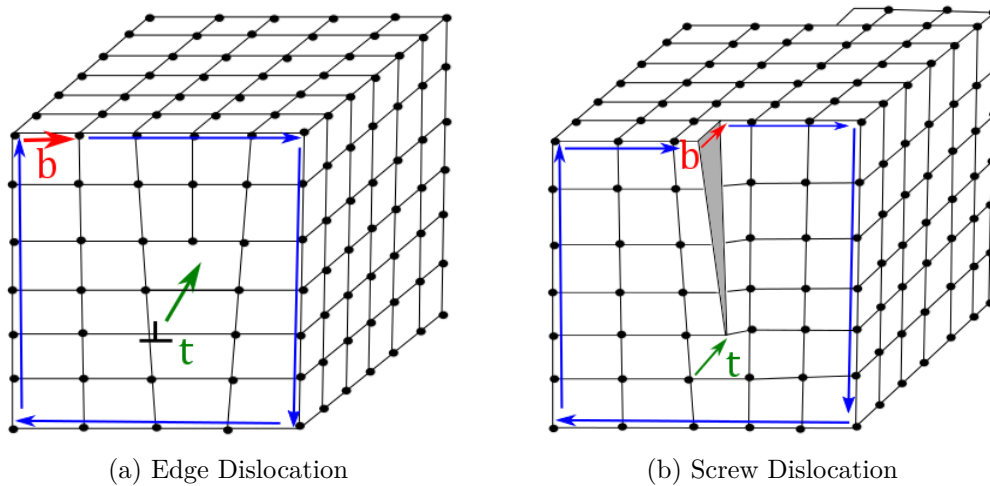


Figure 2.5.: Dislocation Types with Burger and Line Vector

Drawing a circulation line around the distortion line with same length in each grid direction, the Burger vector is the counterpart, which is missing to complete the circle as identified by the red arrow in figure 2.5a and 2.5b.

Edge dislocation can be characterized by an additional half plane included at one side of the chrystal. Screw dislocations, which are named as such as the path of dislocation line has the form of a screw, can be understood as a slipping of atom layers against each other by an atom distance at one side of the dislocation line.

In contrast to the former distortion type Burger and line vector of a screw dislocation are parallel to each other, edge dislocations Burger and line vectors are orthogonal.

## Microscopic Damage Accumulation Models

### 2. Material Structure and Mechanical Behaviour

---

There are hybrids of both distortion types and in general, the dislocation line is much more complex and changes its direction several times moving through the crystal, wherefore the line vector direction varies locally. As the Burger vector remains unchanged, the angles between them differ from  $0^\circ$  to  $90^\circ$ .

Shear stresses acting on a dislocation in a sufficient strength lead to disbalances of the atoms within the distortion area and result in replacing of the binding partner as atom distances change and bondings turn over. Under further load this procedure is repeated and moves through the crystal until the dislocation reaches the surface, i.e. the crystal is deformed plastically.

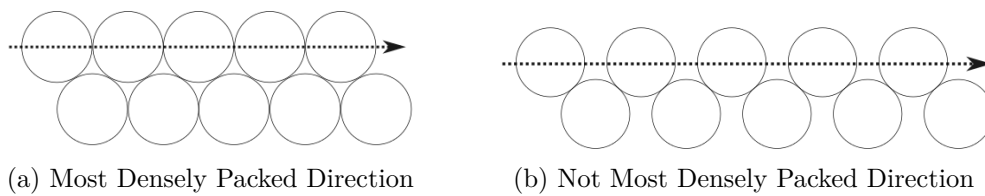


Figure 2.6.: Differences between Densely and Not Densely Packed Atom Layers

The lowest energy starting these mechanisms is needed in direction of the most densely packed atom layers, such that less stress is needed in comparison to other directions to enable slipping and therefore deformations.

Section 2.2.3.2 deepens the understanding of these mechanisms and methodologies. We show how to advance common approaches introduced in the next section to obtain a more appropriate yield criterion for detecting and evaluating possible dislocations.

### 2.2.3. Stress-Strain-Relation and Yield Criteria

It is common to carry out material tests to obtain the so-called stress-strain diagrams showing the relation between stress and strain. In figure 2.7, we consider uniaxial loading with  $\sigma_I > 0$  and  $\sigma_{II} = \sigma_{III} = 0$ . A strain level of 0.2 % is considered to be the last value before unacceptable irreversible strain occurs, of which the corresponding stress value is also referred to as yield

# Microscopic Damage Accumulation Models

## 2. Material Structure and Mechanical Behaviour

---

strength  $R_{p0.2}$ . Up to this point the relation can be described by a line having a slope for small strains, which is equal to the elasticity coefficient  $E$ .

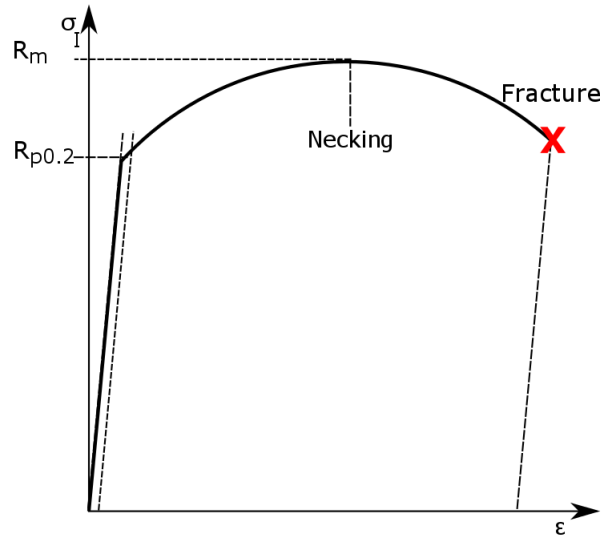


Figure 2.7.: Relation between Stress and Strain

To obtain the exact yield stress value including the fact that the atoms reorder, if strain increases such that plastic deformations occur, the elastical line is shifted by 0.2%. As one can note the relation changes beginning from this point and stress increases flatly up to a maximum  $R_m$ . Beyond this ultimate tensile strength growing neckings at the specimen can be observed resulting in a fracture at  $\epsilon = A$ , also called elongation. Though the stress decreases as it is obtained with regards to the starting prepositions, it locally increases, as the cross sectional area of the specimen becomes smaller.

Considering a polycrystalline metal rod with an isotropic material behaviour, on which uniaxial forces are acting, we assume to obtain plastic deformation approximately, when reaching the yield criterion

$$\sigma_I - R_p = 0. \quad (2.19)$$

For cases of multiaxial stress states we need a reference value to compare the strength of stress to an uniaxial loading state and therewith check whether the

# Microscopic Damage Accumulation Models

## 2. Material Structure and Mechanical Behaviour

---

critical value for plastical deformation is exceeded. In engineering it is common to use an equivalent stress  $\sigma_v$  of the stress tensor, such that

$$f(\sigma) = \sigma_v(\sigma) - \sigma_{yield} = 0. \quad (2.20)$$

Considering the principal stress (2.4) of the stress tensor ordered in a descending way we obtain

$$f(\sigma_I, \sigma_{II}, \sigma_{III}) = 0 \quad (2.21)$$

as flow condition of the material. Consider the situation where the loads switch from state  $\sigma_1$  to load state  $\sigma_2$  periodically, i.e. showing a cyclic behaviour. The according stress amplitude with respect to equivalent stress is

$$\sigma_a = \frac{1}{2} (\sigma_v(\sigma_1) - \sigma_v(\sigma_2)). \quad (2.22)$$

For the purpose of describing the connection between strain and stress according to a given stress amplitude we use the following relation:

**Definition 2.1** (Ramberg-Osgood Equation). *Let  $E$  be the elasticity module of some material with strain hardening coefficient  $K$  and strain hardening exponent  $n$ . The Ramberg-Osgood equation representing the relation between stress and strain with regards to its material constants is defined by*

$$\epsilon_a = RO(\sigma_a) = \frac{\sigma_a}{E} + \left(\frac{\sigma_a}{K}\right)^{\frac{1}{n}}. \quad (2.23)$$

The right handside of the Ramberg-Osgood equation shows the composition of an elastical part and a plastical part, where the former one can be neglected considering large deformations only. The strength of plastical deformation before fracturing is characterized by its ductility, the height of stress by hardening respectively.

### 2.2.3.1. Von Mises Yield Criterion

To investigate the close form of the yield criterion and its usefulness regarding multiaxial loading states we focus on the conditions resulting in deformation first and closely follow von Mises' shape modification hypothesis.

Within one grain plastical deformation is caused by slipping of the atomic

## Microscopic Damage Accumulation Models

### 2. Material Structure and Mechanical Behaviour

---

layers, wherefore the order of atoms and the crystal structure type are important for the elastical and plastical behaviour. Hydrostatical stress, i.e. where  $\sigma_1 = \sigma_2 = \sigma_3$  does not lead to a relocation of atoms and therewith to plastical deformation. As only stress differences compared to the resulting hydrostatical axis leads to shearing within the material, the stress tensor can be reduced by its hydrostatical part

$$\sigma_h = \frac{1}{3}(\sigma_{11} + \sigma_{22} + \sigma_{33}). \quad (2.24)$$

We obtain the so-called stress deviator

$$\sigma' = \sigma - \sigma_h \cdot \delta_{ij}, \quad i, j = 1, 2, 3, \quad (2.25)$$

which means considering principal stress

$$\begin{pmatrix} \sigma'_I & 0 & 0 \\ 0 & \sigma'_{II} & 0 \\ 0 & 0 & \sigma'_{III} \end{pmatrix} = \begin{pmatrix} \sigma_I & 0 & 0 \\ 0 & \sigma_{II} & 0 \\ 0 & 0 & \sigma_{III} \end{pmatrix} - \begin{pmatrix} \sigma_h & 0 & 0 \\ 0 & \sigma_h & 0 \\ 0 & 0 & \sigma_h \end{pmatrix}. \quad (2.26)$$

The invariants, that we introduced in (2.2), can be calculated for the stress deviator as well. To distinguish between the invariants of the stress tensor and the stress deviator we use  $I'_1, I'_2, I'_3$  instead of  $I_1, I_2, I_3$ . Thus the first invariant of the stress deviator (compare (2.2))  $I'_1$  is equal to zero, as

$$I'_1 = (\sigma_I - \sigma_h) + (\sigma_{II} - \sigma_h) + (\sigma_{III} - \sigma_h) = 0 \quad (2.27)$$

Noting that the stress deviator is symmetric as well it holds for the second invariant that

$$\begin{aligned} I'_2 &= \frac{1}{2} \sigma'_{ij} \sigma'_{ji} \\ &= \frac{1}{2} [(\sigma_{11} - \sigma_h)^2 + (\sigma_{22} - \sigma_h)^2 + (\sigma_{33} - \sigma_h)^2 + 2\sigma_{12}^2 + 2\sigma_{13}^2 + 2\sigma_{23}^2] \\ &= \frac{1}{3} [\sigma_{11}^2 + \sigma_{22}^2 + \sigma_{33}^2 - (\sigma_{11}\sigma_{22} + \sigma_{11}\sigma_{33} + \sigma_{22}\sigma_{33})] + \sigma_{12}^2 + \sigma_{13}^2 + \sigma_{23}^2 \end{aligned} \quad (2.28)$$

Considering the deviator in the principal axes form we have

$$I'_2 = \frac{1}{6} [(\sigma_I - \sigma_{II})^2 + (\sigma_I - \sigma_{III})^2 + (\sigma_{II} - \sigma_{III})^2]. \quad (2.29)$$

## Microscopic Damage Accumulation Models

### 2. Material Structure and Mechanical Behaviour

---

To evaluate the influence of a multiaxial stress scenario it is a very frequent practice in engineering to calculate equivalent tensile stress from  $\sigma$  to obtain a comparable value for a yield strength of an uniaxial loading case.

Considering von Mises' shape modification hypothesis the material is assumed to be deformed when the second invariant of the stress deviator reaches a given yield stress, which is related to the former introduced yield criterion  $R_p$  (see (2.19)).

The yield criterion in the von Mises case takes the following form

$$f(I'_2) = I'_2 - k_f^2 = 0 \quad (2.30)$$

with a material depending constant  $k_f$ .

The equivalent stress therewith is defined by

$$\sigma_v = \sqrt{\frac{1}{6} [(\sigma_I - \sigma_{II})^2 + (\sigma_I - \sigma_{III})^2 + (\sigma_{II} - \sigma_{III})^2]}. \quad (2.31)$$

Considering an uniaxial stress state with strength of the yield offset  $R_p$ , i.e.  $\sigma_{II} = \sigma_{III} = 0$  and  $\sigma_I = R_p$  the von Mises yield criterion

$$\sqrt{\frac{1}{6} [(\sigma_I - \sigma_{II})^2 + (\sigma_I - \sigma_{III})^2 + (\sigma_{II} - \sigma_{III})^2]} = k_f \quad (2.32)$$

becomes

$$k_f = \sqrt{\frac{2R_p^2}{6}} = \frac{R_p}{\sqrt{3}}. \quad (2.33)$$

Thus the yield criterion is reached if it holds that

$$\sqrt{\sigma'_{ij}\sigma'_{ji}} = \sqrt{\frac{2}{3}} R_p. \quad (2.34)$$

Figure 2.8 shows the appropriate yield surface in case of von Mises equivalent stress. It can be visualized via a cylinder around the hydrostatic axis, i.e. where  $\sigma_I = \sigma_{II} = \sigma_{III}$  and radius  $r = \sqrt{\frac{2}{3}} \cdot R_p$ . The axes are used according to the principal stress system.

# Microscopic Damage Accumulation Models

## 2. Material Structure and Mechanical Behaviour

---

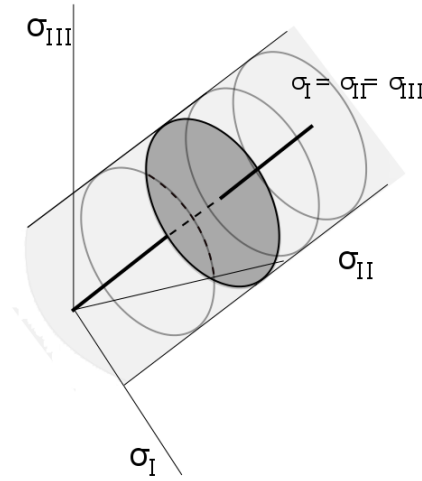


Figure 2.8.: Von Mises Yield Surface as Cylinder around  $\sigma_h I$  with  $r = \sqrt{\frac{2}{3}} R_p$

The following definition shows the possibility of another version for equation (2.34).

**Definition 2.2.** *The Frobenius norm (being also referred to as Hilbert-Schmid norm) of  $A \in \mathbb{R}^{3 \times 3}$  is defined by*

$$\|A\|_F = \sqrt{\sum_{i,j=1}^3 |a_{ij}|^2}. \quad (2.35)$$

As the stress deviator is symmetric and therewith we can write

$$\sqrt{\sigma'_{ij} \sigma'_{ji}} = \sqrt{\sum_{i,j=1}^3 |\sigma'_{ij}|^2} = \|\sigma'\|_F, \quad (2.36)$$

the yield criterion is fulfilled if

$$\|\sigma'\|_F = \sqrt{\frac{2}{3}} R_p. \quad (2.37)$$

There are many combinations of  $\sigma'_I, \sigma'_{II}, \sigma'_{III}$  fulfilling the yield criterion, such that for the appropriate stress tensors equation (2.37) holds.

# Microscopic Damage Accumulation Models

## 2. Material Structure and Mechanical Behaviour

---

Let  $\sigma_h$  be fixed. Then the set of possible stress can be visualized by a slice out of the cylinder around the hydrostatic axis being coloured in darker grey as shown in figure 2.8. For each point on the outer line of the circle standing for a combination of principal stress with coordinates on the circle line equation (2.37) holds.

Let  $R_p = 1$ , then the set of combinations of principal stress according to equation (2.34) can as well be illustrated by a ball with  $r = \sqrt{\frac{2}{3}}$  (Figure 2.9). Considering the stress deviator resulting in deformation only in accordance to the von Mises shape modification hypothesis, principal stress combinations are regarded, where (Compare equation 2.27)

$$I'_1 = \sigma'_I + \sigma'_{II} + \sigma'_{III} = 0. \quad (2.38)$$

Therewith a plane exists intersecting the ball, whose resulting circle line contains all possible stress vectors. The von Mises yield strength criterion does not take into account the relation between  $\sigma'_I, \sigma'_{II}$  and  $\sigma'_{III}$ , wherewith the differences between principal stress are neglected. All points of the intersection lead to the same result of equivalent von Mises stress and are ranked as equals.

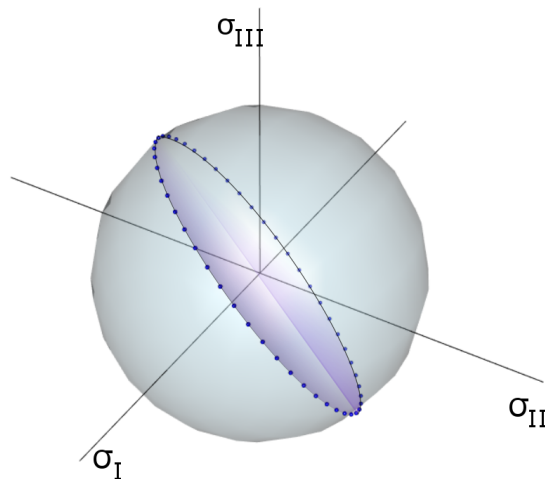


Figure 2.9.: Intersection of Deviatoric Plane and Sphere with  $\|\sigma'\|_F = \sqrt{\frac{2}{3}}$

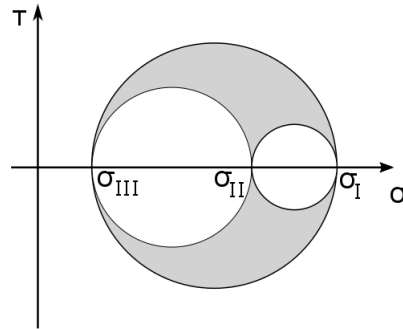


Figure 2.10.: Mohr's Circles characterizing Possible Shear and Normal Stress Combinations

### 2.2.3.2. Schmid Factors and Modified Yield Criteria

As the diversity of solutions is ignored using the resulting equivalent tensile stress only, we now introduce an alternative approach of yield criteria.

According to (2.4) consider a stress state described in terms of principal stress  $\sigma_I, \sigma_{II}, \sigma_{III}$ .

As only shear stress leads to deformation only and the fact that principal stress constitute the extreme values of normal stress of each direction, we can easily calculate maximum shear stress as follows:

$$\tau_{max} = \frac{\sigma_I - \sigma_{III}}{2}, \quad (2.39)$$

which closely relates to Tresca shear stress hypothesis [See 3.3.2, [3]] with yield criterion

$$\sigma_v = \sigma_I - \sigma_{III} = R_p. \quad (2.40)$$

Thus the flow condition is

$$\tau_{max} = \tau_{crit}. \quad (2.41)$$

Figure 2.10 shows the the valid range of normal and shear stress being identified by the grey coloured area and makes the calculation of maximum shear stress regarding (2.39) easily recognizeable. This hypothesis considers the differences of principal stress, but the height of the middle stress  $\sigma_{II}$  is ignored. Our aim is to introduce an approach with accords to the shear stress resulting from different loading states, which acts on the different densely packed atom layers depending on the appropriate crystal structure type. First we have a look at

# Microscopic Damage Accumulation Models

## 2. Material Structure and Mechanical Behaviour

---

the standard case in form of an uniaxial loading state and then continue with the specific characteristics and a possible parametrization for multiaxial stress scenarios.

At first we consider a crystal with face centered cubic lattice (fcc) which means we have a cubic lattice with one eighth of an atom at each edge and half atoms centered in each face.

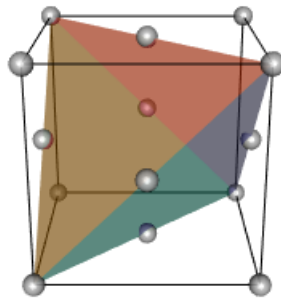


Figure 2.11.: FCC Crystal

As introduced in the beginning of this section dislocation begin to move through the crystal once a sufficient shear stress value is reached. Looking at the structure (Compare figure 2.2a) of a face-centered cubic elementary cell it is obvious in which way the atoms can be relocated under forces involved, namely along the planes of most dense packages. Those are equal to the so-called slip planes being 4 in this case and forming a tetrahedron which is shown in figure 2.11. There are 3 possibilities of slip directions for each slip plane, as two different edges build one slip system. The figure shows an unit cell of a crystal with appropriate slip planes and systems.

Let us consider  $n_i$  to be the normal of slip plane  $i$ ,  $i = 1, \dots, 4$  and  $s_{i,j}$ ,  $j = 1, 2, 3$  the  $j$ -th slip system related to slip plane  $i$ . In the following we consider both vectors to be unit vectors.

Let  $F$  be the vector in direction of tensile stress identified by the dashed line in figure 2.12 and consider the axes of  $x_1$  being parallel to  $F$ . The blue surface

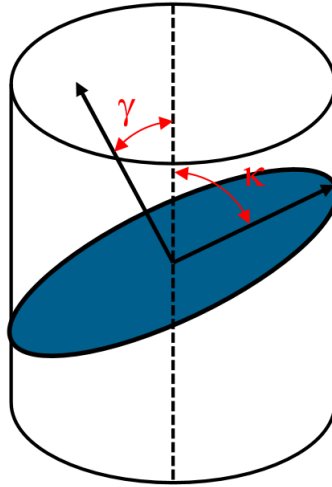


Figure 2.12.: Impact of Tensile Stress on a Slip System

represents an arbitrary slip plane of the crystal with normal vector  $n_i$  and slip direction  $s_{ij}$ . The stress tensor is given by

$$\sigma = \begin{pmatrix} \sigma_I & 0 & 0 \\ 0 & 0 & 0 \\ 0 & 0 & 0 \end{pmatrix}. \quad (2.42)$$

The shear stress acting on the slip plane in direction of  $s_{ij}$  is calculated via

$$\tau_{ij} = n_i \cdot \sigma \cdot s_{ij}. \quad (2.43)$$

As one can note on figure 2.12, for unit vectors  $n_i$  and  $s_{ij}$ , as considered above, and  $\sigma$  as defined, we obtain

$$\tau_{ij} = \sigma_I \cdot \cos \gamma \cos \kappa. \quad (2.44)$$

So in the case of an uniaxial loading state the Schmid factor or rather the conversion factor of normal stress to shear stress for a slip system shear stress can be expressed by

$$\begin{aligned} \frac{\tau_{ij}}{\sigma_I} &= n_{i,1} \cdot s_{ij,1} \\ &= \cos \kappa \cos \gamma. \end{aligned} \quad (2.45)$$

## Microscopic Damage Accumulation Models

### 2. Material Structure and Mechanical Behaviour

---

Obviously the factor reaches its maximum value being 0.5 under forces acting in direction  $45^\circ$  to the slip system. In the following we will rather use the term maximum shear stress than Schmid factor to avoid confusion as there is no one to one transfer possible in the multiaxial loading case. In the following we always consider  $\sigma$  to be normalized, such that we can use  $\tau$  directly as shear stress value.

In the general case shear stress in direction of a slip system  $s_{i,j}$ ,  $i = 1, \dots, 4$ ,  $j = 1, 2, 3$  given the stress tensor  $\sigma$  can be calculated as in 2.43. As the crystal structure type and according slip systems determine the number of shear stress values, there are 12 shear stresses in case of a face-centered cubic crystal. A dislocation begins to move through the crystal when a critical value  $\tau_{crit}$  (or  $R_p$ ) is reached, i.e.

$$\tau_{i,j} = \tau_{crit}. \quad (2.46)$$

So we follow a shear stress based yield criterion approach on slip system level. As for a one-time loading the slip system experiencing maximum shear stress reaches the critical value first and therewith may activate an ongoing dislocation, we consider

$$\tau = \max_{i,j} |\tau_{i,j}| \quad (2.47)$$

as a comparison value to the critical one

Let us consider three-dimensional loading conditions comprising stresses in normal directions and shear stresses in all directions of space. We see in equation 2.2.3.2 that depending on the crystal structure type and therewith the number of slip systems there are various different shear stress values resulting from one loading state. As the deviatoric principal stress tensors are sorted according to their absolute size (compare (2.4)), for uniaxial tensile stress  $\sigma_I$  it holds that

$$\begin{pmatrix} \sigma'_I & 0 & 0 \\ 0 & \sigma'_{II} & 0 \\ 0 & 0 & \sigma'_{III} \end{pmatrix} = \begin{pmatrix} \sigma_I - \sigma_h & 0 & 0 \\ 0 & -\sigma_h & 0 \\ 0 & 0 & -\sigma_h \end{pmatrix} = \begin{pmatrix} \frac{2}{3}\sigma_I & 0 & 0 \\ 0 & -\frac{1}{3}\sigma_I & 0 \\ 0 & 0 & -\frac{1}{3}\sigma_I \end{pmatrix}. \quad (2.48)$$

It is noticeable that the yield criterion according to equation (2.37) is fulfilled for  $\sigma_I = R_p$ , as

$$\left\| \begin{pmatrix} \frac{2}{3}\sigma_I & 0 & 0 \\ 0 & -\frac{1}{3}\sigma_I & 0 \\ 0 & 0 & -\frac{1}{3}\sigma_I \end{pmatrix} \right\| = \sqrt{\frac{2}{3}}\sigma_I. \quad (2.49)$$

# Microscopic Damage Accumulation Models

## 2. Material Structure and Mechanical Behaviour

---

To have a ratio between maximum shear stress and the applied principal stress, we introduce the alternative Schmid factor

$$m := \frac{\tau}{\sqrt{3/2} \cdot \|\sigma'\|_F}, \quad (2.50)$$

where the denominator results from the comparison of von Mises equivalent stress to the yield point  $R_p$ , which is given in equation (2.37).

So in the case where we normalize the stress deviator to  $\sqrt{\frac{2}{3}}$ , we can use  $\tau$  directly.

We introduce the parameter  $\kappa \in [0, 1]$  to measure the ratio of multiaxiality,

$$\kappa = \frac{|\sigma'_{III} - \sigma'_{II}|}{|\sigma'_I|}, \quad (2.51)$$

which is equal to zero in the uniaxial loading state, i.e. if  $\sigma'_{II} = \sigma'_{III}$ . Parameter  $\kappa = 1$  holds, if the absolute stress difference between  $\sigma_{II}$  and  $\sigma_{III}$  is equal to  $|\sigma_I|$ , which is illustrated in figure 2.13. As one can note this is the case for principal stresses with the same strength but different sign. The possible

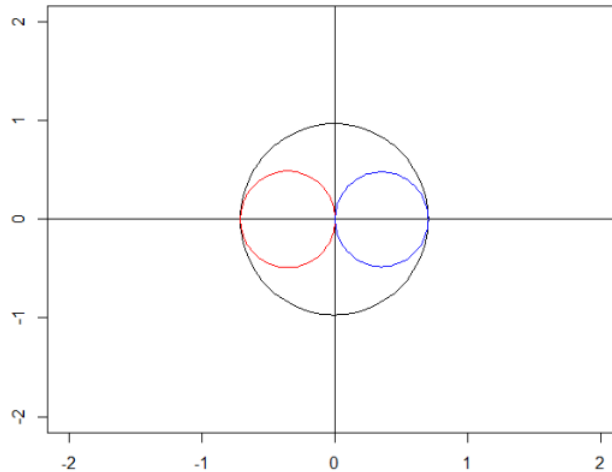


Figure 2.13.: Mohr circles for  $\kappa = 1$

combinations of principal stress values are on the intersection of the deviatoric plane and the cylinder given by the constant equivalent stress condition, shown in figure 2.9. All values on the circle have an equal an constant equivalent stress value and consist of deviatoric parts only. The sphere represents the case, where  $\|\sigma'\|_F = \sqrt{\frac{2}{3}}$ .

# Microscopic Damage Accumulation Models

## 2. Material Structure and Mechanical Behaviour

---

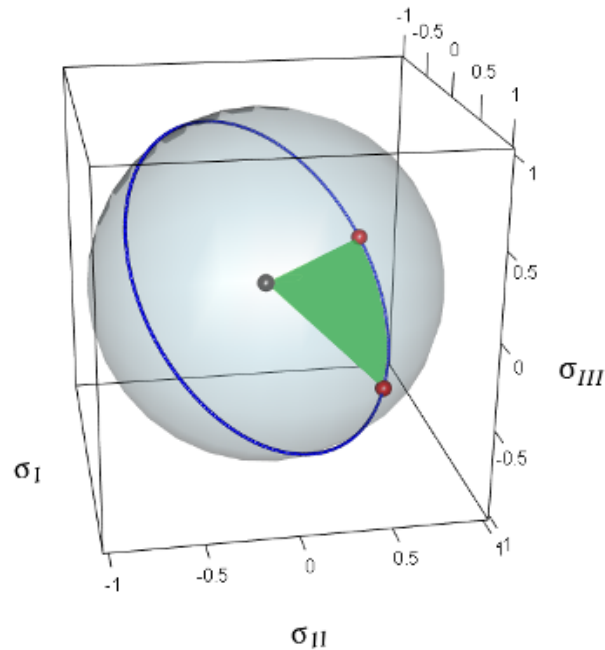


Figure 2.14.: Intersection of Deviatoric Plane and Sphere with  $\|\sigma'\|_F = \sqrt{\frac{2}{3}}$

There are 6 equal areas, as each of the 3 principal stress values can be the lowest or the highest, respectively. The green disk in figure 2.14 shows one of the 6 areas. Each possible point on the circle represents one principal stress combination. The edges represent the points where we have an uniaxial stress state. Proceeding the circle from one point to the other, we obtain all possible loading states with varying principal stress relation  $\kappa$ .

Using  $\kappa$  we can connect the relation of principal stresses to the resulting values of maximum shear stress. We therewith also include the middle stress difference in controversion to section 2.41, where the differences of principal stress are regarded, but the height of the middle stress  $\sigma_{II}$  is neglected.

### 3. Fatigue

In the following we deal with cyclically changing stresses resulting in maximum load limits considerable lower than statical ones. A mechanical component undergoes several numbers of loading cycles of differing intensities and frequency, temperature fluctuations or environmental conditions. We focus on repeated cyclic stress states changing in time, which lead to fracture and damage of the material being also referred to as fatigue.

We first introduce the differences between individual resistance types with regards to two different stress states and in the following focus on a larger number of loading states to evaluate various loading histories. Thereby we follow [3; 28]. Furthermore, we introduce an approach for damage accumulation on slip system level.

#### 3.1. Types of Resistance and Fatigue Testing

We differentiate between dynamic (cycle fatigue) strength resistance and operational resistance being both also referred to as fatigue resistance of the component. The former one is used for periodic loadings whereas the latter one describes an aperiodic deterministic or even randomly occurring stress course. Note that in many cases, these terms are not strictly determined and therefore are often used synonymously.

Figure 3.1 shows an exemplary, sinusoidal fatigue test curve. The stress amplitude identified by  $\sigma_a$  gives the strength of stress changes compared to mean stress  $\sigma_m$ , so the height of swings from mean stress to the upper limit  $\sigma_u$  and the lower  $\sigma_l$ . Obviously, the maximum working stroke is given by  $\Delta\sigma = 2\sigma_a$  and it holds that  $\sigma_m = \frac{\sigma_u + \sigma_l}{2}$  and  $\sigma_a = \frac{\sigma_u - \sigma_l}{2}$ .

## 3. Fatigue

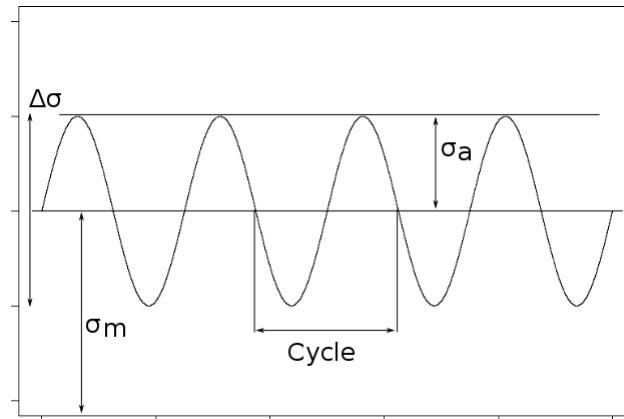


Figure 3.1.: Fatigue Test Curve

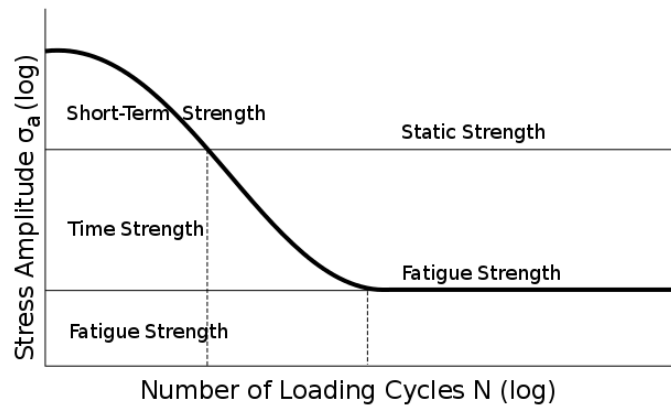


Figure 3.2.: Wöhler Curve

The general fatigue resistance test is called Wöhler fatigue test being a cycle fatigue test with periodically repeated stress or strain cycles of the same heights until a specified failure criterion is reached. The stress amplitudes are varied such that pairs of values for different stress levels  $\sigma_a$  and their maximum number of load cycles until fatigue<sup>3</sup>  $N_i$  are obtained. Plotting these values one obtains the so-called Wöhler line as shown in figure 3.2. There is a large scatter, as the influence of even the smallest material defects on fatigue can be very high.

The range up to a level of lifetime  $N_i = 10^4$  belongs to the short-term fatigue, whereas the range beginning from  $N_i = 10^5$  constitutes the long-term strength, also referred to as time strength or fatigue strength, which has an

<sup>3</sup>Here we use the term lifetime as well.

# Microscopic Damage Accumulation Models

## 3. Fatigue

---

even larger number of cycles and characterizes the material depending range, where the specimen is considered not to fail once the limit is reached. The first range especially covers plastical deformations, beginning from  $N_i = 10^5$  the elastical ones outweigh.

It is very common to also refer to low-cycle fatigue (LCF) and high-cycle fatigue (HCF). LCF corresponds approximately to the short-term strength, whereas HCF begins from  $N_i = 10^5$  according to time strength. The key idea is to differentiate between fatigue mechanisms occurring after a low number of cycles already and those appearing after a large number of cycles. The usage of different terms is often overlapping to some extent. It is a frequent practice to

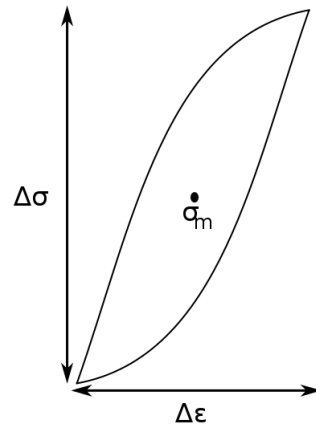


Figure 3.3.: Hysteresis Loop showing Relations between Stress an Strain under Cyclic Loading

do the LCF fatigue testing according to given strain levels rather than stress levels to obtain the so-called strain Wöhler curves.

Figure 3.3 illustrates the non linear relation between stress and strain levels of elastic-plastic load within Wöhler fatigue testing by a hysteresis loop. The composition of strain amplitude  $\epsilon_a = \frac{\Delta\epsilon}{2}$  comprising elastic and plastic parts was introduced by the Ramberg-Osgood equation in (2.23).

Straining the tensile specimen in a sufficient manner leads to an arising of extrusions and intrusions within the material along so-called persistent slip bands, which result from small irreversible dislocations (compare section 2.2.2). For metals, the stress depending Wöhler curve has the form of a straight line on a wide range, the relation can be described by the following

# Microscopic Damage Accumulation Models

## 3. Fatigue

---

**Definition 3.1** (Basquin Equation). *Let  $\sigma'_f > 0$  be the material depending fatigue strength coefficient and  $b < 0$  the fatigue strength exponent. The relation of stress amplitude and life cycle  $N_i$  for metals is approximately given by*

$$\sigma_a = \sigma'_f (2N_i)^b. \quad (3.1)$$

Strain Wöhler diagrams can be divided into two ranges with approximately linear behaviour at log-scale, which characterize the elastical and plastical part of the total strain as seen in (2.23). In order to describe the elastical part and therewith the HCF strain lifetime relation equation (3.1) is used

$$\epsilon_a^{el} = \frac{\sigma'_f}{E} (2N_i)^b. \quad (3.2)$$

As the LCF part covers higher amplitudes, it includes plastical deformations mostly, for which the following relation can be approximated.

**Definition 3.2** (Coffin-Manson Equation). *Consider fatigue ductility coefficient  $\epsilon'_f > 0$  and exponent  $c < 0$ , which characterizes the solidification of the material. The plastical strain lifetime relation can be described by the **Coffin-Manson equation***

$$\epsilon_a^{pl} = \epsilon'_f \cdot (2N_i)^c. \quad (3.3)$$

The composition of both equations (3.1) and (3.2) to total strain leads to

**Definition 3.3** (Coffin-Manson Basquin Equation). *Dividing total strain into plastical and elastical components the relation can be described the following*

$$\epsilon_a = \epsilon_a^{el} + \epsilon_a^{pl} = \frac{\sigma'_f}{E} (2N_i)^b + \epsilon'_f \cdot (2N_i)^c \quad (3.4)$$

*with material constants as given in (3.1) and (3.2).*

In the following we also write in a short form

$$CMB(N_i) = \epsilon_a^{el} + \epsilon_a^{pl} = \frac{\sigma'_f}{E} (2N_i)^b + \epsilon'_f \cdot (2N_i)^c. \quad (3.5)$$

Therewith the relationship between the deterministic number of cycles to failure  $N_i$  and total strain amplitude can be described, see 3.4. To calculate the

# Microscopic Damage Accumulation Models

## 3. Fatigue

---

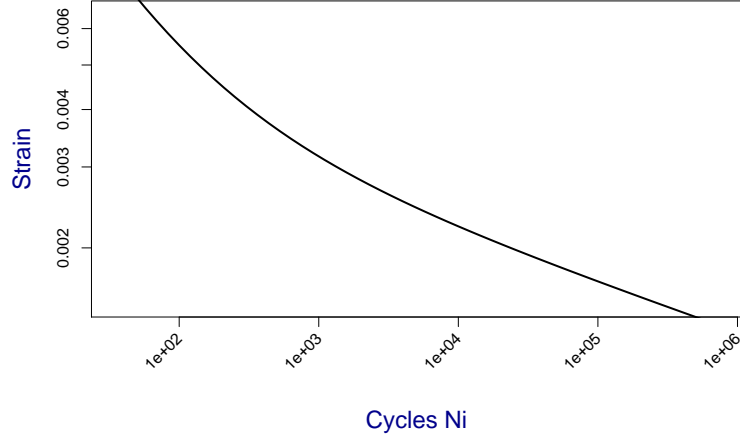


Figure 3.4.: Coffin-Manson Basquin, relation between strain and cycles to failure, axis are scaled in  $\log_{10}$

deterministic number of load cycles to crack initiation based on a given strain amplitude, the equation needs to be inverted, see 3.5. We obtain

$$CMB^{-1}(\epsilon_a) = N_i. \quad (3.6)$$

As plastic yielding causing stress relaxation is not included in using the elastic stress amplitude, the elastic-plastic stress amplitude is overestimated. One can use the common Neuber shake down to convert the elastic stress amplitude to an elastic-plastical one

$$\frac{(\sigma_a^{el})^2}{E} = \frac{(\sigma_a^{el-pl})^2}{E} + \sigma_a^{el-pl} \left( \frac{\sigma_a^{el-pl}}{K} \right)^{\frac{1}{n}} \quad (3.7)$$

By solving  $SD(\sigma_a^{el}) = \sigma_a^{el-pl}$  and plugging in the Ramberg-Osgood equation we obtain  $\epsilon^{el-pl}$ .

After we have introduced the damage mechanisms under cyclic loading, section 3.3.1 shows how cycles of different sizes can be accumulated with regards to their causing damage.

## 3. Fatigue

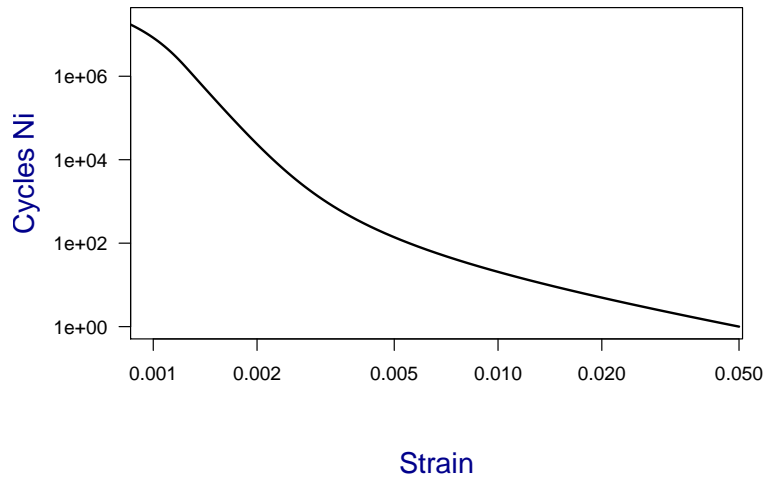


Figure 3.5.: Inverse CMB Relation, resulting from an interpolation in  $R$  with 10 000 knots, the axis are plotted in  $\log_{10}$

### 3.2. Experimental Data

The previously shown results offer a possibility to calculate the number of load cycles  $N_i$  to crack initiation, i.e. a deterministic failure time by inverting  $CMB$  as given in (3.5).

Therewith it should be possible to predict the lifetime of a component based on given parameters of the appropriate material and loading state. For the experimental part, conducted by TU Kaiserslautern, specimen made of Nickel-base superalloy Réne80 are used. Due to the fact that this material has a maximum operational temperature of  $982^\circ\text{C}$ , it is often used in rear stages of gas turbines, where there is a temperature of about  $800^\circ\text{C}$ .

Element	Ni	Cr	Co	Ti	Mo	W	Al	C	B	Zr
Ma.-%	Bal.	14,04	9,48	5,08	4,03	4,02	2,93	0,17	0,0151	0,011
Max.	Bal.	14,3	10	5,2	4,3	4,3	3,2	0,19	0,02	0,1
Min.	Bal.	13,7	9	4,8	3,7	3,7	2,8	0,15	0,01	0,005

Figure 3.6.: Material components of Réne80 specimen

## Microscopic Damage Accumulation Models

### 3. Fatigue

---

The exact casting and follow-up treatment process can be found in [8]. To obtain different grain sizes, the rods, of which the specimens are made, have different diameters. The deviating cooling time results in smaller grains for smaller diameters and bigger grains for larger ones. The dashed black line shows the area of an approximately homogeneous grain structure.

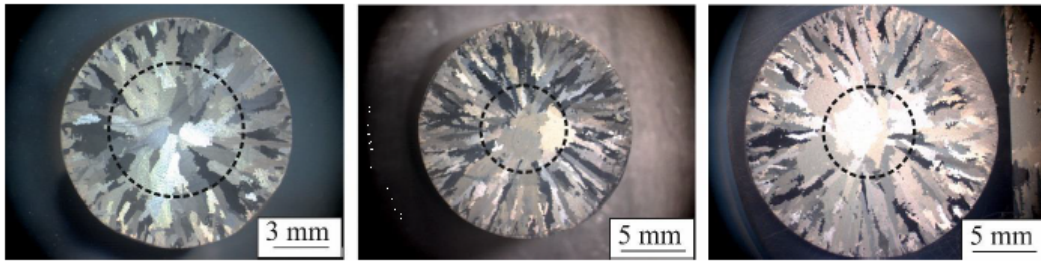


Figure 3.7.: Cross section of the specimen rods with diameter of 12mm, 17mm and 20mm, see [8]

Isothermal LCF experiments are performed under  $850^{\circ}C$ . In case of a crack occurring during the test, the stress amplitude is reduced due to the decreasing cross section. The cycle to fatigue is determined at a stress amplitude drop of 5%.

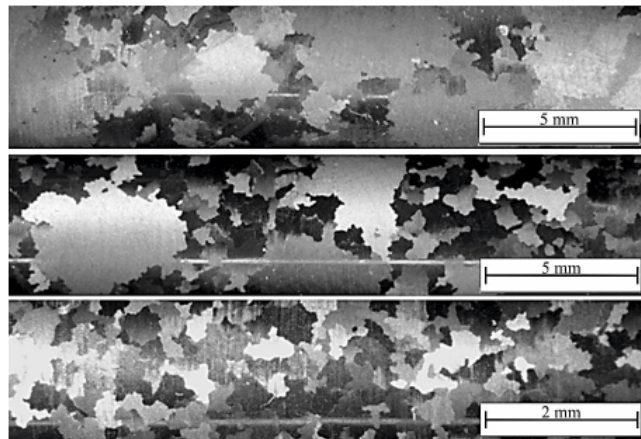


Figure 3.8.: Grain sizes on the surface of the specimen, coarse grain, medium sized grain, fine grain, see [8]

Figure 3.11 shows a big scatter in life for equal stress amplitudes. The fine grained specimens tend to a longer life compared to the medium sized and coarse grained material.

## 3. Fatigue

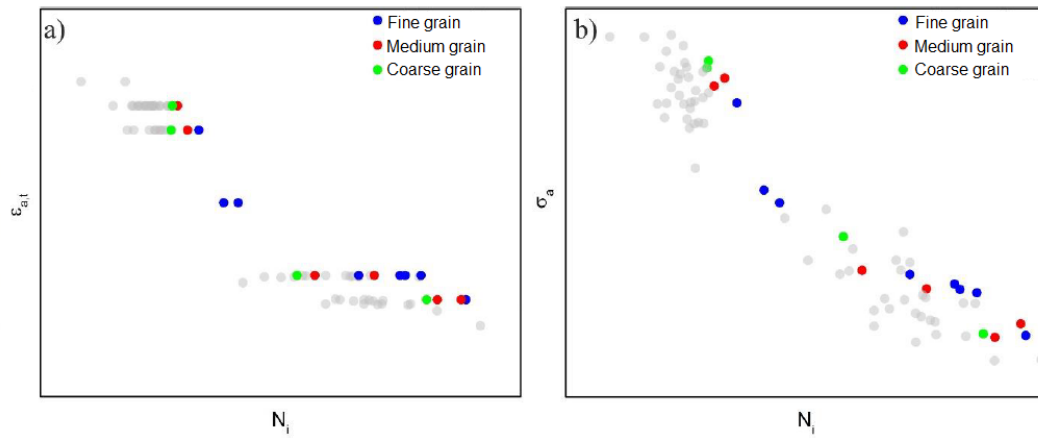


Figure 3.9.: Total strain Wöhler diagram with coarse, medium sized and fine grained specimen, a) shows the total strain amplitude, b) the stress amplitude on the y-axis, cycles to fatigue on the x-axis, plotted with results from [29], see [8]

It is also noticeable that for one strain amplitude the lifetime scatters widely, such that one can not easily imply a deterministic lifetime when loading the specimen by a specific strain. Using the stress amplitude  $\sigma_a$  reduces the scatter significantly for one stress level.

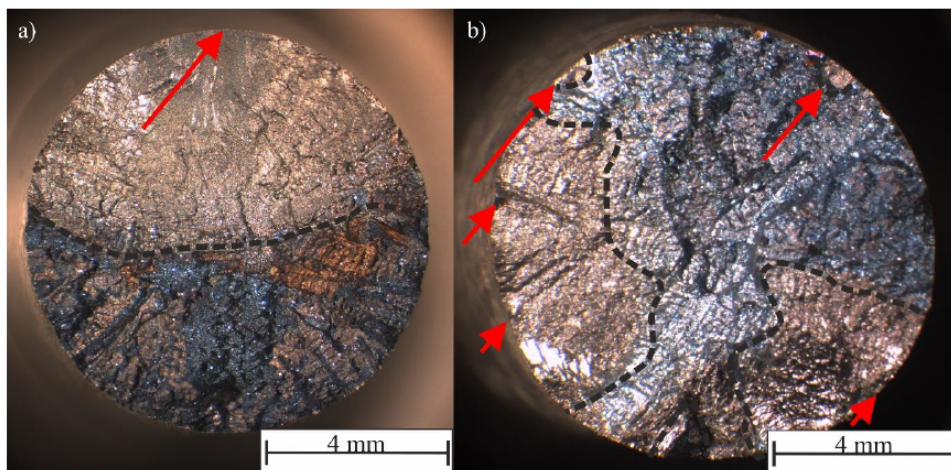


Figure 3.10.: Fracture face of isothermal LCF tests with a, a) low total strain amplitude and fine grained material, b) high total strain amplitude and medium grain size, the red arrows show the crack initiation areas, see [8]

# Microscopic Damage Accumulation Models

## 3. Fatigue

---

The fracture face differs, depending on the level of applied strain. In case of large strain amplitudes there are often several areas of crack initiation due to the high loading and strong plastical deformation. The cracks grow together and lead to an abrupt fatigue. For lower strain amplitudes the cracks grow slowly and start within one single grain. The crack face looks more homogeneous. The different colours within the crack surface result from oxidation under high temperature and make the different areas differentiable.

### 3.2.1. Schmid factors

Low stress amplitudes lead to single cracks, where the plastical deformation is concentrated on one grain and the crack is initiated. The critical shear stress within a slip system of a grain on the surface is exceeded. The local grain orientation and resulting Schmid factor of a specimen and its crack starting zone can be visualized in the so-called EBSD (Electron Back Scatter Diffraction) analysis. Therefore the cutting zone goes through the crack initiating grain, which is afterwards polished and etched.

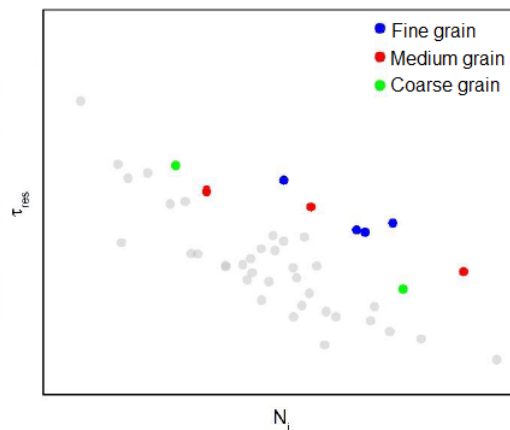


Figure 3.11.: Resulting shear stress within the slip system plotted against cycle to fatigue, together with results from [29], see [8]

Here we can see a clear relation between lifetime to failure  $N_i$  and resulting shear stress  $\tau_{res}$ .

## 3. Fatigue

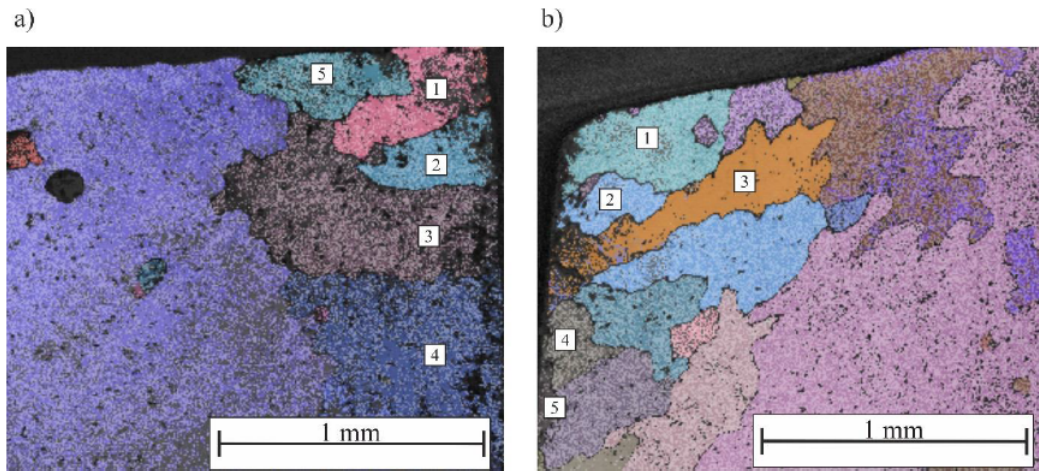


Figure 3.12.: Schmid Factors - EBSD Analysis, see [8]

Grain Number	1	2	3	4	5
Schmid factor	0.46	0.46	0.49	0.49	0.47

Table 3.1.: Schmid factors of grains in 3.12, a)

Grain Number	1	2	3	4	5
Schmid factor	0.46	0.47	0.43	0.49	0.47

Table 3.2.: Schmid factors of grains in 3.12, b)

We see that there are comparably high Schmid Factors in the crack starting area. In practice, we can not look inside the material of the component and therefore need an appropriate possibility to estimate the lifetime based on the regarding parameters such as grain size distribution, stress state and stress history.

The most important problem is that the grains are randomly distributed, there-with deterministic lifetime approaches are not appropriate. Our approach is to build a probabilistic model, which will be introduced in the following chapters.

### 3.3. Damage Accumulation

Looking at the real operation mode of a gas turbine, especially in the case when full and part load periods are considered, a lifetime prediction with constant stress states only is not appropriate. There are several loading collectives, which need to be evaluated differently, as the according lifetimes vary with the respective stress amplitude.

A common approach to estimate a component's life are damage accumulation rules of linear type, such as the so-called Miners rule. The loading states of a stress course are subdivided into several groups of different amplitudes and evaluated with a damage each. The outcome is a damage parameter, whose calculation is given by the following definition.

**Definition 3.4.** *Consider a loading course with  $M \in \mathbb{N}$  different stress states repeated and according amplitudes  $\sigma_a^k$ ,  $k = 1, \dots, M$  with respective deterministic lifetime  $N_{k,det} = N_{det}(\sigma_a^k)$  and  $n_{k,det}$  repetitions in group  $k$ . The damage of collective  $k$  can be calculated as*

$$D_k = \frac{n_{k,det}}{N_{k,det}}. \quad (3.8)$$

According to Miners rule the component fails if

$$\sum_{k=1}^M D_k = \sum_{k=1}^M \frac{n_{k,det}}{N_{k,det}} \geq 1. \quad (3.9)$$

So for each stress component, the number of realized cycles to a given stress amplitude is evaluated in relation to its deterministic admissible number of cycles until failure according to the Coffin-Manson Basquin equation. Once the sum of all groups exceeds a value of 1, hundred percent of allowed cycle numbers is exploited and the component is considered to fail.

One common issue regarding Miners rule is that it does not take into account the sequence of loading states, which may lead to unevaluated sequence effects. As the lifetime is calculated according to a deterministic approach, damage parameter  $D$  is deterministic as well. But the scatter in life is transferred to  $D$  and failure may occur for loading histories having a deterministic damage parameter of  $D < 1$ .

### 3.3.1. Rainflow Counting - General and Slip System Based Approach

The Miners' rule offers a simple possibility to evaluate sustained damage for mechanical components based on the stress history. Therefore the loading course needs to be subdivided into cycles of different height, as each stress amplitude results in a different lifetime value. We consider a stress-time func-

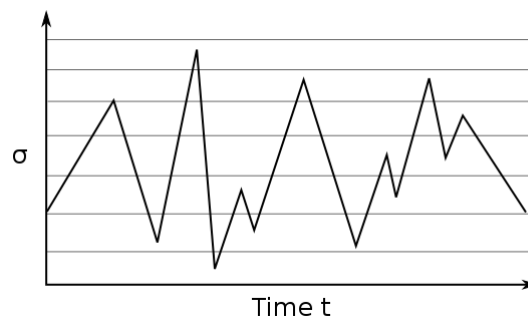


Figure 3.13.: Example of a Stress-Time Function

tion representing the given loading history, i.e. as given in 3.13. The points of interest are the turning points of the stress course, as these local maxima and minima characterize stress reversal and therewith start or end points of load cycles. We can see, that there are also smaller amplitudes adding up to larger cycles. Therefore the load-time history is reduced by removing small cycles, which contribute a negligible amount of damage only.

The aim is to measure the number of passed hysteresis loops of individual stress ranges and evaluate critical load cycles having significant impacts on the damage.

The rainflow counting method was invented by [7] and independently from this research also by [5]. Here we closely follow [22].

Rainflow counting is named as such, as the principle reminds of examining the flow of rain over a set of pagoda roofs. A flows starting point is a positive or negative peak of the time dependent stress or strain function, where the rain reaches the lower level (roof).

The rainflow ends if one of the following conditions is fulfilled:

1. The rainflow of a roof reaches the falling water of a higher roof.

## 3. Fatigue

---

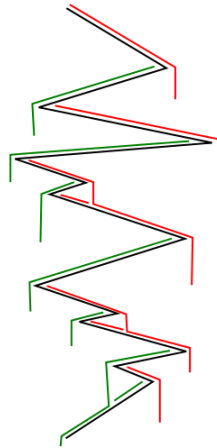


Figure 3.14.: Figure 3.13 as pagoda roof with positive (red) and negative (green) directed flows

2. The waterfall is on the opposite of a peak being higher / lower than (or equal to) the starting point of the flow.
3. There is no higher (or lower) roof, which the falling water reaches.

An example is given in figure 3.14. Each rainflow has an according start point, a stress value at start point respectively, and an end point. The range between each start and end point is evaluated as half cycle regarding stress difference between them.

After all half cycles are determined they are summed up depending on their individual amplitude, since each cycle results in part damages according to a general assumption that damages accumulate and lead to a total damage. We focus on a linear damage accumulation with regards to [23] as given in definition 3.4.

Although it may lead to uncertain or inaccurate results, it is a very frequent practice due to simplification and transparency of the procedure. The used lifetime parts  $n_k$  are measured relative to the ones given by Wöhler testing to obtain the portion of load cycles already realized.

## 3. Fatigue

---

### 3.3.1.1. Slip System Based Rainflow Counting

Conventional rainflow counting methods use principal stress ranges or von Mises equivalent stress for cycle counting. This is applicable for uniaxial loadings. For multiaxial and non-proportional loading cycles these methods are not appropriate. According to the previously given reasons, we evaluate the damage each collective causes applying a slip system based approach. Possible approaches to count and evaluate multiaxial variable amplitude loading have been introduced in [35; 4].

We consider that the part damages calculated according to equation (3.8) occur within the slip systems. Therefore we again recall equation (2.43) to calculate shear stress for each slip system in the case of a face centered cubic crystal structure.

Consider 3 loading states  $\sigma_{rep,1}$ ,  $\sigma_{rep,2}$  and  $\sigma_{rep,3}$ , which are alternating due to a cyclic operational course. Applied to (2.43) we obtain 3 shear stress values for each slip system

$$\tau_{i,j}(\sigma_{rep,l}) = n_i \cdot \sigma_{rep,l} \cdot s_{i,j}, \quad (3.10)$$

where  $l = 1, 2, 3$ . Looking at a time history with  $T$  changing points we consider various switches between the stress states and therewith a complete sequence of stress scenarios

$$\sigma_{hist} = \begin{pmatrix} \sigma_{hist,0} \\ \sigma_{hist,1} \\ \vdots \\ \sigma_{hist,T} \end{pmatrix}, \quad (3.11)$$

with  $\sigma_{hist,t} \in \{\sigma_{rep,1}, \sigma_{rep,2}, \sigma_{rep,3}\}$ ,  $t = 0, 1, \dots, T$ . The shear stress for each slip system at a given time point  $m > 0$  is given by

$$\tau_{i,j}(\sigma_{hist,m}) = \tau_{i,j}(\sigma_{hist,m}). \quad (3.12)$$

Since we apply rainflow counting, we first reduce the given historical load course and remove small cycles. For 3 stress scenarios it is sufficient to apply the following:

As there are 3 stress scenarios  $\sigma_{rep,1}$ ,  $\sigma_{rep,2}$  and  $\sigma_{rep,3}$  for a fixed slip system, there are 3 different situations of resulting shear stress, namely  $\tau_{i,j}(\sigma_{rep,1})$ ,  $\tau_{i,j}(\sigma_{rep,2})$  or  $\tau_{i,j}(\sigma_{rep,3})$ .

## Microscopic Damage Accumulation Models

### 3. Fatigue

<b>Algorithmus 1</b> : Reduce History for Rainflow Counting with 3 Load States	
<b>Data</b> : $\sigma_{hist}$ ( $T + 1 \times 3 \times 3$ ) tensor with $\sigma_{hist,m} \in \{\sigma_{rep,1}, \sigma_{rep,2}, \sigma_{rep,3}\}$ $\forall m \in \{0, 1, \dots, T\}$ , Slip Plane Normals $n_i$ , Slip Systems $s_{i,j}$ , $i = 1, 2, 3, 4, j = 1, 2, 3$	
<b>Result</b> : $\sigma^*$ ( $T' \times 3 \times 3$ ) tensor containing the reduced stress history	
<b>for</b> all slip planes $i = 1, 2, 3, 4$ <b>do</b>	
<b>for</b> all slip systems $j = 1, 2, 3$ <b>do</b>	
1	Let $\tau_{a,i,j}(\sigma_{hist,m}) :=$
	$\tau_{i,j}(\sigma_{hist,m}) - \tau_{i,j}(\sigma_{hist,m-1})$ <b>for</b> all changing points $m = 1, \dots, T$ <b>do</b>
2	<b>if</b> $\text{sgn}(\tau_{a,i,j}(\sigma_{hist,m}) \cdot \tau_{a,i,j}(\sigma_{hist,m+1})) == +1$ <b>then</b>
	Delete $\sigma_{hist,m}$ ;
	<b>end</b>
	<b>end</b>
	<b>end</b>
	<b>end</b>
3	Store new load history with $T'$ points as $\sigma^*$

This results in the following possible stress amplitudes for a given time point  $m$  of the adjusted load history:

$$\tau_{a,i,j}(\sigma_m^*) = \begin{cases} (\tau_{i,j}(\sigma_{rep,1}) - \tau_{i,j}(\sigma_{rep,2}))/2, & \text{if } \sigma_m^* = \sigma_{rep,1}, \sigma_{m-1}^* = \sigma_{rep,2} \text{ OR v.v.}, \\ (\tau_{i,j}(\sigma_{rep,2}) - \tau_{i,j}(\sigma_{rep,3}))/2, & \text{if } \sigma_m^* = \sigma_{rep,2}, \sigma_{m-1}^* = \sigma_{rep,3} \text{ OR v.v.}, \\ (\tau_{i,j}(\sigma_{rep,1}) - \tau_{i,j}(\sigma_{rep,3}))/2, & \text{if } \sigma_m^* = \sigma_{rep,1}, \sigma_{m-1}^* = \sigma_{rep,3} \text{ OR v.v.} \end{cases}$$

Algorithm 2 shows the counting for a face-centered cubic crystal with 3 states and the previously adjusted load history according to the given rainflow counting method. Let the stress amplitudes be sorted with respect to their size, such that

$$\tau_{i,j}(\sigma_{rep,1}) - \tau_{i,j}(\sigma_{rep,3}) \geq \tau_{i,j}(\sigma_{rep,1}) - \tau_{i,j}(\sigma_{rep,2}) \geq \tau_{i,j}(\sigma_{rep,2}) - \tau_{i,j}(\sigma_{rep,3}).$$

To introduce a shorter form let  $\tau_{aI} := \tau_{i,j}(\sigma_{rep,1}) - \tau_{i,j}(\sigma_{rep,3})$ ,

$\tau_{aII} := \tau_{i,j}(\sigma_{rep,1}) - \tau_{i,j}(\sigma_{rep,2})$  and  $\tau_{aIII} := \tau_{i,j}(\sigma_{rep,2}) - \tau_{i,j}(\sigma_{rep,3})$ .

With the method described in algorithm 1 and 2 we can evaluate given stress scenarios with respect to their damage with a slip system based approach. The problem is the unknown orientation of grains. Therefore a probabilistic approach and enlargement for this method will be introduced in chapter 10.

## Microscopic Damage Accumulation Models

### 3. Fatigue

---

**Algorithmus 2** : Rainflow Counting per Slip System with 3 Stress States

**Data** :  $\sigma^*$  ( $T' \times 3 \times 3$ ) tensor with  $\sigma_m^* \in \{\sigma_{rep,1}, \sigma_{rep,2}, \sigma_{rep,3}\}$   
 $\forall m \in \{0, 1, \dots, T\}$ , Slip Plane Normals  $n_i$ , Slip Systems  $s_{i,j}$ ,  
 $i = 1, 2, 3, 4, j = 1, 2, 3$

**Result** :  $N_{rain}$  ( $3 \times 3 \times 4$ ) tensor containing the rainflow counts of 3 stress states for a fcc crystal (12 slip systems)

```
1 Initialize a  $3 \times 3 \times 4$  tensor  $n_{rain} := 0$ ;  
for all slip planes  $i = 1, 2, 3, 4$  do  
  for all slip systems  $j = 1, 2, 3$  do  
2    Sort shear stress amplitudes according to size, such that  
       $\tau_{aI} := \tau_{i,j}(\sigma_{rep,1}) - \tau_{i,j}(\sigma_{rep,3})$ ,  $\tau_{aII} := \tau_{i,j}(\sigma_{rep,1}) - \tau_{i,j}(\sigma_{rep,2})$  and  
       $\tau_{aIII} := \tau_{i,j}(\sigma_{rep,2}) - \tau_{i,j}(\sigma_{rep,3})$  with  $\tau_{aI} \geq \tau_{aII} \geq \tau_{aIII}$ ;  
3    for all changing points  $m = 1, \dots, T'$  do  
4      Calculate shear stress amplitudes  
       $\tau_{a,i,j}(\sigma_m^*) := \tau_{i,j}(\sigma_m^*) - \tau_{i,j}(\sigma_{m-1}^*)$ ;  
      if  $\tau_{a,i,j}(\sigma_m^*) == \tau_{aI}$  then  
        |  $N_{rain,1,i,j} := N_{rain,1,i,j} + 1$ ;  
      else if  $\tau_{a,i,j}(\sigma_m^*) == \tau_{aII}$  then  
        |  $N_{rain,2,i,j} := N_{rain,2,i,j} + 1$ ;  
      else  
        |  $N_{rain,3,i,j} := N_{rain,3,i,j} + 1$ ;  
      end  
    end  
  end  
end  
end
```

## 4. Mathematical Basics

We introduce mathematical basics to describe the random orientations of grains appropriately and give some numerical insight to solve the recurrence relations arising from the percolation model in the next chapters.

### 4.1. Stochastic Fundamentals and Haar Measure

For the following we follow [6] and [15].

**Definition 4.1** (Group). *A group is a set  $\Gamma$  with a corresponding operation  $\cdot : \Gamma \times \Gamma \rightarrow \Gamma$  which complies*

1.  $(ab)c = a(bc) \forall a, b, c \in \Gamma$  (Associativity)
2.  $\exists e \in \Gamma$  such that  $ae = ea = e \forall a \in \Gamma$  (Existence of identity)
3.  $\forall a \in \Gamma \exists a^{-1} \in \Gamma$  such that  $aa^{-1} = a^{-1}a = e$  (Existence of inverse)

In the following let  $\Gamma$  be a group with identity element  $e$ . With  $A, B \subset \Gamma$  and  $x \in \Gamma$  we determine

$$\begin{aligned} AB &:= \{ab : a \in A, b \in B\}, A^{-1} := \{a^{-1} : a \in A\}, \\ xA &:= \{xa : a \in A\}, Ax := \{ax : a \in A\}. \end{aligned} \tag{4.1}$$

For  $a \in \Gamma$  we define left translation  $L(a) : \Gamma \rightarrow \Gamma$  and right translation  $R(a) : \Gamma \rightarrow \Gamma$  as  $L(a) := ax$  and  $R(a) := xa, x \in \Gamma$ .

**Definition 4.2** (Topological space). *Let  $X$  be a set. A set of subsets of  $X$   $\tau$  is a topology on  $X$  if*

# Microscopic Damage Accumulation Models

## 4. Mathematical Basics

---

1.  $\emptyset, X \in \tau$ ,
2.  $A_i \in \tau \forall i \in I \Rightarrow \bigcup_{i \in I} A_i \in \tau$  for all set of indices  $I$ ,
3.  $A_1, \dots, A_n \in \tau \Rightarrow \bigcap_{i=1}^n A_i \in \tau$ .

$X$  has the Hausdorff property if  $\forall x, y \in X \exists U, V \in \tau$  with  $x \in U, y \in V$  and  $U \cap V = \emptyset$ .

In the following will consider the groups to fulfill the Hausdorff property. Let  $C(X)$  denote the space of continuous functions  $f : X \rightarrow \mathbb{K}$ . Further let  $C_C(X)$  denote the space of  $f \in C(X)$  with compact  $\text{supp } f := \{f \neq 0\}$  and  $C_C^+(X)$  the non-negative elements of  $C_C(X)$ .

**Definition 4.3** (Topological group). *A group  $\Gamma$  with an associated topology  $\tau$  on  $\Gamma$  is a topological group, if the maps*

$$\begin{aligned} \Gamma \times \Gamma &\rightarrow \Gamma & (x, y) &\rightarrow xy \text{ (group multiplication)} \\ \Gamma &\rightarrow \Gamma & x &\rightarrow x^{-1} \text{ (inverse)} \end{aligned}$$

*are continuous. A group with a Hausdorff topology is locally compact if each point  $x \in X$  has a compact neighborhood.*

**Definition 4.4** (Lie group). *A topological group with the structure of a  $C^\infty$  manifold having a smooth multiplication and inversion map is called a Lie group.*

**Definition 4.5.** *The special orthogonal group  $SO(3)$  with matrix multiplication is the set of matrices in  $\{U \mid U \in \mathbb{R}^{3 \times 3} : UU^T = U^T U = \mathbb{1}, \det(U) = 1\}$ . It represents the group of rotations in  $\mathbb{R}^3$ .*

**Definition 4.6** (Borel measure, Radon measure). *Let  $X$  be a locally compact Hausdorff space with Borel  $\sigma$ -algebra  $\mathcal{B}(X)$ . If for a measure  $\mu : \mathcal{B} \rightarrow [0, \infty]$  it holds that  $\forall x \in X \exists$  an open set  $D$  with  $\mu(D) < \infty$ , then  $\mu$  is a Borel measure. If additionally,*

$$\forall B \in \mathcal{B}(X) : \mu(B) = \sup\{\mu(K) \mid K \subset B, K \text{ compact}\}, \quad (4.2)$$

*$\mu$  is a Radon measure.*

# Microscopic Damage Accumulation Models

## 4. Mathematical Basics

---

A linear form  $I : C_C(\Gamma) \rightarrow \mathbb{K}$  with

$$I(f \circ L(y)) = I(f), \quad (4.3)$$

$f \in C_C(\Gamma)$ ,  $y \in \Gamma$ , is called left invariant. Analogously, a measure  $\mu : \mathcal{B}(\Gamma) \rightarrow [0, \infty]$  is left invariant, if  $\forall y \in \Gamma$  it holds that

$$\mu(yB) = \mu(B), \quad (4.4)$$

$B \in \mathcal{B}(\Gamma)$ ,  $y \in \Gamma$ , i.e. if  $L(y)(\mu) = \mu$ .

**Theorem 4.7** (3.8, [6]). *Let  $\Gamma$  be a topological group. Each  $f \in C_C(\Gamma)$  is left- and right uniformly continuous<sup>4</sup>.*

**Lemma 4.8** (3.9, [6]). *Let  $\Gamma$  be a locally compact Hausdorff topological group. Let  $I : C_C(\Gamma) \rightarrow \mathbb{K}$  be a left invariant positive linear form. There exists exactly one Radon measure  $\mu : \mathcal{B}(\Gamma) \rightarrow [0, \infty]$  with*

$$I(f) = \int_{\Gamma} f d\mu, \quad (4.5)$$

*$f \in C_C(\Gamma)$ , and  $\mu$  is left invariant. In reverse, with each left invariant Radon measure  $\mu : \mathcal{B}(\Gamma) \rightarrow [0, \infty]$  complies a left invariant positive linear form  $I : C_C(\Gamma) \rightarrow \mathbb{K}$ , so  $I(f) \geq 0$  for  $f \geq 0$ , with (4.5).*

**[Proof]** Since  $I$  is a left invariant positive linear form on  $C_C(\Gamma)$ , there exists exactly one Radon measure  $\mu$  with (4.5) according to Riesz-Markov representation theorem (see [6] for example). Applying the general transformation law (V.3.1, [6]), it holds for  $f \in C_C(\Gamma)$ ,  $y \in \Gamma$

$$I(f) = I(f \circ L(y)) = \int_{\Gamma} f \circ L(y) d\mu = \int_{\Gamma} f dL(y)(\mu), \quad (4.6)$$

which means that  $\mu$  is left invariant. Since  $L(y)(\mu)$  is a Radon measure, it holds that  $L(y)(\mu) = \mu$ ,  $y \in \Gamma$ , as  $\mu$  is unique. Vice versa, with the general transformation law the left invariance of  $I$  follows, if  $\mu$  in (4.5) is a left invariant Radon measure. ■

**Theorem 4.9** (3.11,[6]). *Let  $\Gamma$  be a locally compact Hausdorff topological group. There exists a left invariant positive linear form  $I : C_C(\Gamma) \rightarrow \mathbb{K}$ ,  $I \neq 0$ ,*

---

<sup>4</sup>See A.1 for definition.

# Microscopic Damage Accumulation Models

## 4. Mathematical Basics

---

and  $I$  is uniquely determined except for a positive factor.  $I$  is called left Haar integral on  $C_C(\Gamma)$ .

The proof is given in A.2.

**Theorem 4.10** (3.12,[6]). *Let  $\Gamma$  be a locally compact Hausdorff topological group. There exists a left invariant Radon measure  $\mu : \mathcal{B}(\Gamma) \rightarrow [0, \infty]$ ,  $\mu \neq 0$ , and  $\mu$  is determined uniquely up to a positive factor.  $\mu$  is the left Haar measure on  $\Gamma$ .*

**[Proof]** The statement is following from (4.8) and (4.9). ■

Let

$$Z(\theta) = \begin{pmatrix} \cos \theta & -\sin \theta & 0 \\ \sin \theta & \cos \theta & 0 \\ 0 & 0 & 1 \end{pmatrix} \quad (4.7)$$

be rotations around the z-axes and

$$X(\theta) = \begin{pmatrix} 1 & 0 & 0 \\ 0 & \cos \theta & -\sin \theta \\ 0 & \sin \theta & \cos \theta \end{pmatrix} \quad (4.8)$$

around the x-axes. An element  $U \in SO(3)$  can be parametrized by the so-called Euler angles and therewith represented via

$$U = Z(\varphi_2)X(\theta)Z(\varphi_1) \quad (4.9)$$

with  $\theta \in [0, \pi]$ ,  $\varphi_1, \varphi_2 \in [0, 2\pi)$ .

Let  $f(U)$  be a function depending on orientation  $U$ . We obtain for the integral in accordance with the Haar measure the following

$$\int_{SO(3)} f(U)dU = \frac{1}{8\pi^2} \int_0^\pi \int_0^{2\pi} \int_0^{2\pi} f(U(\varphi_1, \varphi_2, \theta))d\varphi_1d\varphi_2 \sin \theta d\theta. \quad (4.10)$$

As orientation-depending function we will use

$$f(U) = \mathbb{1}_{\{m(U) \leq m\}} \quad (4.11)$$

with  $m(U)$  being defined in (5.3).

## 4.2. Recurrence Relations

We use [20] and [30] in the following section.

**Definition 4.11.** *A recurrence relation of order  $k$  is defined as*

$$t_n = f(n, t_{n-1}, \dots, t_{n-k}), \quad (4.12)$$

*with order  $k$  of the relation and therefore the number of dependencies and initial conditions.*

**Definition 4.12** (homogeneous, linear). *A recurrence relation*

$$t_n = d_1 t_{n-1} + \dots + d_k t_{n-k} + c_k \quad (4.13)$$

*with initial conditions  $t_i = c_i \forall i \in \{0, \dots, k-1\}$  is linear and of order  $k$ . If*

$$c_k = 0, \quad (4.14)$$

*it is a linear homogeneous recurrence relation.*

A homogeneous linear recurrence relation of second order is

$$t_n = d_1 t_{n-1} + d_2 t_{n-2}, \quad (4.15)$$

with  $n \geq 2$ .

The recurrence can be considered as a kind of polynomial and  $t_i$  can be replaced by  $x^i$ .

**Definition 4.13** (Characteristical Polynomial). *The characteristical polynomial of a homogeneous recurrence relation is given by*

$$P(x) = d_k x^n + d_{k-1} x^{k-1} + \dots + d_1 x^1 + d_0 x^0 = \sum_{\lambda=0}^k d_\lambda \cdot x^\lambda. \quad (4.16)$$

**Theorem 4.14** (4.15,[20]). *Let  $\alpha \neq \beta$  be real zero crossings of the characteristical polynomial  $P(x) = x^2 - d_1 x - d_2$ . All solutions of the recurrence relation  $t_n = d_1 t_{n-1} - d_2$  are given by*

$$t_n = c_1 \alpha^n + c_2 \beta^n \quad (4.17)$$

# Microscopic Damage Accumulation Models

## 4. Mathematical Basics

---

for  $c_1, c_2 \in \mathbb{R}$ .

**[Proof]** First we show that all  $t_n$  of the given form fullfill the recurrence relation. Therefore let  $c_1, c_2 \in \mathbb{R}$ . We can write

$$\begin{aligned} t_n &= c_1 \alpha^n + c_2 \beta^n \\ &= c_1 \alpha^{n-2} \alpha^2 + c_2 \beta^n - 2\beta^2 \\ &= c_1 \alpha^{n-2} \cdot (d_1 \alpha + d_2) + c_2 \beta^{n-2} \cdot (d_1 \beta + d_2) \\ &= d_1 \cdot (c_1 \alpha^{n-1} + c_2 \beta^{n-1}) + d_2 \cdot (c_1 \alpha^{n-2} + c_2 \beta^{n-2}) \\ &= d_1 t_{n-1} + d_2 t_{n-2} \end{aligned} \tag{4.18}$$

Now let  $t_n$  be a solution of the recurrence. We define

$$s_n := t_n - (c_1 \alpha^n + c_2 \beta^n), \tag{4.19}$$

$c_1, c_2 \in \mathbb{R}$ , such that  $s_0 = 0$  and  $s_1 = 0$ . As per (4.18),  $s_n$  also fullfills the recurrence relation, i.e.

$$s_n = d_1 s_{n-1} + d_2 s_{n-2}, \tag{4.20}$$

$n \geq 2$ . Since  $s_0 = s_1 = 0$ , it follows that  $s_n = 0 \forall n \geq 2$  and therewith it holds for (4.19)

$$t_n = s_n + (c_1 \alpha^n + c_2 \beta^n) = c_1 \alpha^n + c_2 \beta^n. \tag{4.21}$$

■

## **5. Grain Orientation and Probabilistic Schmid Factors**

### **5.1. Random Grain Orientation and Probabilistic Schmid Factors**

As we do not know the actual orientation of grains and their individual sizes, we will introduce an approach, which includes and projects the probabilistic properties appropriately. Therefore, we model the distribution of grains according to the Haar measure, which we introduced in section 4.1.

We assume that the scatter occurring in LCF life arises from the scatter of shear stress acting on the different slip planes, which are randomly oriented.

First, we consider the case of an uniaxial loading state and then continue with multiaxial stress scenarios. In this regard, we show the differences between both assumptions and their impacts.

#### **5.1.1. Probabilistic Schmid Factors**

We consider a crystal with face centered cubic lattice with properties as given in (2.43) and before. We make the assumption that the material is isotropic and the orientation of each grain is random as well as independent from neighbouring grains.

A rotation can be represented by a transformation with a rotation matrix  $U \in SO(3)$ . The randomness of a grain can therewith be represented by a random transformation of the according slip systems within the crystal, in particular of  $n_i$  and  $s_{i,j}$ .

We parametrize via Euler angles. Let us therefore consider a coordinate system

# Microscopic Damage Accumulation Models

## 5. Grain Orientation and Probabilistic Schmid Factors

---

with basis vectors  $e_1, e_2$  and  $e_3$  which is transferred to an arbitrarily rotated one by carrying out 3 successively rotations.

1. Rotation of  $\varphi_1 \in [0, 2\pi)$  around  $e_3$ .
2. Rotation of  $\theta \in [0, \pi)$  around  $e_1$  the axis  $e_3$  is changed to  $e'_3$ .
3. Rotation of  $\varphi_2 \in [0, 2\pi)$  around  $e'_3$ .

Hence we obtain an arbitrary rotation matrix via

$$U(\varphi_1, \varphi_2, \theta) = \begin{pmatrix} \cos \varphi_2 & \sin \varphi_2 & 0 \\ -\sin \varphi_2 & \cos \varphi_2 & 0 \\ 0 & 0 & 1 \end{pmatrix} \begin{pmatrix} 1 & 0 & 0 \\ 0 & \cos \theta & \sin \theta \\ 0 & -\sin \theta & \cos \theta \end{pmatrix} \begin{pmatrix} \cos \varphi_1 & \sin \varphi_1 & 0 \\ -\sin \varphi_1 & \cos \varphi_1 & 0 \\ 0 & 0 & 1 \end{pmatrix}$$

with  $\varphi_1, \varphi_2$  and  $\theta$  being called the Euler angles.

As we transform  $n_i$  and  $s_{i,j}$  with  $U(\varphi_1, \varphi_2, \theta)$ , slip planes and systems become probabilistic and we obtain

$$\begin{aligned} n_i(U) &= U n_i, \\ s_{i,j}(U) &= U s_{i,j}. \end{aligned} \tag{5.1}$$

Considering the random transformation acting on the slip planes and systems, one can obtain probabilistic shear stress as well as their maximum value depending on rotation  $U$ ,

$$\tau_{i,j}(U) = U n_i \cdot \sigma \cdot U s_{i,j}, \tau = \max_{i,j} |\tau_{i,j}(U)|. \tag{5.2}$$

We do not necessarily need the maximum value only, when we want to proceed the rainflow counting to accumulate damages, all stress values within one time step need to be stored. But first we focus on the most simple case having equal stress states and a constant von Mises stress amplitude.

As the probability distribution of  $U$  is uniquely determined, one method to generate random rotation matrices is given in algorithm 3.

The random generation of Euler angles according to the Haar measure is implemented within the **rotations** package in *R*. In order to reduce simulation expense, there is a more efficient approach to generate maximum shear stress. As we know the distribution of the Euler angles, we can discretize and weight them in accordance to their density value.

To build the density values for maximum shear stress we choose a number of grid points  $N_a$ , with which we discretize each of the Euler angles. Based on these mesh

## Microscopic Damage Accumulation Models

### 5. Grain Orientation and Probabilistic Schmid Factors

<b>Algorithmus 3</b> : Monte Carlo Simulation of Random Shear Stress	
<b>Data</b> : Slip Plane Normals $n_i$ , Slip Systems $s_{i,j}$ , $i = 1, 2, 3, 4$ , $j = 1, 2, 3$ , Stress Tensor $\sigma$ , Number of Simulations $M_{SF}$	
<b>Result</b> : $SF$ ( $12 \times M_{SF}$ ) matrix containing the shear stresses for a fcc crystal with loading state $\sigma$ , $SF_{max}$ vector of size $M_{SF}$ containing the maximum shear stress for each simulation	
1	Initialize a $M_{SF} \times 12$ matrix $SF := 0$ ;
2	Initialize a $M_{SF}$ vector $SF_{max} := 0$ ;
	<b>for</b> all simulation steps $k = 1, \dots, M_{SF}$ <b>do</b>
3	Generate random Euler angles $\varphi_1, \varphi_2, \theta$ according to Haar measure;
4	Build random rotation matrix $U(\varphi_1, \varphi_2, \theta)$ ;
	<b>for</b> all slip planes $i = 1, 2, 3, 4$ <b>do</b>
	<b>for</b> all slip systems $j = 1, 2, 3$ <b>do</b>
5	Calculate random shear stress $\tau_{i,j}(U) = U \cdot s_{i,j} \sigma \cdot U \cdot n_i$
	$SF_{i,j,k} := \tau_{i,j}$ ;
6	Compute maximum shear stress $\tau = \max_{i,j}  \tau_{i,j}(U) $
	$SF_{max,k} := \tau$ ;
	<b>end</b>
	<b>end</b>
	<b>end</b>

points we build the rotation matrices and calculate maximum shear stress for each rotation. The weights according to the density for  $SO(3)$  with regards to the Haar measure are calculated and stored as well to further obtain the densities of Schmid factors. Algorithm 4 shows the procedure. Based on the results of both algorithms we can obtain

$$m(U) = \frac{\tau(U)}{\sqrt{\frac{3}{2}} \cdot \|\sigma'\|_F}. \quad (5.3)$$

We again consider the former mentioned Haar measure for  $SO(3)$

$$\int_{SO(3)} f(U) d\mu(\gamma) = \int_0^\pi \int_0^{2\pi} \int_0^{2\pi} \frac{1}{8\pi^2} \sin \theta f(U(\varphi_1, \varphi_2, \theta)) d\varphi_1 d\varphi_2 d\theta \quad (5.4)$$

with

$$f(U) = \mathbb{1}_{\{m(U) \leq m\}}. \quad (5.5)$$

The algorithm is independent from the chosen crystal structure type, the normal and slip system vectors can be customized, such that we obtain simulation results for different types of crystals.

## Microscopic Damage Accumulation Models

### 5. Grain Orientation and Probabilistic Schmid Factors

**Algorithmus 4 :** Calculation of Shear Stress with Discretization of Euler Angles

**Data :** Slip Plane Normals  $n_i$ , Slip Systems  $s_{i,j}$ ,  $i = 1, 2, 3, 4$ ,  
 $j = 1, 2, 3$ , Stress Tensor  $\sigma$ , Number of Grid Points for Euler Angles  $N_a$

**Result :**  $SF$  ( $12 \times N_q$ ) matrix containing the shear stresses for a fcc crystal with loading state  $\sigma$ ,  $SF_{max}$  vector of size  $N_q$  containing the maximum shear stress for each grid point

```

1 Initialize  $I := [0, 2\pi] \times [0, 2\pi] \times [0, \pi]$ ;
2 Set number of grid points  $N_q := (N_a - 1)^3$ ;
3 Initialize grid points  $x_1, \dots, x_{N_q} \in I$  for Euler angle discretization;
4 Initialize a  $N_q \times 12$  matrix  $SF := 0$ ;
5 Initialize  $N_q$  vectors  $SF_{max} := 0$  and  $w_k := 0$ ;
for all grid points  $x_k$ ,  $k = 1, \dots, N_q$  do
6   Set Euler angles  $(\varphi_1, \varphi_2, \theta) := x_k$ ;
7   Compute rotation matrix  $U(\varphi_1, \varphi_2, \theta)$ ;
   for all slip planes  $i = 1, 2, 3, 4$  do
   for all slip systems  $j = 1, 2, 3$  do
8     Calculate shear stress  $\tau_{i,j}(U) = U \cdot s_{i,j} \sigma \cdot U \cdot n_i$ 
      $SF_{i,j,k} := \tau_{i,j}$ ;
9     Compute maximum shear stress  $\tau = \max_{i,j} |\tau_{i,j}(U)|$ 
      $SF_{max,k} := \tau$ ;
10    Calculate weight according to Haar measure and store
      $w_k := \frac{\sin(\theta)}{8\pi^2}$ ;
   end
  end
end

```

First, we consider the stress state in the simulation to be uniaxial with

$$\sigma = \begin{pmatrix} \sigma_I & 0 & 0 \\ 0 & 0 & 0 \\ 0 & 0 & 0 \end{pmatrix}. \quad (5.6)$$

and  $\|\sigma'\|_F = \sqrt{\frac{2}{3}}$ . After a Monte Carlo simulation with an amount of 1 Mio. simulation steps we can display the density of maximum shear stress of a face-centered cubic crystal, as it is shown in figure 5.1.

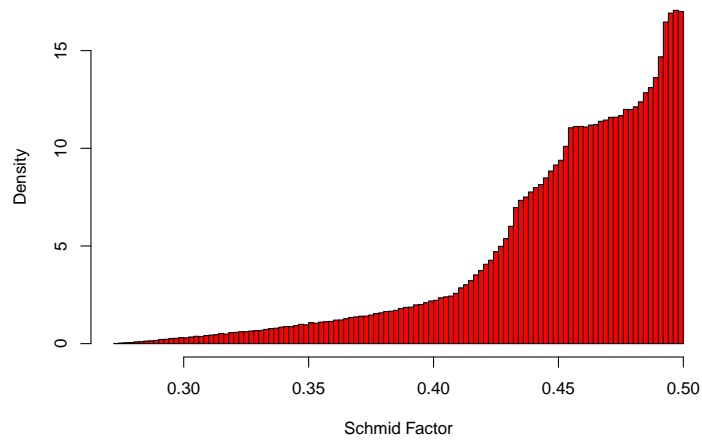


Figure 5.1.: MC Simulation - Density of Schmid Factor Distribution

We see a characteristic course of the histogram with a very sharp limit at  $m = 0.5$ , which represents the case of forces acting in direction  $45^\circ$  to a slip system. For the uniaxial case this is the maximum value of shear stress.

The highest density of values is in the range of 0.4 to 0.5, which is implied by the fact that there are 12 slip systems in total. Therewith there is often at least one of the slip systems oriented such that it has a large Schmid factor. The density for a single slip plane, without maximizing over all 12 ones, looks different, as we can see in figure 5.2.

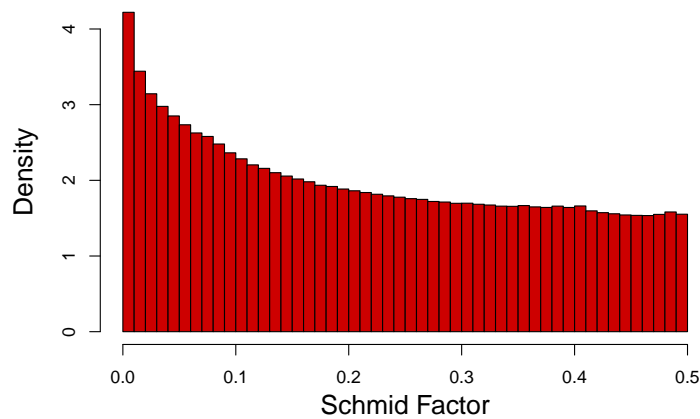


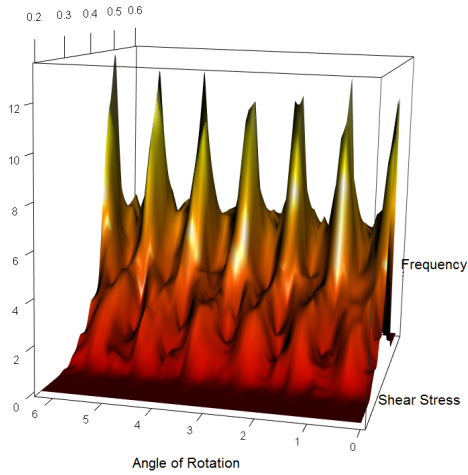
Figure 5.2.: MC Simulation - Density of Schmid Factor Distribution for one Slip Plane

# Microscopic Damage Accumulation Models

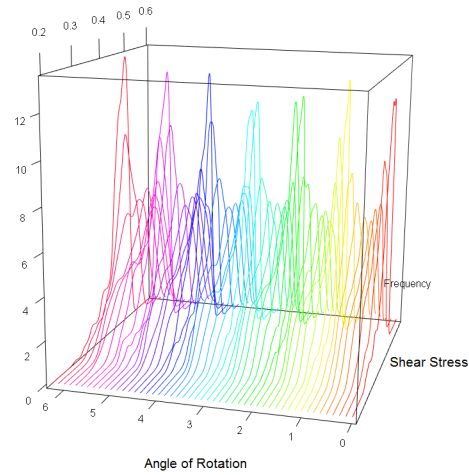
## 5. Grain Orientation and Probabilistic Schmid Factors

---

We are interested in the results for different loading states and want to evaluate these according to the different yield criteria. We consider  $\kappa$  from (2.51), which represents the level of multiaxiality of the principal stress values. The stress tensor for each value of  $\kappa$  can be used for the input tensor in the simulation of algorithm 3.



(a) Surface of Densities of Maximum Shear Stress Distribution



(b) Densities of Maximum Shear Stress Distribution

Consider that for each of the principal stress combinations of the whole circle we proceed the simulation and calculate the values for the density of the maximum shear stress distribution. If we put all of the densities together they build a surface as it is shown in figure 5.3a.

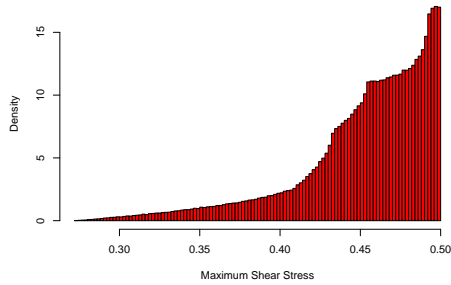
Assume a uniaxial loading state as a start point, so for example one of the red points on the circle in figure 2.14. To reach a point of the circle, we can turn this vector via rotation from 0 to  $2\pi$  around the inclined axis. The x axis plots the angle of rotation around this axis. The z axis gives the value of the density for each shear stress value plotted on the y axis.

As there are 6 areas, where the order of the principal stress values changes, but the relation implies the same  $\kappa$ , we focus on the changes within one of them. The amount of multiaxiality  $\kappa$  equals zero in the red points and reaches its maximum value of 1 in the middle of the way between both. In figure 5.3b we selected some principal stress combinations on the circle and calculated the respective densities of maximum shear stress. It is noticeable, that there are large differences between the several stress states. In a direct comparison of the uniaxial case, as shown again in

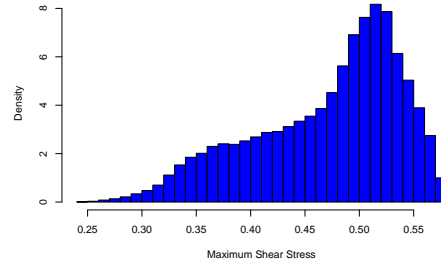
# Microscopic Damage Accumulation Models

## 5. Grain Orientation and Probabilistic Schmid Factors

---



(c) Uniaxial Loading State  $\kappa = 0$



(d) Multiaxial Loading State  $\kappa = 1$

figure 5.3c, to a multiaxial one as shown in figure 5.3d, it is remarkable, that the course of the curve varies significantly.

There is a greater variance of maximum shear stress as well as a higher mean. Additionally, there are maximum shear stress values larger than the upper limit of  $m(U) = 0.5$ . Therewith, the conversion factor used to calculate shear stress based on normal stress is much higher, when multiaxial loading states are present.

Although the von Mises equivalent stress is equal and we change the relation of the principal stress values only, the maximum shear stress of a grain scatters more under multiaxial loading conditions.

Figures 5.3 and 5.4 show the different values for the standard deviation and the mean values depending on the amount of multiaxiality. Under an uniaxial loading state, i.e. where  $\kappa = 0$ , the mean takes the typical value of 0.4523. The larger the part of a second principal stress value becomes, i.e. the more  $\kappa$  increases, the higher is the mean value. Similar results are noticeable for the standard deviation.

## Microscopic Damage Accumulation Models

### 5. Grain Orientation and Probabilistic Schmid Factors

---

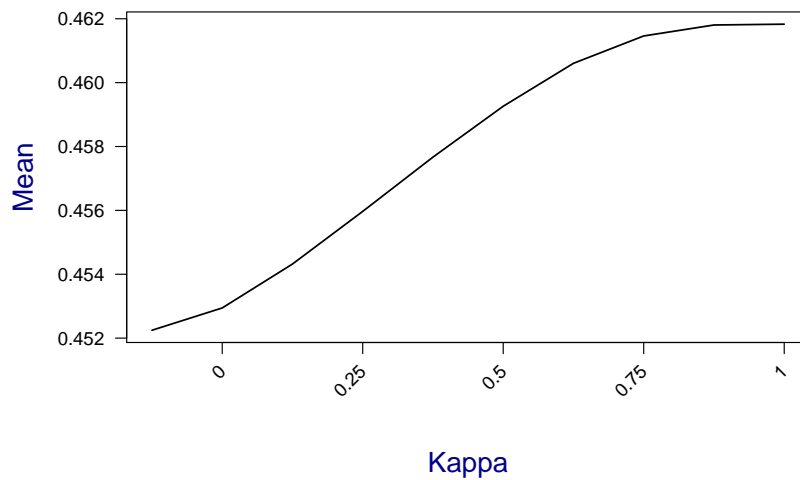


Figure 5.3.: Mean of  $m(U)$  depending on  $\kappa$

Under a maximum of multiaxiality with  $\kappa = 1$  a mean value of 0.462 is reached, so there is an increase by about 2.1%.

Looking at the upper limits of maximum shear stress, the differences are even clearer. In the uniaxial case there is a natural upper limit at 0.5. Under variation of  $\kappa$  the maximum values go beyond that limit. In the case where  $\kappa = 1$ , the maximum shear stress is at 0.577, which is an increase of about 15.4%.

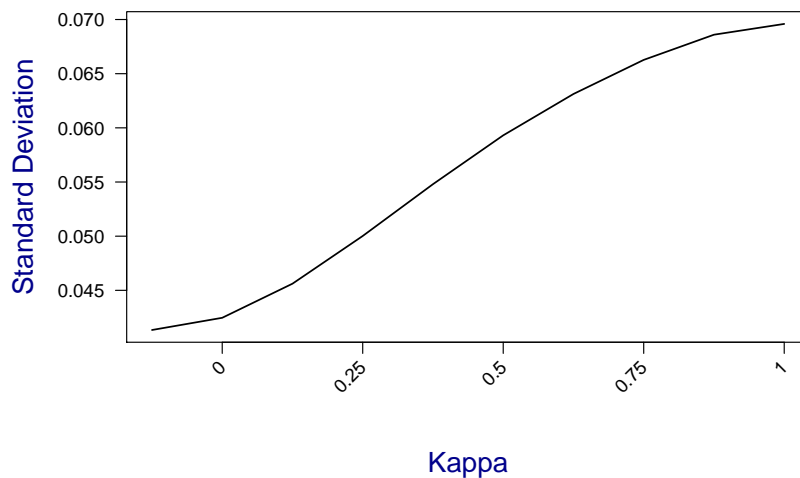


Figure 5.4.: Standard Deviation of  $m(U)$  depending on  $\kappa$

## 5.2. Anisotropic Elasticity

We introduced an approach to calculate maximum shear stress and according distributions under the condition that we consider an isotropic linear material behaviour and a constant global elasticity module  $E$  for all grains, such that with Lamé coefficients

$$\mu = \frac{E}{2(1 + \nu)}, \quad \lambda = \frac{E\nu}{(1 + \nu)(1 - 2\nu)}, \quad (5.7)$$

we calculate the values for the stress tensor via

$$\sigma = \lambda tr(\epsilon)I + 2\mu\epsilon. \quad (5.8)$$

Cubic crystal structures, such as Nickel on a subgranular scale, have orientation depending properties, they are anisotropic. Our isotropy assumptions are based on the fact that we generally consider the component to have a large number of grains in comparison to its size, such that the orientation of the single grains and their impact on material properties are compensated and even out. In the case of Nickel, the grain size is much larger in relation to the specimens, especially compared to other metals like steel. The calculation of shear stress distributions and resulting lifetime distributions supposes an isotropic behaviour of elasticity and a global E module, although we calculate the shear stress locally for each grain.

The following approach includes the anisotropy of E module in the calculation of the shear stress distribution and represents an alternative to the probabilistic Schmid factor model considering an isotropic E module.

In case of isotropic material, the components of the elasticity tensor  $C_{\alpha,\beta}$  as given in 2.12 look the following

$$C_{\alpha,\beta} = \begin{pmatrix} C_{11} & C_{12} & C_{12} & 0 & 0 & 0 \\ C_{12} & C_{11} & C_{12} & 0 & 0 & 0 \\ C_{12} & C_{12} & C_{11} & 0 & 0 & 0 \\ 0 & 0 & 0 & C_{44} & 0 & 0 \\ 0 & 0 & 0 & 0 & C_{44} & 0 \\ 0 & 0 & 0 & 0 & 0 & C_{44} \end{pmatrix} \quad (5.9)$$

where

$$C_{44} = \frac{C_{11} - C_{12}}{2}. \quad (5.10)$$

# Microscopic Damage Accumulation Models

## 5. Grain Orientation and Probabilistic Schmid Factors

---

So it is sufficient to know the values for  $C_{11}$  and  $C_{12}$ . In cubic crystal systems, where the material is generally anisotropic, it holds that

$$C_{44} \neq \frac{C_{11} - C_{12}}{2}. \quad (5.11)$$

In the following we consider the local occurring stress of one grain to be strain controlled.

We consider calculations based on the values of an FEA model to obtain stress tensor  $\sigma_{el,iso} := \sigma_{FE}$  by using an isotropic material law. We use the elastic isotropic stress tensor of the FEA to calculate an elastic isotropic strain tensor

$$\epsilon_{el,iso} = -\frac{\nu}{E} \text{tr}(\sigma_{el,iso})I + \frac{1+\nu}{E} \sigma_{el,iso} \quad (5.12)$$

This strain tensor is then converted into an anisotropic stress tensor. In a standard orientation this is realized by using the elasticity tensor  $C$  and calculate

$$\sigma_{ij} = C_{ijkl}\epsilon_{kl} = C_{ij11}\epsilon_{11} + C_{ij12}\epsilon_{12} + C_{ij13}\epsilon_{13} + C_{ij21}\epsilon_{21} + \dots + C_{ij33}\epsilon_{33}. \quad (5.13)$$

In the following section we calculate the stress tensor according to a random transformation of the elasticity tensor and introduce an additional approach to obtain Schmid factors using anisotropic elasticity.

### 5.2.1. Probabilistic Schmid Factor

We again assume random orientations of the grains and use rotation matrices  $U \in SO(3)$  to transform the elasticity tensor

$$C(U)_{ijkl} = \sum_{p,q,r,s} U_{ip}U_{jq}U_{kr}U_{ls}C_{pqrs}. \quad (5.14)$$

Therewith we can calculate a random anisotropic stress state

$$\sigma(U)_{ani,ij} = \sum_{k,l} C(U)_{ijkl}\epsilon_{el,iso,kl}. \quad (5.15)$$

The randomly oriented anisotropic stress tensor is used for further calculations of the shear stress of slip systems. Therefore we again consider  $n_i$  and  $s_{i,j}$  with  $i \in$

## Microscopic Damage Accumulation Models

### 5. Grain Orientation and Probabilistic Schmid Factors

---

$\{1, 2, 3, 4\}$ ,  $j \in \{1, 2, 3\}$ , being transformed by  $U$ , such that slip planes and systems become randomly oriented as well and we obtain

$$\begin{aligned} n_i(U) &= U n_i, \\ s_{i,j}(U) &= U s_{i,j}. \end{aligned} \quad (5.16)$$

Combining the transformed slip planes and systems as well as the transformed anisotropic stress tensor, we obtain the probabilistic shear stress for  $i$ th slip plane and  $j$ th direction

$$\tau_{ij}(U) = U n_i \cdot \sigma_{ani}(U) \cdot U s_{i,j} \quad (5.17)$$

We insert the transformed anisotropic stress tensor and subsequently the transformed elasticity tensor. We obtain using Einstein notation

$$\begin{aligned} \tau_{ij}(U) &= (U n_i)_v \cdot (\sigma_{ani}(U))_{vw} \cdot (U s_{i,j})_w \\ &= (U n_i)_v \cdot C(U)_{vwkl} \epsilon_{el,iso,kl} \cdot (U s_{i,j})_w \\ &= (U n_i)_v \cdot U_{vr} U_{ws} U_{kt} U_{lu} C_{rstu} \epsilon_{el,iso,kl} \cdot (U s_{i,j})_w \\ &= U_{vr} (n_i)_r U_{vr} U_{ws} U_{kt} U_{lu} C_{rstu} \epsilon_{el,iso,kl} U_{ws} (s_{i,j})_s \\ &= U_{vr}^T U_{vr} (n_i)_r U_{kt} U_{lu} C_{rstu} \epsilon_{el,iso,kl} U_{sw}^T U_{ws} (s_{i,j})_s \\ &= (n_i)_r C_{rstu} U_{tk}^T U_{ul}^T \epsilon_{el,iso,kl} (s_{i,j})_s, \end{aligned} \quad (5.18)$$

where we used for the last equation, that  $U^T U = I$ . With

$$\left( C \epsilon_{el,iso} \left( U^T \right) \right)_{rs} = C_{rstu} \left( \epsilon_{el,iso} \left( U^T \right) \right)_{tu} \quad (5.19)$$

and

$$\left( \epsilon_{el,iso} \left( U^T \right) \right)_{tu} = U_{tk}^T U_{ul}^T \epsilon_{el,iso,kl} \quad (5.20)$$

we obtain

$$\tau_{ij}(U) = n_i C \epsilon_{el,iso} \left( U^T \right) s_{i,j}. \quad (5.21)$$

We again look at the maximum shear stress of all slip systems

$$\tau(U) = \max_{ij} |\tau_{ij}(U)|. \quad (5.22)$$

The resulting random anisotropic maximum shear stress can be used to obtain an alternative probabilistic correcting factor, or probabilistic Schmid factor respectively,

# Microscopic Damage Accumulation Models

## 5. Grain Orientation and Probabilistic Schmid Factors

---

with which we can adjust lifetime calculations. Therefore we again define our adjustment factor as the ratio between maximum anisotropic computed shear stress  $\tau(U)$  and von Mises equivalent stress in the same form as in equation 2.50. In this case our reference stress is given by the elastic isotropic stress tensor and we obtain

$$m(U) = \frac{\tau(U)}{\sqrt{\frac{3}{2}} \|\sigma'_{iso}\|_F}. \quad (5.23)$$

To obtain the distribution of Schmid factors to be transferred to lifetime calculations, we follow the same approach for the rotations as in the isotropic case. The Euler angles are again discretized and weighed according to the Haar measure for  $SO(3)$ . Algorithm 4 shows the different steps of the procedure to obtain probabilistic Schmid factors based on a given isotropic stress state and known material constants. We are interested in the differences between the isotropic and the anisotropic calculation. We further compare the values for different loading states regarding their multiaxiality. After proceeding the simulation with material constants of Nickel at a temperature of  $850^\circ C$  under uniaxial loading we obtain the histogram of figure 5.5.

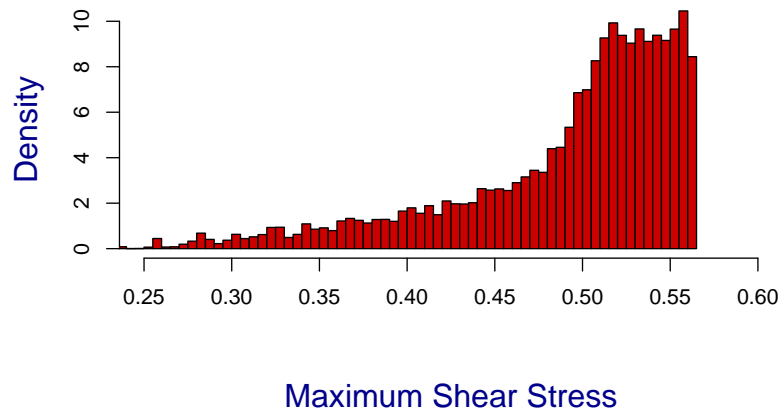


Figure 5.5.: Maximum Shear Stress for Uniaxial Loading State - Anisotropic

The maximum value is at  $m = 0.563$  and therewith almost 13% higher than for the isotropic calculated stress. The values are strongly depending on material constants given for different temperatures. Since we are interested in the behaviour at  $850^\circ C$ , we focus on this case and set the constants of the elasticity tensor to  $C_{11} = 225$ ,  $C_{21} = 161$  and  $C_{44} = 98$  according to the values of the experiment for Rene80. We use an isotropic E module of 145. It is noticeable that the course of the histogram is different

## Microscopic Damage Accumulation Models

### 5. Grain Orientation and Probabilistic Schmid Factors

---

to the isotropic one. There is a slight difference of maximum values as well as a lower limit of the anisotropic calculated Schmid factors which is smaller than the isotropic one. The values of the anisotropic calculation are shifted to the left and the deviation is larger. Table 5.1 shows the summary of both variants.

Schmid Factor	Min.	1st Qua.	Median	Mean	3rd Qua.	Max.
Isotropic	0.2746	0.4349	0.4621	0.4523	0.4835	0.5
Anisotropic	0.2361	0.4648	0.5118	0.4916	0.5383	0.563

Table 5.1.: Summary of Schmid Factors - Isotropic and Anisotropic Uniaxial

We see the differences in the mean value with a value being about 0.039 higher than the isotropic calculated Schmid factors, which corresponds to a percentage deviation upwards by 8.7%. Also the differences in range and the right shift of the values in the anisotropic case are indicated. In the multiaxial case, where  $\kappa = 1$ , the distribution looks similar to the isotropic one at first glance. Figure 5.6 shows the histogram. The standard deviation is noticeably higher than under uniaxial loading and the mean is again shifted to the right. There is a maximum value of 0.65, which is much higher compared to the maximum value of 0.5772 for the isotropic calculated shear stresses.

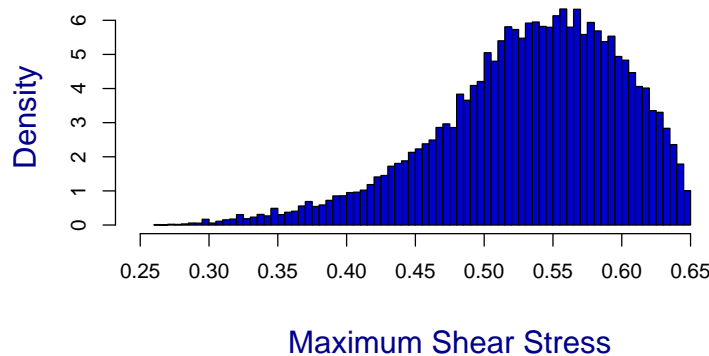


Figure 5.6.: Maximum Shear Stress, Anisotropic, Multiaxial  
 $\kappa = 1$

The standard deviation and mean values for different levels of multiaxiality are shown in figures 5.7 and 5.9. The mean value increases with the amount of multiaxiality. The mean value for  $\kappa = 1$  is 8.5% higher than under uniaxial loading.

# Microscopic Damage Accumulation Models

## 5. Grain Orientation and Probabilistic Schmid Factors

---

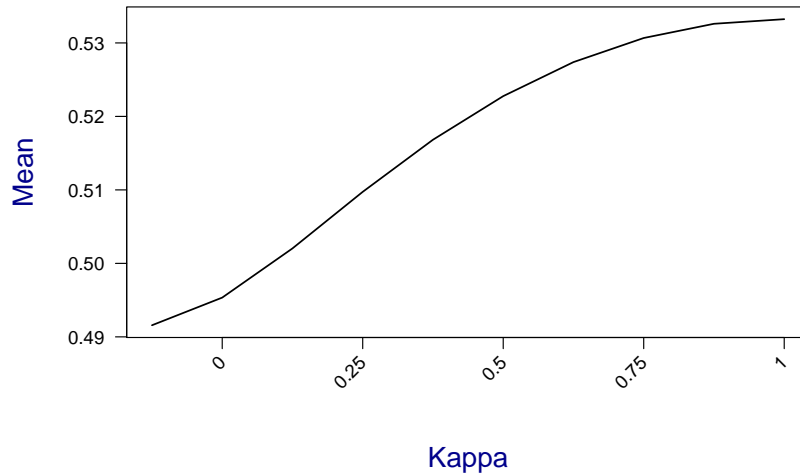


Figure 5.7.: Mean depending on  $\kappa$ , Anisotropic

If we compare the change of mean value under multiaxial loading between the isotropic and anisotropic case, it is noticeable that the percentage increase of the mean of Schmid factors based on an isotropic calculation is about four times lower than the change under anisotropic conditions. Both changes in mean are in the same direction, but the anisotropic calculation is much more sensitive to increases of multiaxiality.

Figure 5.8 shows both courses in comparison, where the remarkable differences are illustrated. The mean in the anisotropic case is already higher for uniaxial loading, which can also be seen in table 5.1 and figure 5.8, as this is the case for the slope. For the highest multiaxiality where  $\kappa = 1$  anisotropic calculated Schmid factors have higher means.

# Microscopic Damage Accumulation Models

## 5. Grain Orientation and Probabilistic Schmid Factors

---

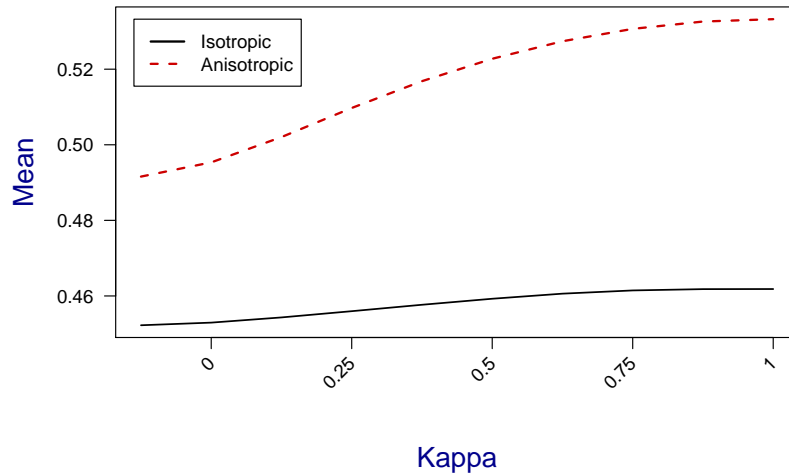


Figure 5.8.: Comparison of Mean of Isotropic and Anisotropic Schmid Factors

The values of standard deviation also show an increasing course. The scatter increases under a larger amount of multiaxiality. But under consideration of the scale the values do not differ a lot from each other for varying levels of multiaxiality. At  $\kappa = 0.25$  and  $\kappa = 0.5$  the values are slightly different only. For an increasing multiaxiality represented by  $\kappa$ , the values for Schmid factors scatter more, but the differences of standard deviation with  $\kappa = 1$  to the uniaxial case need to be compared to those of the isotropic calculation. The standard deviation of both variants can be seen in figure 5.9. In comparison to the isotropic calculation the scatter increases only minimally under multiaxial loading.

# Microscopic Damage Accumulation Models

## 5. Grain Orientation and Probabilistic Schmid Factors

---

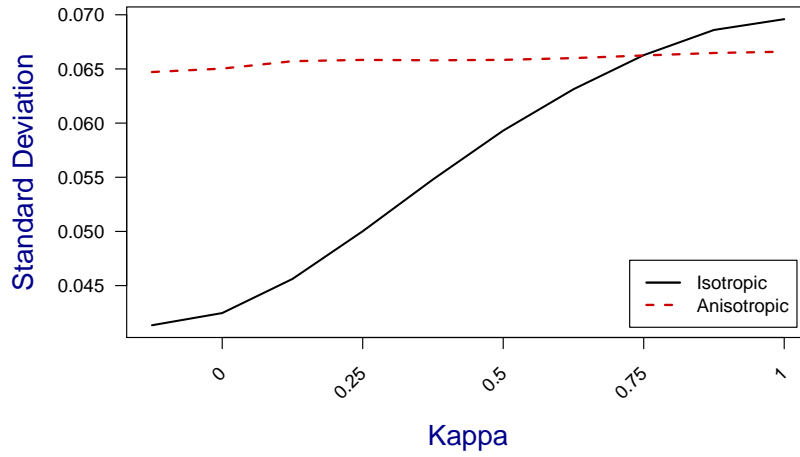


Figure 5.9.: Comparison of Standard Deviation of Isotropic and Anisotropic Schmid Factors

Table 5.2 contains the values of the summary. In the multiaxial case, the isotropic calculated Schmid factor has a lower 1st Quartile.

Schmid Factor	Min.	1st Qua.	Median	Mean	3rd Qua.	Max.
Isotropic	0.2431	0.4101	0.4760	0.4620	0.5179	0.5772
Anisotropic	0.2609	0.4945	0.5411	0.5332	0.5831	0.6499

Table 5.2.: Summary of Schmid Factors - Isotropic and Anisotropic  
 $\kappa = 1$

The mean values differ by 0.08, which is a percentage deviation upwards by 17.9% calculating the shear stress anisotropic.

## 6. Probabilistic LCF Life for Single Grains

We introduced different approaches to calculate maximum shear stress and according distributions either based on an isotropic E module or on an anisotropic one. The comparison of both distributions for different levels of multiaxiality indicates differences in scatter and location.

The shift of means and an increase of standard deviation of maximum shear stress within a grain also influences the time until plastical deformation occurs and therefore its lifetime. A deterministic approach according to section 3.1 is standard because of the practical applicability, but it is not really appropriate, as the lifetime results of testing even under equal loading conditions scatter a lot and the curve does not exactly fit the data.

Including the random orientation of grains allows us to consider distributions of shear stress at different given stress levels. Additionally, we have the possibility to include several levels of multiaxiality as well as an anisotropic behaviour of the elasticity tensor  $C$ .

In the following section we present an approach to calculate the lifetime to failure based on probabilistic shear stress. Thereby we use the distributions of Schmid factors for different strengths of multiaxiality and compare the results from calculations based on an isotropic and an anisotropic material law.

We use reliability statistics to model local fatigue life and use the probabilistic models of the previous section. We follow [19] and [27].

We are interested in the time to crack initiation and therefore consider  $T$  to be a continuous random variable on some probability space  $(\Omega, \mathcal{A}, \mathbb{P})$  with values in  $\mathbb{R}^+$ . We will later on use the discrete number of cycles to failure  $n$  instead of  $t$ . Further, consider the corresponding cumulative densities function to be given by

## Microscopic Damage Accumulation Models

### 6. Probabilistic LCF Life for Single Grains

---

$F_T = \mathbb{P}(T \leq t)$  and the underlying density  $f_T(t) = \frac{\partial}{\partial t} F_T(t)$ . The according **hazard function** describing the current rate of failure at time  $t$  is defined as

$$h(t) = \lim_{\Delta t \rightarrow 0} \frac{\mathbb{P}(t < T < t + \Delta t | T > t)}{\Delta t}. \quad (6.1)$$

The respective cumulative hazard function is defined as

$$H(t) = \int_0^t h(s) ds. \quad (6.2)$$

The function giving the probability of survival up to time  $t$  is given by the survival function

$$S_T(t) = \exp(-H(t)), \quad (6.3)$$

which can also be calculated with the according probability of failure as

$$S_T(t) = 1 - F_T(t). \quad (6.4)$$

It holds that

$$h(t) = \frac{f_T(t)}{1 - F_T(t)} = -\frac{\partial}{\partial t} \log S_T(t). \quad (6.5)$$

We are interested in the LCF failure mechanisms of a polycrystalline component. Therefore consider a geometry  $\Omega \subset \mathbb{R}^3$  with an arbitrary partition of pairwise disjoint  $\{A_i\}_{i=1, \dots, m}$  of the boundary  $\partial\Omega$ , such that

$$\partial\Omega = \bigcup_{i=1}^m A_i. \quad (6.6)$$

We consider the failure time on each  $A_i$  to be independent and further let  $\{T_i\}_{i=1, \dots, m}$  be iid. random variables describing the time to crack initiation for each set  $A_i$  with according hazard functions  $h_i$ ,  $i = 1, \dots, m$ .

To obtain the first time to crack initiation over the whole boundary of the geometry we consider  $T = \min(T_1, \dots, T_m)$ . Since for independent  $T_i, T_j$  with respective  $h_i, h_j$  we can calculate the hazard of  $\min(T_i, T_j)$  via  $h_i + h_j$ , the hazard function of  $T$  is given by

$$h = \sum_{i=1}^m h_i. \quad (6.7)$$

Additionally we consider for any measurable surface region  $A \subseteq \partial\Omega$  that the hazard function of the respective area at time  $t$  can be calculated with an appropriate hazard

# Microscopic Damage Accumulation Models

## 6. Probabilistic LCF Life for Single Grains

---

density function  $\rho$  taking into account the number of grains  $N$ , the displacement field  $u$  induced by the underlying stress state  $\sigma$  and the critical crack size  $L_C$  as

$$h_A(t) = \int_A \rho(t, N, \sigma, L_C) dA. \quad (6.8)$$

We consider a subset of the surface  $A \subset \partial\Omega$ , which we subdivide into  $k$  equal sized subsets again with surface sizes

$$|A_i| = \frac{|A|}{k}, i = 1, \dots, k. \quad (6.9)$$

Let the applied load be approximately constant and equal overall surface subsets, which results in  $h_{A_i} \approx h_{A_j}$  for  $i, j = 1, \dots, k$ . We obtain for the hazard of the arbitrary subset  $A$  that

$$\begin{aligned} h_A &= \sum_{i=1}^k h_{A_i} \\ &\approx k \cdot h_{A_1} \\ &= \frac{|A|}{|A_1|} h_{A_1}. \end{aligned} \quad (6.10)$$

For  $k \rightarrow \infty$  the hazard density function becomes

$$\rho = \lim_{k \rightarrow \infty} k \cdot \frac{h_{A_1}}{|A_1|} \quad (6.11)$$

and  $h \approx A \cdot \rho$ .

With the assumptions made, we obtain the hazard function for the whole geometry as

$$h(t) = \int_{\partial\Omega} \rho(t, N, \sigma, L_C) dA. \quad (6.12)$$

Therewith, we can calculate the probability of failure for LCF initiation of crack until time or cycle  $t$  via

$$\begin{aligned} F_T(t) &= 1 - \exp(-H(t)) \\ &= 1 - \exp\left(-\int_0^t h(s) ds\right) \\ &= 1 - \exp\left(-\int_0^t \int_{\partial\Omega} \rho(t, N, \sigma, L_C) dAdt\right) \end{aligned} \quad (6.13)$$

We now discuss the form of the hazard density function  $\rho$  in case of a single grain and will later on extend this to multiple grains. Therefore we first calculate the probability of failure for one grain depending on a given loading state and strain amplitude. We recapitulate the relation between stress and strain amplitude being described

# Microscopic Damage Accumulation Models

## 6. Probabilistic LCF Life for Single Grains

---

by the Ramberg-Osgood equation in (2.23). and the Coffin-Manson-Basquin equation in (3.5) describing the strain to life relation. To obtain the number of load cycles to crack initiation based on a given strain amplitude, the equation needs to be inverted, e.g. this can be realised by using a spline-approximation. So we again consider the inverse of the Coffin-Manson-Basquin equation in 3.6 and the inverse of the Ramberg-Osgood equation

$$RO^{-1}(\epsilon_a) = \sigma_a. \quad (6.14)$$

The material functions are usually used for a deterministic calculation of fatigue life for an applied strain amplitude and given material constants. We now use these relations to calculate probabilistic fatigue life. Therefore we make use of the probabilistic shear stresses as we have introduced in chapter 5.1.

The strain amplitudes scatter because of the random grain orientation, such that we do not know which strain can appropriately be used for the Coffin-Manson-Basquin equation.

Hence, we use the Schmid factors to adjust stress and strain amplitudes. The Schmid factors can be calculated by

$$m(U) = \frac{\tau(U)}{\sqrt{\frac{3}{2}} \cdot \|\sigma'\|_F}. \quad (6.15)$$

We want to use an adjustment factor, which locally measures the deviation from the expectational value in the uniaxial case. Now let

$$\lambda = \mathbb{E}_U[m(U)]. \quad (6.16)$$

As we do mostly consider strain controlled fatigue testing we now use the inverse of the Ramberg-Osgood equation to compute the corresponding stress amplitude, which is then corrected with the adjustment factor

$$\sigma_a^{ad}(U) = \frac{m(U)}{\lambda} RO^{-1}(\epsilon_a). \quad (6.17)$$

Therewith we compute the probabilistic strain amplitude

$$\epsilon_a(U) = RO(\sigma_a^{ad}(U)). \quad (6.18)$$

# Microscopic Damage Accumulation Models

## 6. Probabilistic LCF Life for Single Grains

---

Finally, we obtain a random fatigue lifetime via

$$\begin{aligned} N_i(U) &= CMB^{-1}(\epsilon_a(U)) \\ &= CMB^{-1}\left(RO\left(\sigma_a^{ad}(U)\right)\right) \\ &= CMB^{-1}\left(RO\left(RO^{-1}(\epsilon_a) \cdot \frac{m(U)}{\lambda}\right)\right). \end{aligned} \tag{6.19}$$

Therewith, we can calculate the probability of LCF failure as

$$\begin{aligned} &\mathbb{P}(N_i(U) \leq n) \\ &= \mathbb{P}(CMB^{-1}(\epsilon_a(U)) \leq n) \\ &= \mathbb{P}(CMB^{-1}\left(RO\left(\sigma_a^{ad}(U)\right)\right) \leq n) \\ &= \mathbb{P}\left(CMB^{-1}\left(RO\left(RO^{-1}(\epsilon_a) \cdot \frac{m(U)}{\lambda}\right)\right) \leq n\right). \end{aligned} \tag{6.20}$$

Let the distribution function of Schmid factors  $m(U)$  be denoted by

$$F_{SF}(n) = \mathbb{P}\left(CMB^{-1}\left(RO\left(RO^{-1}(\epsilon_a) \cdot \frac{m(U)}{\lambda}\right)\right) \leq n\right). \tag{6.21}$$

and the corresponding density function by

$$f_{SF}(n) = \frac{\partial}{\partial n} F_{SF}(n). \tag{6.22}$$

The distribution of Schmid factors represents the probability of failure for one grain at cycle  $n$ . The survival function  $S_{SF}(n)$  can be computed as given in 6.4 and for the hazard function  $h_{SF}(n)$  we obtain 6.5. These functions can be used to compute reliability values for single grains applying different stress or strain states. As the setting of of the Schmid factor calculations enable computations for arbitrary crystal structure types, these values can be obtained for different materials.

We have seen that depending on the level of multiaxiality the Schmid factors distributions deviate a lot and we hereby have a possibility to include these effects in the fatigue lifetime calculations. The following section shows the results of the transfer of the probabilistic Schmid factors to LCF fatigue lifetime.

### 6.1. Single Grain Life for fcc Crystals

In this section we use the results of chapter 5.1 to calculate LCF fatigue lifetime in case of the face-centered cubic crystal. We consider a single grain first, the next

# Microscopic Damage Accumulation Models

## 6. Probabilistic LCF Life for Single Grains

---

chapter shows the transfer to multigrain models and the impacts on lifetime calculations. The material parameters, which we use, were provided by Siemens and will not be stated explicitly.

We have seen that the different levels of multiaxiality imply different Schmid factor distributions. The means are shifted and the scatter varies significantly. We first consider an uniaxial loading state with an applied strain amplitude of 0.2% and appropriate material parameter. Figure 6.1 shows the lifetime distribution of a single grain.

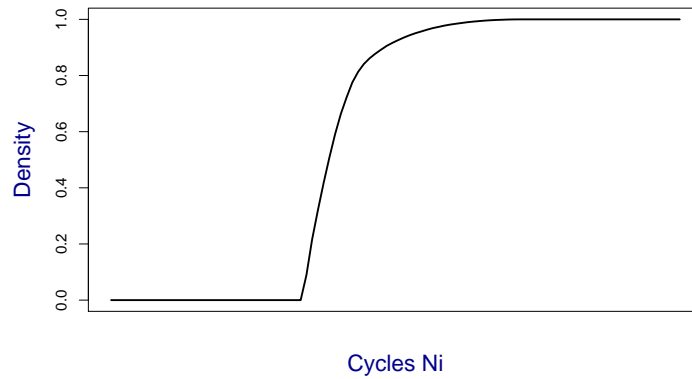


Figure 6.1.: Lifetime Distribution Uniaxial

We can see that there is a high increase within an area of  $N_i = 10^{3.5}$  and  $N_i = 10^{4.5}$ . The corresponding density function is shown in figure 6.2.

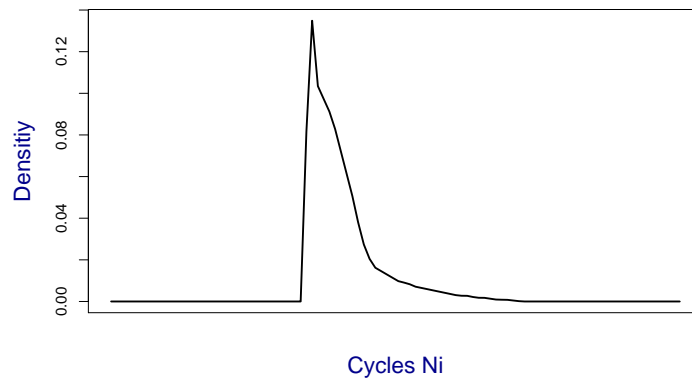


Figure 6.2.: Lifetime Density Function Uniaxial

# Microscopic Damage Accumulation Models

## 6. Probabilistic LCF Life for Single Grains

---

As it is noticeable in the figure, the course of the density of single grain LCF fatigue life is a result of the Schmid factor density. There is a big mass within a small area such that the density becomes acute. This results from the small range of the Schmid factors. The sharp upper limit of the Schmid factors becomes a lower one for LCF lifetime.

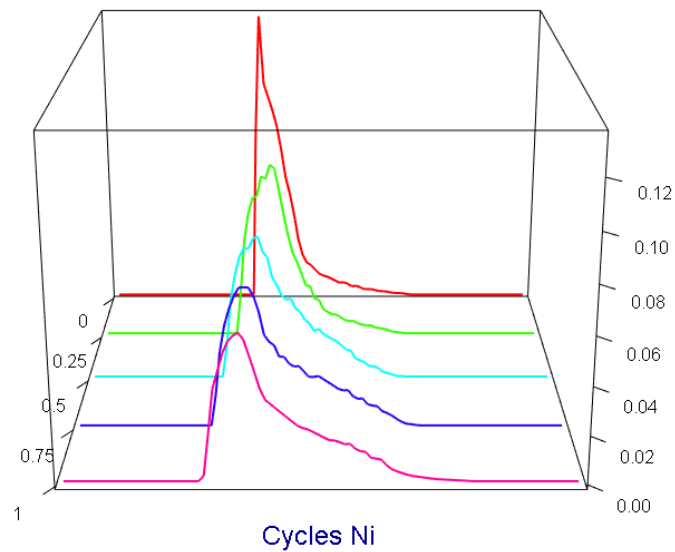


Figure 6.3.: Lifetime Densities Multiaxial

Figure 6.3 shows the densities of lifetime distributions under different levels of multiaxiality with  $\kappa \in [0, 1]$ . The red line is the density according to the uniaxial case, i.e.  $\kappa = 0$ , which has already been shown in figure 6.2.

It is noticeable that the curves deviate between different amounts of multiaxiality. The distributions scatter more and the minimum values are shifted to the left. These effects closely correspond those of the Schmid factors. As the maximum values of shear stress increase, the minimum of fatigue lifetime decreases.

The according distributions are given in figure 6.4.

6. Probabilistic LCF Life for Single Grains

---

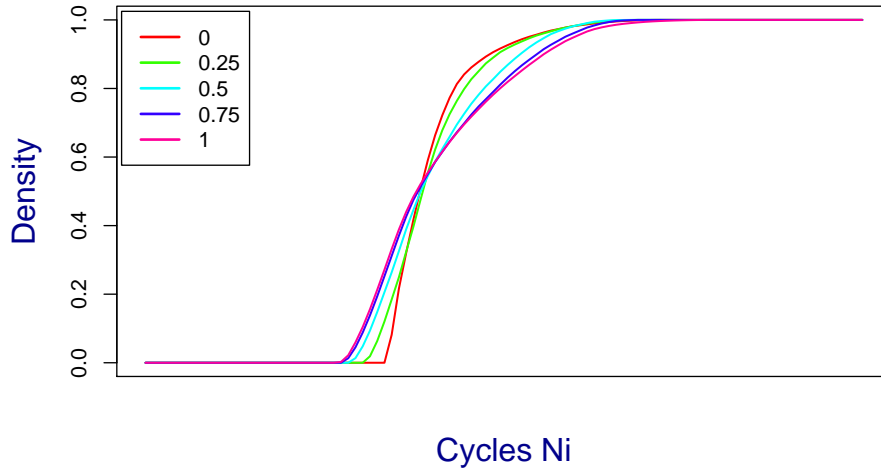


Figure 6.4.: Lifetime Distribution Multiaxial

Figure 6.5 shows the change in minimum value for an increasing multi-axiality. In mean the number of cycles to fatigue  $N_i$  change slightly only as one can see in table 6.1. They stay in a range of  $10^{4.67}$  and  $10^{4.95}$  and even increase by a small amount comparing the values of  $\kappa = 0$  to those of  $\kappa = 1$ , but there is a left-shift of the range in general and an accompanying increase in scatter by raising the amount of multi-axiality. Therewith, multi-axiality changes the lifetime of single fcc grains. As usually, the amplitude of von Mises stress is taken as a reference value, the risk of failure can be underestimated.

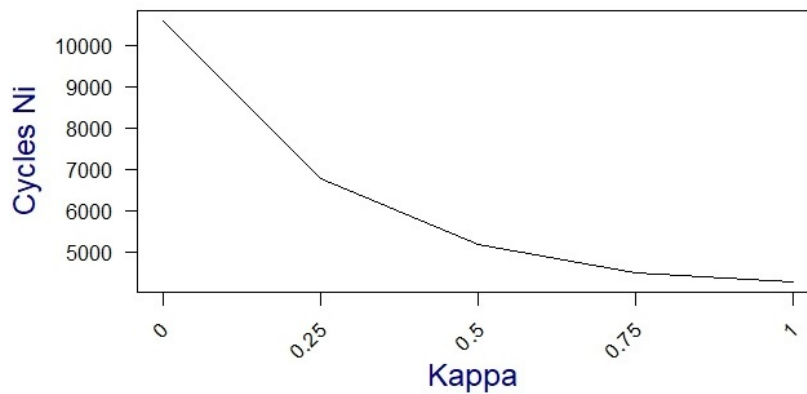


Figure 6.5.: Mean of Fatigue Life Multiaxial

# Microscopic Damage Accumulation Models

## 6. Probabilistic LCF Life for Single Grains

---

Fatigue Life	Min.	1st Qua.	Median	Mean	3rd Qua.	Max.
Uniaxial	10590	13790	19850	46780	32900	2044000
Multiaxial	4269	9501	18520	89530	65300	6121000

Table 6.1.: Summary of Fatigue Life - Uniaxial and Multiaxial

Table 6.1 shows the deviation of the number of cycles to fatigue between the uniaxial and the multiaxial loading state where  $\kappa = 1$ . The mean of fatigue life under high multiaxial loading conditions reaches 89530 cycles. The maximum value in the uniaxial case is 2044000 and 6121000 in the multiaxial. The minimum of fatigue lifetime is at 4269 cycles, the minimum number of cycles in the uniaxial case is 10590 and therewith almost 2.5 times higher than under multiaxial loading conditions.

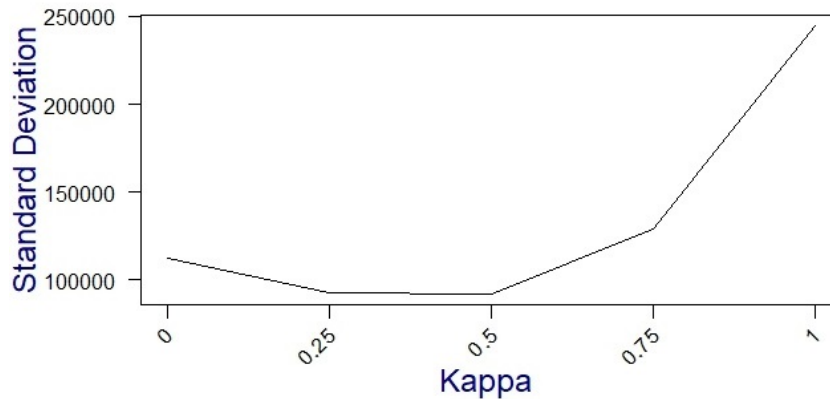


Figure 6.6.: SD of Fatigue Life Multiaxial

Although the equivalent stress is at the same level, we obtain very different lifetime distributions and according densities for a single grain fatigue. Generally speaking, the shift of minimum values tends to lower life values resulting from the right-shift of shear stress under multiaxial loading. Also the scatter in life increases at higher levels of multiaxiality. To which effects the slip system based approach leads in multigrain models will be shown in chapter 7.

Single grain fatigue can also be calculated for an anisotropic E module. The intention behind using an anisotropic E module as well as the combination with a slip system based approach was discussed in chapter 5.2. We use the resulting Schmid factor distributions to compute single grain life for different levels of multiaxiality and compare them to the results of those based on an isotropic calculation.

# Microscopic Damage Accumulation Models

## 6. Probabilistic LCF Life for Single Grains

---

A comparison of LCF fatigue life distribution is given in 6.7. The anisotropic calculated distribution increases at a smaller number of cycles than the isotropic one. Therefore it is flatter and has a larger range in total.

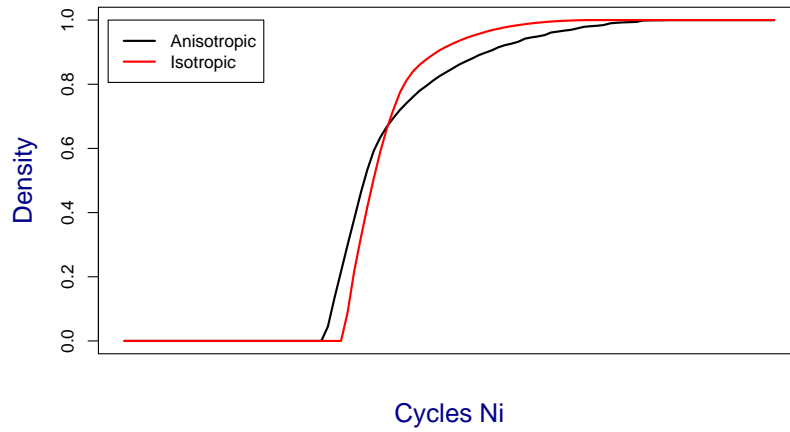


Figure 6.7.: Lifetime Distributions Uniaxial

Looking at the density under multiaxial loading, we see that it has a strong increase, but is although lower and not as sharp as the density in the isotropic case, which can be seen in a direct comparison in figure 6.9. Figure 6.8 shows the density in the anisotropic case for an uniaxial loading state.

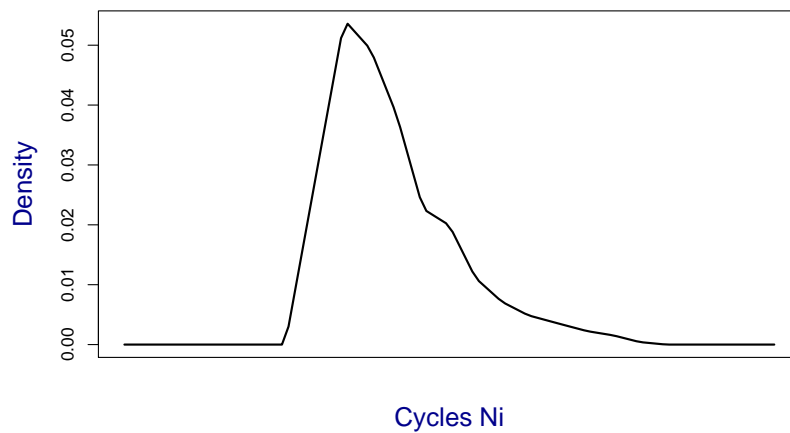


Figure 6.8.: Lifetime Density for  $\kappa = 1$  - Anisotropic

# Microscopic Damage Accumulation Models

## 6. Probabilistic LCF Life for Single Grains

---

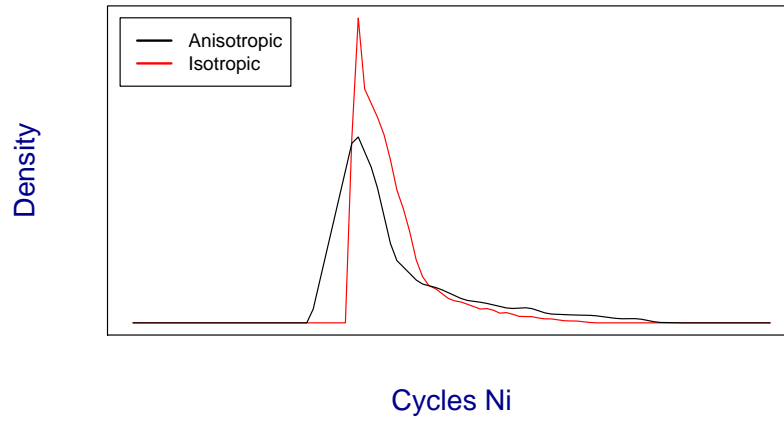


Figure 6.9.: Lifetime Densities Comparison

Now we discuss the influence of multiaxiality on the density. Therefore we variate  $\kappa$  and generate the according LCF fatigue life distributions. Figure 6.10 shows the densities of 5 different values of  $\kappa \in [0, 1]$ .

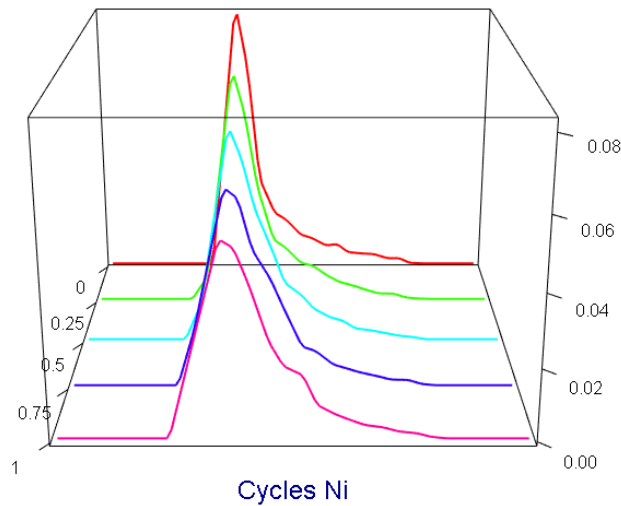


Figure 6.10.: Lifetime Densities Multiaxial - Anisotropic

The densities show similar changes to the isotropic calculated densities. They are shifted to the left, the minimum life is shorter. The standard deviation increases as well, but can see bigger differences only for  $\kappa \geq 0.75$ .

6. Probabilistic LCF Life for Single Grains

---

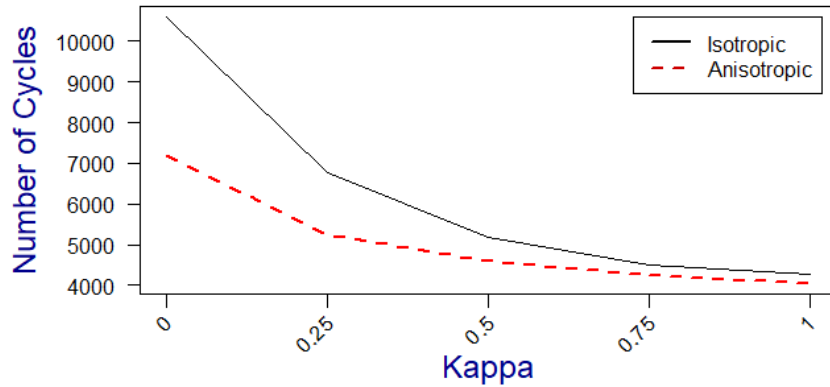


Figure 6.11.: Minimum of Fatigue Life Multiaxial

Figure 6.11 shows the comparison between the change in the minimum value for different levels of multiaxiality in the isotropic and the anisotropic case. It is noticeable that the minimum value decreases for both calculations. For  $\kappa = 0.25$  we already have a decrease of 36% in the isotropic case and about 25% in the anisotropic one. The minimum value for  $\kappa = 1$  is changed by 60% and 37%, they fall to 4268 and 5095 cycles.

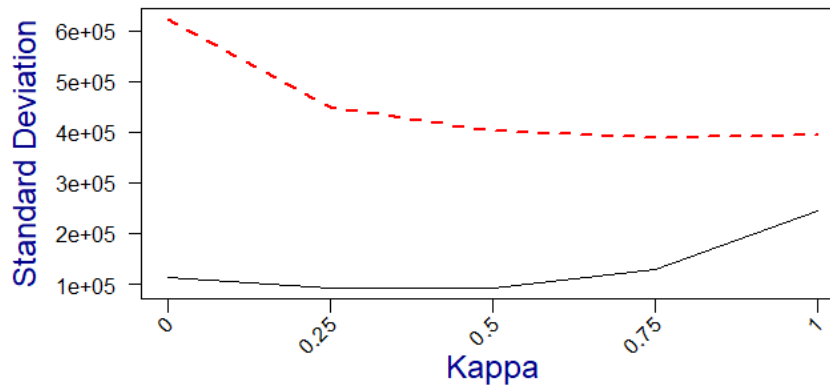


Figure 6.12.: Comparison Standard Deviation

Comparing the mean values and standard deviation of both single life distributions for  $\kappa \in [0, 1]$  we notice effects, which arise from those of the Schmid factor distributions. Since we standardize with the expectational value for lifetime calculation, the effects weaken. In the anisotropic case we notice a slightly decreasing number of cycles for the mean value from 156771 to 110640 cycles, therefore the standard deviation also falls from about 621881 to 392814 cycles. In the isotropic case the mean value increases, in the uniaxial case the mean number of cycles is 46782 and in the highest multiaxial case where  $\kappa = 1$  we have 89525. The standard deviation

## Microscopic Damage Accumulation Models

### *6. Probabilistic LCF Life for Single Grains*

---

increases from 112210 to 244479 cycles.

Therewith we in general have a lower mean number of cycles to fatigue in the uniaxial case. This value slightly increases under multiaxial loading, but therefore the standard deviation also increases, since the number of cycles scatter more. This is also noticeable looking at development of the minimum values of figure 6.11. Although there are small changes in the mean value of the number of cycles to fatigue, the bandwidth becomes wider, such that the minimum value is shifted from 10 587 to 4 269 cycles.

In the anisotropic case we see that the mean becomes smaller when the loading becomes more multiaxial. Therefore the scatter decreases and the standard deviation changes downwards. It is noticeable that the values in the isotropic case are in general below those of the anisotropic one.

Since we have seen how the Schmid factor distributions influence the lifetime of a single grain, the following chapter shows different approaches to obtain multi-grain models. Additionally, different fatigue criteria are introduced and the models are used to calculate probabilities of failure for various grain and crack sizes to get insights in the mechanisms of failure depending on the grain morphology.

## 7. Crack Propagation and Grain Morphology

We investigated the material behaviour depending on the state of stress applied with focus on multiaxial load states for a single grain. Here the results are extended to multiple grains, since the component build of polycrystalline material consists of numerous grains showing interdependencies, which are analyzed in the following.

It is necessary to have an insight into the interactions between the different grains, especially at the grain boundaries, to understand how an initiated crack percolates to another grain and which factors influence the crack propagation in detail. An important quantity we look at is the grain size, which can to a certain extend be controlled by the cooling rate.

We consider randomly distributed and twisted grains, since we do neither know the exact distribution nor the orientation of the grains in the component. We use a

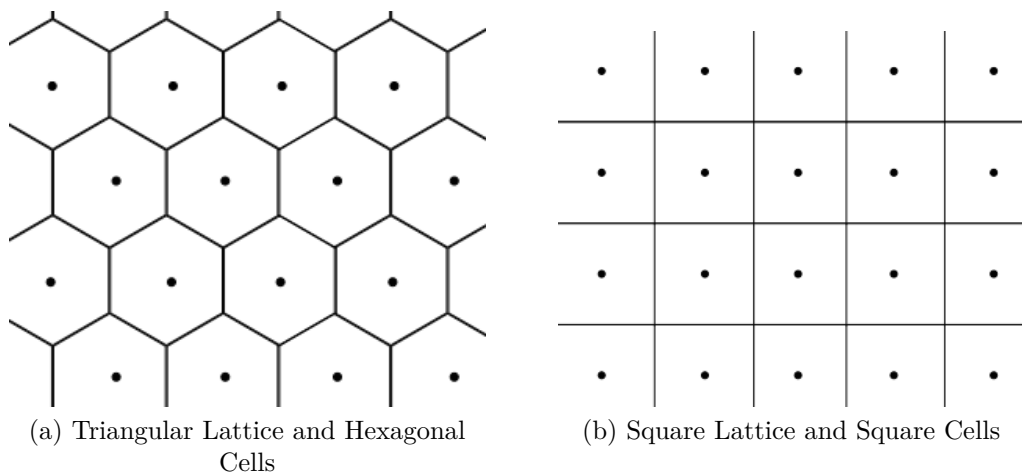


Figure 7.1.: Regular Lattices and their Voronoi Cells

so-called cell model to describe the microstructure of the polycrystal, which is very common in case of random heterogeneous material (see [33, 8] for example). In this regard we introduce Voronoi tessellations, which are used to partition spaces of dimension  $d$  into  $d$ -dimensional (convex) cells with either deterministic equidistant or

# Microscopic Damage Accumulation Models

## 7. Crack Propagation and Grain Morphology

---

random points.

The partitioning of finite type (Voronoi diagram) or extending to all of space with its several forms are used very frequently, as these cell models represent plentiful materials having cellular microstructure appropriately and simplify answering required questions such as finding nearest neighbours for given point sets.

Let  $G = (V, E)$  be a graph with finite number of vertices  $V$  and corresponding edges  $E \subseteq \{(u, v) | u, v \in V, u \neq v\}$  with elements  $e \in E$  of the form  $e = (u, v)$ ,  $u, v \in V, u \neq v$ . Further let  $N, F \in \mathbb{N}$  be the number of cells and the number of faces respectively. Figures 7.1a and 7.1b show typical tile patterns in two dimensions resulting in shapes of equal size and form. We focus on the square lattice to describe the composition of grains of the material, where each square cell relates to a grain with respective neighbouring cells. We consider an area of size  $A$  and cells of length  $L_G$  such that the number of cells in the area is calculated as  $N = \frac{A}{L_G^2}$ . We first look at the one-dimensional case with  $N$  cells in a row and a crack enabled to grow in one direction only.

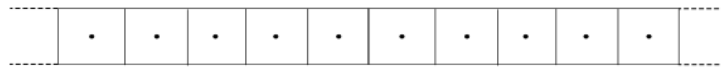


Figure 7.2.: Cubic Lattice in One Dimension

Furthermore, consider a critical crack length of size  $L_C$ . The number of cells, which need to be cracked until reaching the critical crack length, is given as  $n_C = \frac{L_C}{L_G}$ . Looking at a finite grid there are a multiple possibilities for a crack of size  $L_C$ , i.e. a chain of cells showing a crack in a row, which we will call cluster of size  $n_C$  for simplification reasons.



Figure 7.3.: Possible Positions for a Crack  $L_C = 2L_G$

Consider the cells being numbered in an ascending manner from left to right. The crack of size  $L_C$  with  $n_C$  cracked grains in a row can be shifted from the first left

# Microscopic Damage Accumulation Models

## 7. Crack Propagation and Grain Morphology

---

cell to the cell with position  $N - L_C + 1$ , as at least  $n_C$  cells need to be cracked in a row after the observed cracked one. Beginning from the first one, we go through the cells from left to right and stop once a cluster showing a crack with a minimum size of  $n_c$  is observed. So we are looking for the probability that the first crack with a minimum size of  $L_C$  begins in grain  $k = 1, \dots, N - n_C + 1$ .

### 7.1. Modified Percolation Models

The investigation in the occurrence of cracks showing a given critical length is closely related to questions regarding percolation theory, i.e. the occupancy and transfer within graphs with certain initial conditions. Some basics are for example shown in [24].

For the sake of simplification, we consider the vertices as centers of the grains and  $v_i \in \mathbb{Z}^2$ ,  $i=1, \dots, N$  with  $\sum_{j=1}^2 |v_{ij} - v_{kj}| = 1$ ,  $i \neq k$ . In this context let the set of all edges of neighbored cells be

$$E' := \left\{ (v_i, v_k) \mid v_i, v_k \in \mathbb{Z}^2, i, k = 1, \dots, N, i \neq k, \|v_i - v_k\|_1 = 1 \right\}. \quad (7.1)$$

Thus, we obtain the graph  $G = (V', E')$  with vertices  $V'$  and edges  $E'$  as defined with  $|V'| = N$  cells and  $|E'| = m$  edges. We first consider the chain-type grain structure, so let the second coordinate be fixed.

With probability  $p \in [0, 1]$  each vertex can crack and a sequence of  $s$  cracked grains is again called  $s$ -cluster, so a set of active vertices being connected by edges. This percolation type is also known as **site percolation**.

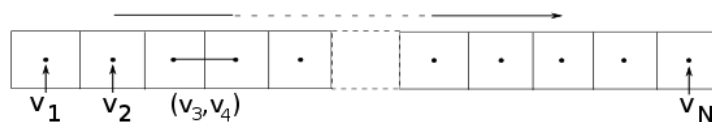


Figure 7.4.: Graph for One Dimension

This can be represented by  $N$  i.i.d. random variables  $(X_k)_{k=1, \dots, N}$  on  $(\Omega, \mathcal{A}, \mathbb{P})$  with

$$\Omega := \{\omega = (\omega_k)_{k=1, \dots, N} \mid \omega_k \in \{0, 1\}\} = \{0, 1\}^N \quad (7.2)$$

A vertex number  $k$  of graph  $G$  can be either cracked,

$$X_k(\omega) = \omega_k = 1 \quad (7.3)$$



# Microscopic Damage Accumulation Models

## 7. Crack Propagation and Grain Morphology

---

For grain  $k \in \{2, \dots, N - s + 1\}$  we can formulate the cumulated crack probabilities recursively,

$$\begin{aligned} \mathbb{P}(C_{\min}(n_C, \omega) \leq k) &= (1 - \mathbb{P}(C_{\min}(n_C, \omega) \leq k - 2)) (1 - p)^{n_C} \\ &\quad + \mathbb{P}(C_{\min}(n_C, \omega) \leq k - 1), \end{aligned} \quad (7.10)$$

since grain  $k - 2$  can not be the minimum starting point for a  $n_C$ -crack and grain  $k - 1$  needs to be not cracked, as otherwise the cluster's starting point would not be in  $k$ . This can be visualized

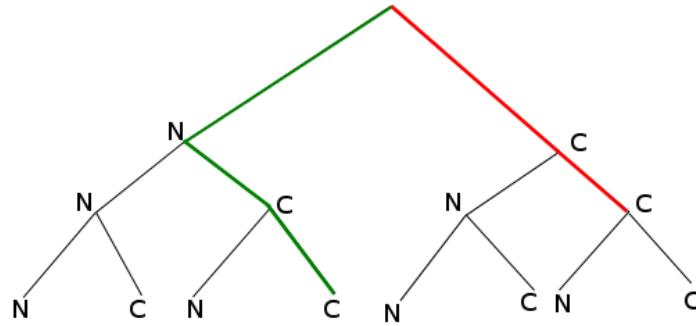


Figure 7.6.: Crack Possibilities for  $n_C = 2$  and  $N = 3$

In order to obtain solutions for the crack probabilities we transfer it to approaches to solve recurrence relations.

### 7.1.1. Recurrence Relation of Crack Probability

The probability for cracks of a given critical length  $n_C$  can be formulated recursively. We consider a chain-type graph  $G = (V', E')$  as defined in (7.1) and its grains from left to right, i.e.  $k = 1, \dots, N - n_C + 1$ . The problem can be represented as in equations (7.8), (7.9) and (7.10). We use the introduced fundamentals as given in 4.2.

Let

$$C_k(n_C) := \mathbb{P}(C_{\min}(n_C, \omega) \leq k) \quad (7.11)$$

for  $k \in \{2, \dots, N - n_C + 1\}$  with

$$\begin{aligned} C_0(n_C) &= 0 \\ C_1(n_C) &= p^{n_C}, \end{aligned} \quad (7.12)$$

## Microscopic Damage Accumulation Models

### 7. Crack Propagation and Grain Morphology

---

then  $C_k(n_C)$  can be obtained by

$$C_k(n_C) = (1 - C_{k-2}(n_C))(1 - p)p^{n_C} + C_{k-1}(n_C). \quad (7.13)$$

This corresponds to an inhomogeneous recurrence equation of second order and can be easily seen after rearranging as follows

$$C_k(n_C) - C_{k-1}(n_C) + (1 - p)p^{n_C}C_{k-2}(n_C) = (1 - p)p^{n_C} := \tilde{p} \quad (7.14)$$

and initial conditions as given in (7.12). This can also be represented by

$$\begin{pmatrix} 1 & 0 & 0 & 0 & \cdots & 0 & 0 & 0 \\ -1 & 1 & 0 & 0 & \cdots & 0 & 0 & 0 \\ \tilde{p} & -1 & 1 & 0 & \cdots & 0 & 0 & 0 \\ 0 & \tilde{p} & -1 & 1 & \cdots & 0 & 0 & 0 \\ \vdots & \vdots & \ddots & \ddots & \ddots & \vdots & \vdots & \vdots \\ 0 & 0 & 0 & 0 & \cdots & \tilde{p} & -1 & 1 \end{pmatrix} \cdot \begin{pmatrix} C_0 \\ C_1 \\ C_2 \\ C_3 \\ \vdots \\ C_k \end{pmatrix} = \begin{pmatrix} 0 \\ p^{n_C} \\ \tilde{p} \\ \tilde{p} \\ \vdots \\ \tilde{p} \end{pmatrix}, \quad (7.15)$$

and in short form

$$Ax = b, \quad (7.16)$$

where

$$A := \begin{pmatrix} 1 & 0 & 0 & 0 & \cdots & 0 & 0 & 0 \\ -1 & 1 & 0 & 0 & \cdots & 0 & 0 & 0 \\ \tilde{p} & -1 & 1 & 0 & \cdots & 0 & 0 & 0 \\ 0 & \tilde{p} & -1 & 1 & \cdots & 0 & 0 & 0 \\ \vdots & \vdots & \ddots & \ddots & \ddots & \vdots & \vdots & \vdots \\ 0 & 0 & 0 & 0 & \cdots & \tilde{p} & -1 & 1 \end{pmatrix}, x := \begin{pmatrix} C_0 \\ C_1 \\ C_2 \\ C_3 \\ \vdots \\ C_k \end{pmatrix}, b := \begin{pmatrix} 0 \\ p^{n_C} \\ \tilde{p} \\ \tilde{p} \\ \vdots \\ \tilde{p} \end{pmatrix} \quad (7.17)$$

To assign the probabilities of a critical crack up to grain  $k$ , we calculate

$$x = A^{-1}b, \quad (7.18)$$

# Microscopic Damage Accumulation Models

## 7. Crack Propagation and Grain Morphology

---

wherefore we compute the inverse of  $A$ . The individual matrix entries of  $A$  follow a regular pattern. Considering

$$\left( \begin{array}{cccccc|cccc} 1 & 0 & 0 & 0 & 0 & \cdots & 0 & 0 & 0 & 1 & 0 & 0 & 0 & 0 & \cdots & 0 & 0 & 0 \\ -1 & 1 & 0 & 0 & 0 & \cdots & 0 & 0 & 0 & 0 & 1 & 0 & 0 & 0 & \cdots & 0 & 0 & 0 \\ \tilde{p} & -1 & 1 & 0 & 0 & \cdots & 0 & 0 & 0 & 0 & 0 & 1 & 0 & 0 & \cdots & 0 & 0 & 0 \\ 0 & \tilde{p} & -1 & 1 & 0 & \cdots & 0 & 0 & 0 & 0 & 0 & 0 & 1 & 0 & \cdots & 0 & 0 & 0 \\ 0 & 0 & \tilde{p} & -1 & 1 & \cdots & 0 & 0 & 0 & 0 & 0 & 0 & 0 & 1 & \cdots & 0 & 0 & 0 \\ \vdots & \vdots & \ddots & \ddots & \ddots & \ddots & \vdots & \vdots & \vdots & \vdots & \vdots & \ddots & \ddots & \ddots & \ddots & \vdots & \vdots & \vdots \\ 0 & 0 & 0 & 0 & 0 & \cdots & \tilde{p} & -1 & 1 & 0 & 0 & 0 & 0 & 0 & \cdots & 0 & 0 & 1 \end{array} \right) \quad (7.19)$$

after proceeding some steps of the Gauß algorithm to invert the matrix, the right handside takes the following form

$$\left( \begin{array}{cccccc|cccc} 1 & 0 & 0 & 0 & 0 & \cdots & 0 & 0 & 0 \\ 1 & 1 & 0 & 0 & 0 & \cdots & 0 & 0 & 0 \\ 1 - \tilde{p} & 1 & 1 & 0 & 0 & \cdots & 0 & 0 & 0 \\ 1 - 2\tilde{p} & 1 - \tilde{p} & 1 & 1 & 0 & \cdots & 0 & 0 & 0 \\ 0 & 0 & 0 & 0 & 1 & \cdots & 0 & 0 & 0 \\ \vdots & \vdots & \ddots & \ddots & \ddots & \ddots & \vdots & \vdots & \vdots \\ 0 & 0 & 0 & 0 & 0 & \cdots & 0 & 0 & 1 \end{array} \right) \quad (7.20)$$

and the inverse further becomes

$$\left( \begin{array}{cccccc|cccc} 1 & 0 & 0 & 0 & 0 & \cdots & 0 & 0 & 0 \\ 1 & 1 & 0 & 0 & 0 & \cdots & 0 & 0 & 0 \\ 1 - \tilde{p} & 1 & 1 & 0 & 0 & \cdots & 0 & 0 & 0 \\ 1 - 2\tilde{p} & 1 - \tilde{p} & 1 & 1 & 0 & \cdots & 0 & 0 & 0 \\ 1 - 2\tilde{p} - \tilde{p}(1 - \tilde{p}) & 1 - 2\tilde{p} & 1 - \tilde{p} & 1 & 1 & \cdots & 0 & 0 & 0 \\ \vdots & \vdots & \ddots & \ddots & \ddots & \ddots & \vdots & \vdots & \vdots \\ 0 & 0 & 0 & 0 & 0 & \cdots & 0 & 0 & 1 \end{array} \right), \quad (7.21)$$

where it is noticeable that the individual matrix entries follow a regular pattern as well, they can be computed using a recurrence relation as well,

$$a_{ij} = a_{i-1j} - \tilde{p} \cdot a_{i-2j}, \quad (7.22)$$

# Microscopic Damage Accumulation Models

## 7. Crack Propagation and Grain Morphology

---

where

$$\begin{aligned}(a_{1j})_{j=1,\dots,n}^t &= \vec{e}_1, \\ (a_{2j})_{j=1,\dots,n}^t &= \vec{e}_1 + \vec{e}_2, \\ a_{ii} &= 1, \quad \text{for } i = 1, \dots, n,\end{aligned}\tag{7.23}$$

such that we can compute the matrix directly to calculate the inverse and therewith avoid a possibly time-consuming procedure for inversion. This again corresponds to a recurrence relation of second order, since it depends on the values of two former solutions. But in controvension to (7.14) it is homogeneous, since the disruptive term on the right handside after rearranging (7.22) equals zero,

$$a_{ij} - a_{i-1j} + \tilde{p} \cdot a_{i-2j} = 0.\tag{7.24}$$

To solve the coefficients of (7.24) we follow a common method, which is shown for example in [16]. Therefore, we first compute the zero crossings of the characteristical polynomial of equation (7.24)

$$P(x) = x^2 - x + \tilde{p}\tag{7.25}$$

and we obtain

$$\begin{aligned}x_0 &= \frac{1 + \sqrt{1 - 4\tilde{p}}}{2}, \\ x_1 &= \frac{1 - \sqrt{1 - 4\tilde{p}}}{2}.\end{aligned}\tag{7.26}$$

The general solution is given by

$$t_n = c_0 \cdot x_0^n + c_1 \cdot x_1^n,\tag{7.27}$$

with some constants  $c_i$ ,  $i = 1, 2$ . We plug in the initial conditions, namely

$$t_0 = 0, \quad t_1 = 1,\tag{7.28}$$

and obtain

$$\begin{aligned}c_0 + c_1 &= 0 \\ c_0 x_0 + c_1 x_1 &= 1.\end{aligned}\tag{7.29}$$

# Microscopic Damage Accumulation Models

## 7. Crack Propagation and Grain Morphology

---

With  $x_0$  and  $x_1$  this leads to the constants

$$\begin{aligned} c_0 &= -c_1 \\ c_1 &= \frac{1}{\sqrt{1-4\tilde{p}}} \end{aligned} \quad (7.30)$$

and therewith the relation

$$\begin{aligned} t_n &= \left( \frac{1}{\sqrt{1-4\tilde{p}}} \right) \cdot \left( \frac{1+\sqrt{1-4\tilde{p}}}{2} \right)^n - \left( \frac{1}{\sqrt{1-4\tilde{p}}} \right) \cdot \left( \frac{1-\sqrt{1-4\tilde{p}}}{2} \right)^n \\ &= \frac{1}{\sqrt{1-4\tilde{p}}} \left[ \left( \frac{1+\sqrt{1-4\tilde{p}}}{2} \right)^n - \left( \frac{1-\sqrt{1-4\tilde{p}}}{2} \right)^n \right]. \end{aligned} \quad (7.31)$$

The inverse matrix  $A^{-1}$  ( $(N - n_C + 2) \times (N - n_C + 2)$ -matrix) therewith can be computed directly and has the following form

$$A^{-1} = \begin{pmatrix} t_1 & t_0 & 0 & 0 & 0 & \cdots & 0 & 0 & 0 \\ t_2 & t_1 & t_0 & 0 & 0 & \cdots & 0 & 0 & 0 \\ t_3 & t_2 & t_1 & t_0 & 0 & \cdots & 0 & 0 & 0 \\ t_4 & t_3 & t_2 & t_1 & t_0 & \cdots & 0 & 0 & 0 \\ t_5 & t_4 & t_3 & t_2 & t_1 & \cdots & 0 & 0 & 0 \\ \vdots & \vdots & \ddots & \ddots & \ddots & \ddots & \vdots & \vdots & \vdots \\ t_{N-n_C+2} & t_{N-n_C+1} & t_{N-n_C} & t_{N-n_C-1} & t_{N-n_C-2} & \cdots & t_3 & t_2 & t_1 \end{pmatrix}. \quad (7.32)$$

Therefore, the cumulated probabilities to observe a  $n_C$  crack in the chain is given by

$$\begin{pmatrix} C_0 \\ C_1 \\ C_2 \\ C_3 \\ C_4 \\ \vdots \\ C_{N-n_C+1} \end{pmatrix} = \begin{pmatrix} t_1 & t_0 & 0 & \cdots & 0 & 0 & 0 \\ t_2 & t_1 & t_0 & \cdots & 0 & 0 & 0 \\ t_3 & t_2 & t_1 & \cdots & 0 & 0 & 0 \\ t_4 & t_3 & t_2 & \cdots & 0 & 0 & 0 \\ t_5 & t_4 & t_3 & \cdots & 0 & 0 & 0 \\ \vdots & \vdots & \ddots & \ddots & \vdots & \vdots & \vdots \\ t_{N-n_C+2} & t_{N-n_C+1} & t_{N-n_C} & \cdots & t_3 & t_2 & t_1 \end{pmatrix} \cdot \begin{pmatrix} 0 \\ p^{n_C} \\ \tilde{p} \\ \tilde{p} \\ \vdots \\ \tilde{p} \end{pmatrix} \quad (7.33)$$

The total crack probability in this model is therewith

$$\begin{aligned} C_N(n_C) &= \mathbb{P}(C_{\min}(n_C, \omega) \leq N - n_C + 1) \\ &= \sum_{k=1}^{N-n_C} t_k \tilde{p} + t_{N-n_C+1} p^{n_C}. \end{aligned} \quad (7.34)$$

## Microscopic Damage Accumulation Models

### 7. Crack Propagation and Grain Morphology

---

To compute the probabilities of failure and the hazard rate we compute the partial derivation with respect to  $p$ . Thus,

$$\begin{aligned}
& \frac{\partial}{\partial p} C_N \\
&= \frac{\partial}{\partial p} \mathbb{P}(C_{\min}(n_C, \omega) \leq N - n_C + 1) \\
&= \frac{\partial}{\partial p} \sum_{k=1}^{N-n_C} t_k \tilde{p} + t_{N-n_C+1} p^{n_C} \\
&= \sum_{k=1}^{N-n_C} \frac{\partial}{\partial p} (t_k \tilde{p} + t_{N-n_C+1} p^{n_C}) \tag{7.35} \\
&= \sum_{k=1}^{N-n_C} \frac{\partial}{\partial p} \left( \frac{\tilde{p}}{\sqrt{1-4\tilde{p}}} \left[ \left( \frac{1+\sqrt{1-4\tilde{p}}}{2} \right)^k - \left( \frac{1-\sqrt{1-4\tilde{p}}}{2} \right)^k \right] \right) \\
&\quad + \frac{\partial}{\partial p} \left( \frac{p^{n_C}}{\sqrt{1-4\tilde{p}}} \left[ \left( \frac{1+\sqrt{1-4\tilde{p}}}{2} \right)^{N-n_C+1} - \left( \frac{1-\sqrt{1-4\tilde{p}}}{2} \right)^{N-n_C+1} \right] \right).
\end{aligned}$$

Let index  $k$  be fixed, we compute for the left part

$$\begin{aligned}
& \frac{\partial}{\partial p} \frac{(1-p)p^{n_C}}{\sqrt{1-4(1-p)p^{n_C}}} \\
&= \frac{n_C p^{n_C-1} - (n_C+1)p^{n_C}}{\sqrt{1-4\tilde{p}}} \left( 1 + \frac{2\tilde{p}}{1-4\tilde{p}} \right) \tag{7.36} \\
&= \frac{(n_C p^{n_C-1} - (n_C+1)p^{n_C})(1-2\tilde{p})}{(1-4\tilde{p})^{\frac{3}{2}}},
\end{aligned}$$

and for the right part

$$\begin{aligned}
& \frac{\partial}{\partial p} \left( \left( \frac{1+\sqrt{1-4\tilde{p}}}{2} \right)^k - \left( \frac{1-\sqrt{1-4\tilde{p}}}{2} \right)^k \right) \\
&= k \frac{(n_C+1)p^{n_C} - n_C p^{n_C-1}}{\sqrt{1-4\tilde{p}}} \left[ \left( \frac{1+\sqrt{1-4\tilde{p}}}{2} \right)^{k-1} + \left( \frac{1-\sqrt{1-4\tilde{p}}}{2} \right)^{k-1} \right]. \tag{7.37}
\end{aligned}$$

Thus, the partial derivation with respect to  $p$  for the sum is given by

## 7. Crack Propagation and Grain Morphology

$$\begin{aligned}
 & \sum_{k=1}^{N-n_C-2} \frac{\partial}{\partial p} t_k \tilde{p} \\
 = & \sum_{k=1}^{N-n_C-2} \frac{\partial}{\partial p} \left( \frac{\tilde{p}}{\sqrt{1-4\tilde{p}}} \left[ \left( \frac{1+\sqrt{1-4\tilde{p}}}{2} \right)^k - \left( \frac{1-\sqrt{1-4\tilde{p}}}{2} \right)^k \right] \right) \\
 = & \sum_{k=1}^{N-n_C-2} \frac{(n_C p^{n_C-1} - (n_C+1)p^{n_C})(1-2\tilde{p})}{(1-4\tilde{p})^{\frac{3}{2}}} \\
 & \cdot \left[ \left( \frac{1+\sqrt{1-4\tilde{p}}}{2} \right)^k - \left( \frac{1-\sqrt{1-4\tilde{p}}}{2} \right)^k \right] \\
 & + \tilde{p} k \frac{(n_C+1)p^{n_C} - n_C p^{n_C-1}}{1-4\tilde{p}} \left[ \left( \frac{1+\sqrt{1-4\tilde{p}}}{2} \right)^{k-1} + \left( \frac{1-\sqrt{1-4\tilde{p}}}{2} \right)^{k-1} \right].
 \end{aligned} \tag{7.38}$$

As it holds that

$$\begin{aligned}
 & \frac{\partial}{\partial p} \frac{p^{n_C}}{\sqrt{1-4\tilde{p}}} \\
 = & \frac{p^{n_C-1} (n_C - 2n_C p^{n_C} + (2n_C - 2)p^{n_C+1})}{(1-\tilde{p})^{\frac{3}{2}}},
 \end{aligned} \tag{7.39}$$

we further compute

$$\begin{aligned}
 & \frac{\partial}{\partial p} t_{N-n_C+1} p^{n_C} \\
 = & \frac{\partial}{\partial p} \left( \frac{p^{n_C}}{\sqrt{1-4\tilde{p}}} \left[ \left( \frac{1+\sqrt{1-4\tilde{p}}}{2} \right)^{N-n_C-2} - \left( \frac{1-\sqrt{1-4\tilde{p}}}{2} \right)^{N-n_C-2} \right] \right) \\
 = & \frac{p^{n_C-1} (n_C - 2n_C p^{n_C} + (2n_C - 2)p^{n_C+1})}{(1-\tilde{p})^{\frac{3}{2}}} \\
 & \cdot \left[ \left( \frac{1+\sqrt{1-4\tilde{p}}}{2} \right)^{N-n_C-1} - \left( \frac{1-\sqrt{1-4\tilde{p}}}{2} \right)^{N-n_C-1} \right] \\
 & + (N-n_C-1) p^{n_C} \frac{(n_C+1)p^{n_C} - n_C p^{n_C-1}}{1-4\tilde{p}} \\
 & \cdot \left[ \left( \frac{1+\sqrt{1-4\tilde{p}}}{2} \right)^{N-n_C-2} + \left( \frac{1-\sqrt{1-4\tilde{p}}}{2} \right)^{N-n_C-2} \right].
 \end{aligned} \tag{7.40}$$

## Microscopic Damage Accumulation Models

### 7. Crack Propagation and Grain Morphology

---

For the partial derivative of the total crack probability we obtain

$$\begin{aligned}
& \frac{\partial}{\partial p} C_N \\
&= \frac{\partial}{\partial p} \mathbb{P}(C_{\min}(n_C, \omega) \leq N - n_C + 1) \\
&= \frac{\partial}{\partial p} \sum_{k=1}^{N-n_C-2} t_k \tilde{p} + t_{N-n_C-1} p^{n_C} \\
&= \sum_{k=1}^{N-n_C-2} \frac{n_C p^{n_C-1} - (n_C + 1) p^{n_C} (1 - 2\tilde{p})}{(1 - 4\tilde{p})^{\frac{3}{2}}} \\
&\quad \cdot \left[ \left( \frac{1 + \sqrt{1 - 4\tilde{p}}}{2} \right)^k - \left( \frac{1 - \sqrt{1 - 4\tilde{p}}}{2} \right)^k \right] \\
&\quad + \tilde{p} k \frac{(n_C + 1) p^{n_C} - n_C p^{n_C-1}}{1 - 4\tilde{p}} \left[ \left( \frac{1 + \sqrt{1 - 4\tilde{p}}}{2} \right)^{k-1} + \left( \frac{1 - \sqrt{1 - 4\tilde{p}}}{2} \right)^{k-1} \right] \\
&\quad + \frac{p^{n_C-1} (n_C - 2n_C p^{n_C} + (2n_C - 2) p^{n_C+1})}{(1 - \tilde{p})^{\frac{3}{2}}} \\
&\quad \cdot \left[ \left( \frac{1 + \sqrt{1 - 4\tilde{p}}}{2} \right)^{N-n_C-1} - \left( \frac{1 - \sqrt{1 - 4\tilde{p}}}{2} \right)^{N-n_C-1} \right] \\
&\quad + (N - n_C - 1) p^{n_C} \frac{(n_C + 1) p^{n_C} - n_C p^{n_C-1}}{1 - 4\tilde{p}} \\
&\quad \cdot \left[ \left( \frac{1 + \sqrt{1 - 4\tilde{p}}}{2} \right)^{N-n_C-2} + \left( \frac{1 - \sqrt{1 - 4\tilde{p}}}{2} \right)^{N-n_C-2} \right].
\end{aligned} \tag{7.41}$$

Having computed the partial derivation of the probability of failure for  $N$  grains in a row, we can use the result to calculate the hazard function

$$h_A(n) = \int_A \rho(n, L_G, \sigma, L_C) dA \tag{7.42}$$

with grain size  $L_G$ , where  $N = \frac{A}{L_G^2}$ , critical crack size  $L_C = n_C \cdot L_G$  and number of cycles  $n$ , which we consider as fixed for the moment. To obtain the hazard for a chain of size  $N$  with the discussed model let

$$\begin{aligned}
p(n) &= F_{SF}(n) \\
&= \mathbb{P} \left( CMB^{-1} \left( RO \left( RO^{-1}(\epsilon_a) \cdot \frac{m(U)}{\lambda} \right) \right) \leq n \right)
\end{aligned} \tag{7.43}$$

# Microscopic Damage Accumulation Models

## 7. Crack Propagation and Grain Morphology

---

denote the single grain crack probability, which is based on the Schmid factor distribution. We use the derivative of the probability of failure and plug in the single crack probability. Thus, we can calculate the density function for a given size  $A$

$$\begin{aligned}
 f_A(n) &= \frac{\partial}{\partial n} F_A(n) \\
 &= \frac{\partial}{\partial n} F_A(L_G, L_C, p(n, \sigma)) \\
 &= \frac{\partial}{\partial p} C_N(L_G, L_C, p(n, \sigma)) \cdot \frac{\partial}{\partial n} p(n, \sigma) \\
 &= \frac{\partial}{\partial p} C_N(L_G, L_C, p(n, \sigma)) \cdot \frac{\partial}{\partial n} \mathbb{P} \left( CMB^{-1} \left( RO \left( RO^{-1}(\epsilon_a) \cdot \frac{m(U)}{\lambda} \right) \right) \leq n \right) \\
 &= \frac{\partial}{\partial p} C_N(L_G, L_C, p(n, \sigma)) \cdot f_{SF}(n)
 \end{aligned} \tag{7.44}$$

with  $\frac{\partial}{\partial p} C_N$  as calculated before. The probability of failure as well as the according density can now be calculated for different numbers of grains, surface size and critical crack sizes  $n_C$ . As we use the Schmid factor distribution, we can include different levels of multiaxiality.

We now look at the distributions for different combinations of grain numbers  $N$  and levels of multiaxiality. The case where  $N = 1$  and  $n_C = 1$  are the same results as for the single grain fatigue life, as shown in figure 6.2. For an increasing number of grains and a constant single grain crack probability the number of possibilities for a crack increases. We can see that the densities as shown in figure 7.7 and 7.12 become more sharp for a growing grain number and a constant critical crack size.

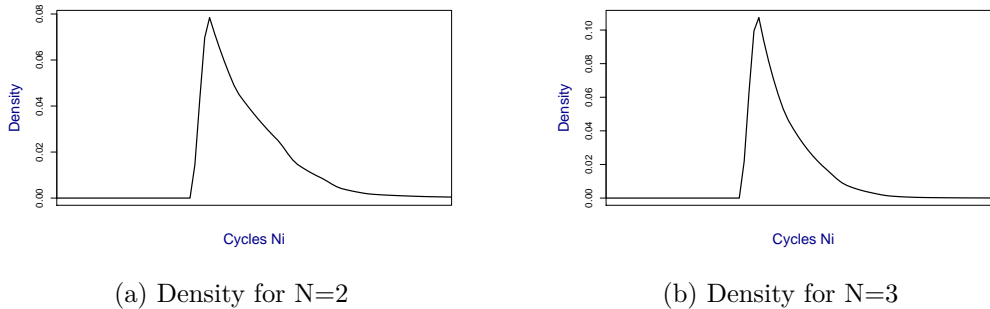


Figure 7.7.: Densities of Lifetime Distribution for 2 and 3 Grains

# Microscopic Damage Accumulation Models

## 7. Crack Propagation and Grain Morphology

---

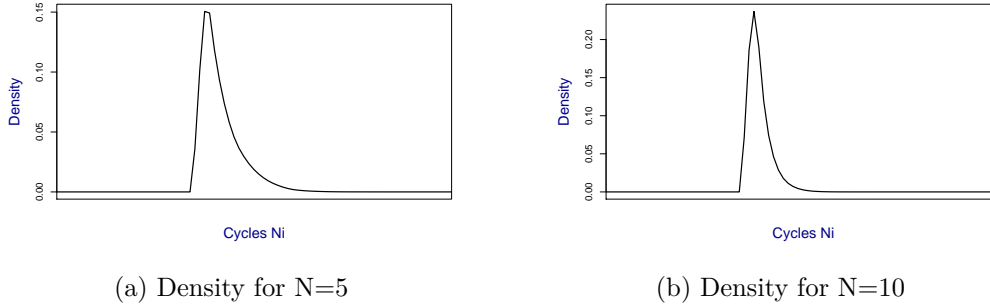


Figure 7.8.: Densities of Lifetime Distribution for 5 and 10 Grains

Looking at the Lifetime Distributions we can see the large differences between even clearer. For  $N = 10$  the distribution increases suddenly up to 1 at a number of about 10.000 cycles. For  $N = 1$  we obtain the known fatigue life distribution of the single grain case. The other distributions for grain numbers  $N = 2, 3, 5$  are in between.

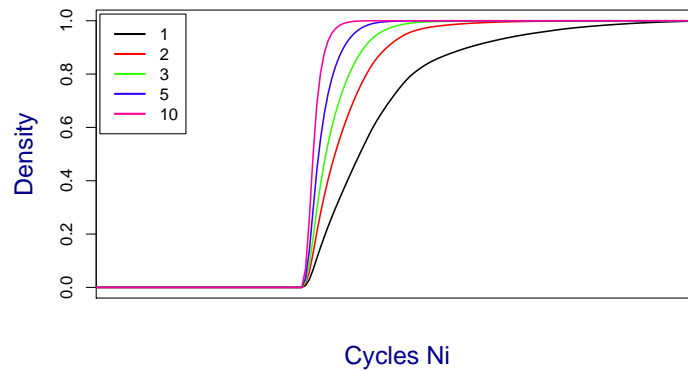


Figure 7.9.: Distributions of Fatigue Life for different Grain Numbers

We look at critical crack lengths  $L_C$  with  $\frac{L_C}{L_G} = n_C > 1$  and see, how the fatigue lifetime changes. We consider a grain chain of size  $N = 10$  and different critical crack sizes with according  $n_C$ .

# Microscopic Damage Accumulation Models

## 7. Crack Propagation and Grain Morphology

---

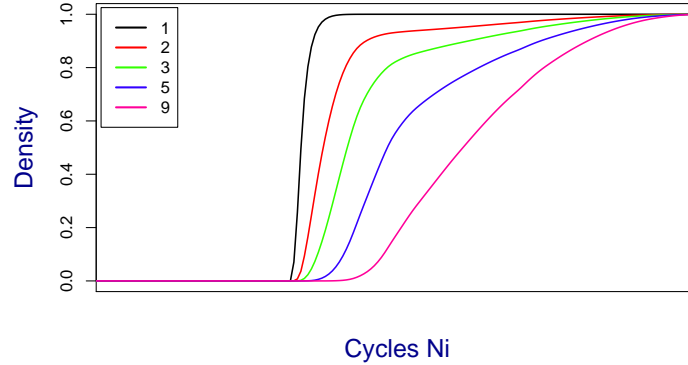


Figure 7.10.: Distributions of Fatigue Life for different Crack Numbers

Figure 7.10 shows the distribution for a fixed grain number of  $N = 10$  and critical grain numbers of 1, 2, 3, 5 and 9. For  $n_C = 1$  we obtain the distribution as given in figure 6.1, represented by the black line. As the number of grains, which need to be cracked in a row to reach a critical crack length, increases, the distribution becomes more and more flat. For a fixed grain number  $N$  the number of possibilities decreases for larger cracks, since more grains need to crack in a row such that the critical crack size is reached. In the following the according densities for the different crack sizes are shown.

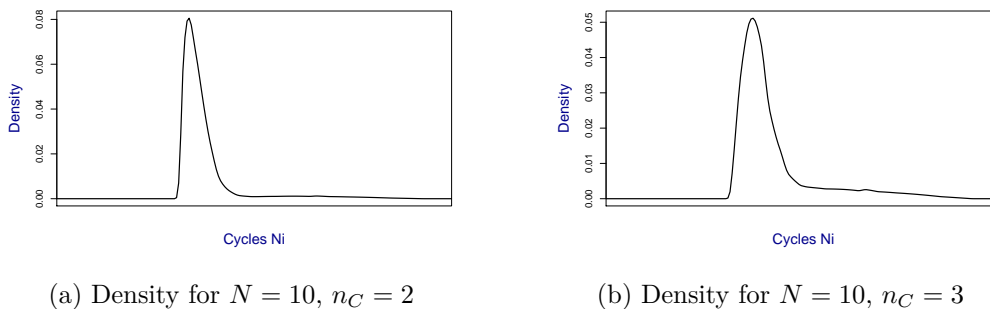


Figure 7.11.: Densities of Lifetime Distribution for  $n_C = 2$  and  $n_C = 3$

# Microscopic Damage Accumulation Models

## 7. Crack Propagation and Grain Morphology

---

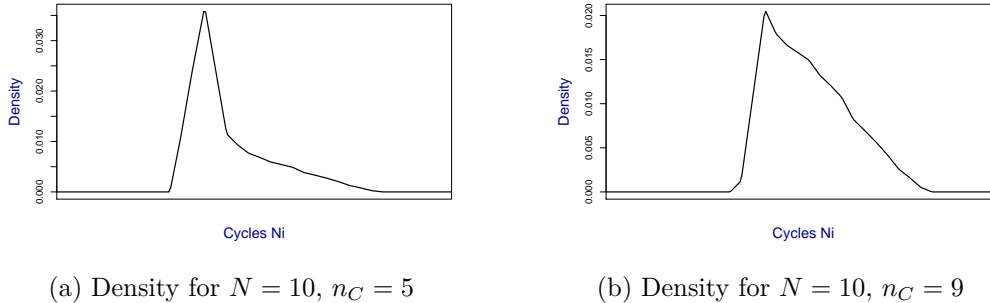


Figure 7.12.: Densities of Lifetime Distribution for  $n_C = 5$  and  $n_C = 9$

For the case of a larger number of grains and a smaller critical crack size the density concentrates and becomes sharp, as the number of possibilities is much higher and once the number of cycles is reached, which leads to a sufficient single crack probability, a small critical crack length is reached very fast. For larger cracks and therewith higher  $n_C$  there is more scatter, as we can see in figure 7.12.

The previous results have been produced using a uniaxial loading state. We now look at the case where  $\kappa = 1$  and compare the densities among each other and to the effects we have seen in the uniaxial case.

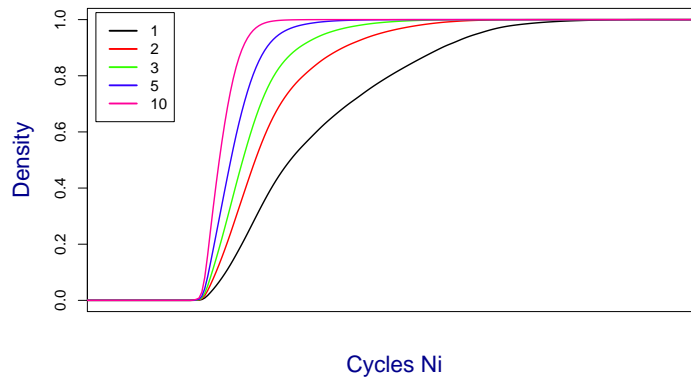


Figure 7.13.: Distributions for  $n_C = 1$  and  $\kappa = 1$

Comparing the distributions as given in figures 7.13 and 7.14 we see that the changes under increasing the number of grains are different to those under uniaxial loading. The minimum values are shifted to the left, so to lower life. They are also wider compared to the uniaxial case.

# Microscopic Damage Accumulation Models

## 7. Crack Propagation and Grain Morphology

---

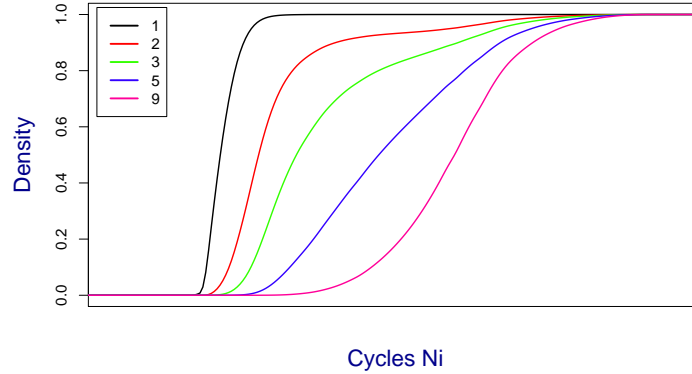


Figure 7.14.: Distributions for  $N = 10$  and  $\kappa = 1$

Considering a fixed number of grains and a larger critical crack size, we see that the distributions deviate even more. As the length of critical crack and therewith  $n_C$  increases, the distributions become flat. In the case where  $n_C = 5$  the course looks nearly linear and for  $n_C = 9$  the distribution increases more steeply at a larger number of cycles.

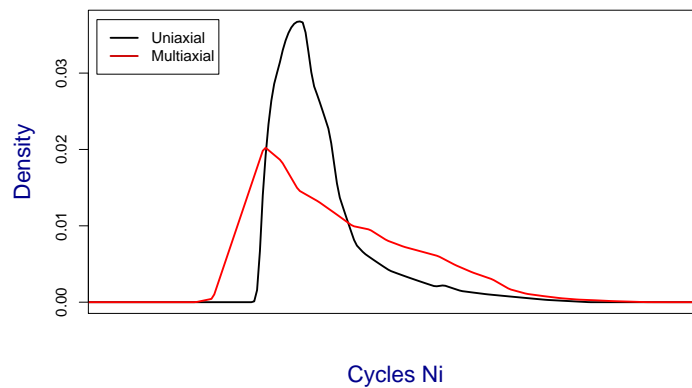


Figure 7.15.: Densities for  $N = 3$ ,  $n_C = 2$  and  $\kappa = 0, 1$

We consider a grain number  $N = 3$  and a number of grains to obtain a critical crack  $n_C = 2$ . It is noticeable that the density in the multiaxial case has a wider range as the uniaxial one. The density of LCF fatigue lifetime starts to increase at approximately 10.000 cycles, whereas the uniaxial one starts increasing at about  $n = 4.500$ , so less than half of the number of cycles.

# Microscopic Damage Accumulation Models

## 7. Crack Propagation and Grain Morphology

---

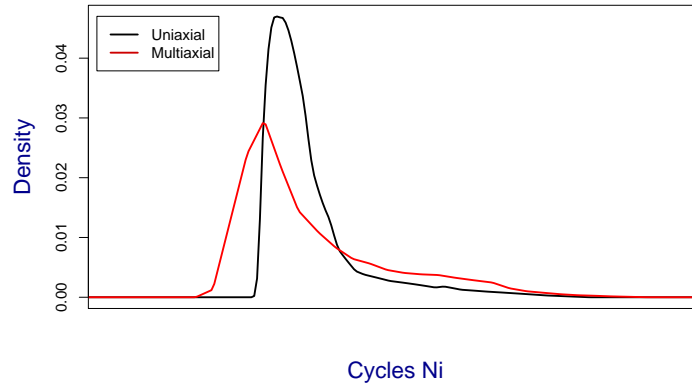


Figure 7.16.: Densities for  $N = 5$ ,  $n_C = 2$  and  $\kappa = 0, 1$

As the number of grains becomes larger and the size of critical crack size remains fixed, the densities become closer, but the one of the multiaxial case is in general shifted to a lower number of cycles and deviates more.

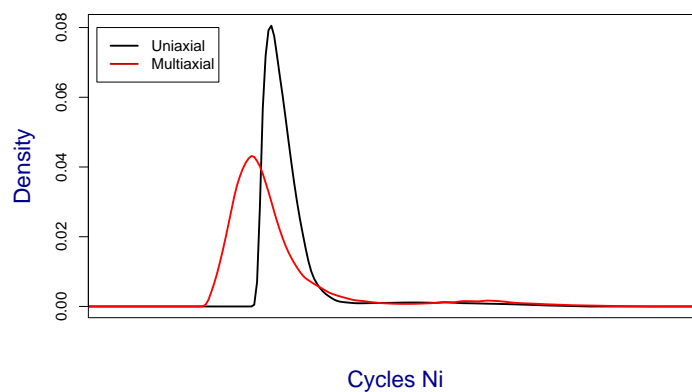


Figure 7.17.: Densities for  $N = 10$ ,  $n_C = 2$  and  $\kappa = 0, 1$

For a fixed number of grains and a larger critical crack size the effects are the same. The larger the critical crack size and therewith  $n_C$  becomes, the more the density scatters.

7. Crack Propagation and Grain Morphology

---

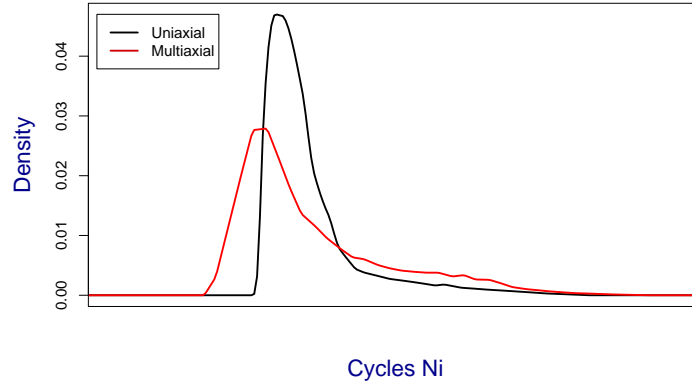


Figure 7.18.: Densities for  $N = 5$ ,  $n_C = 2$  and  $\kappa = 0, 1$

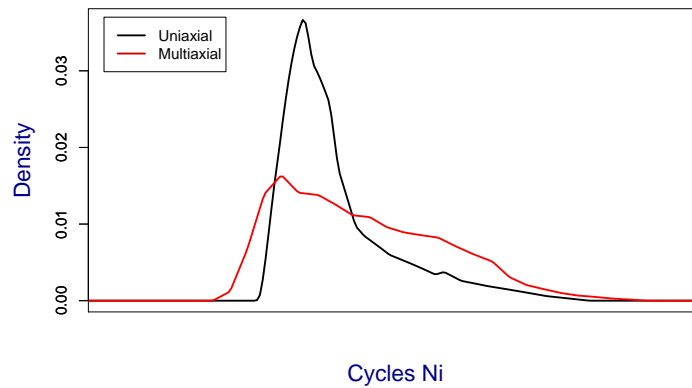


Figure 7.19.: Densities for  $N = 5$ ,  $n_C = 3$  and  $\kappa = 0, 1$

Now we enlarge this to two dimensions and consider a grid of size  $N = N_1 \times N_2$ . We are still focussing on cracks growth in one direction only, which in this case can occur in each of the grain layers. According to (7.5) we again assume independency of the grains, applying equally to the individual grain layers. The  $n_C$ -crack probability of an  $N_2$  chain is

$$F_{N_2}(n_C, p(n, \sigma)) = C_N(n_C, p(n, \sigma)), \quad (7.45)$$

therewith the survival of one layer can be calculated via

$$S_{N_2}(n_C, p(n, \sigma)) = 1 - F_{N_2}(n_C, p(n, \sigma)). \quad (7.46)$$

We transfer this to  $N_2$  independent layers and obtain the survival of all layers

$$S_N(n_C, p(n, \sigma)) = (1 - F_{N_2}(n_C, p(n, \sigma)))^{N_1} \quad (7.47)$$

## 7. Crack Propagation and Grain Morphology

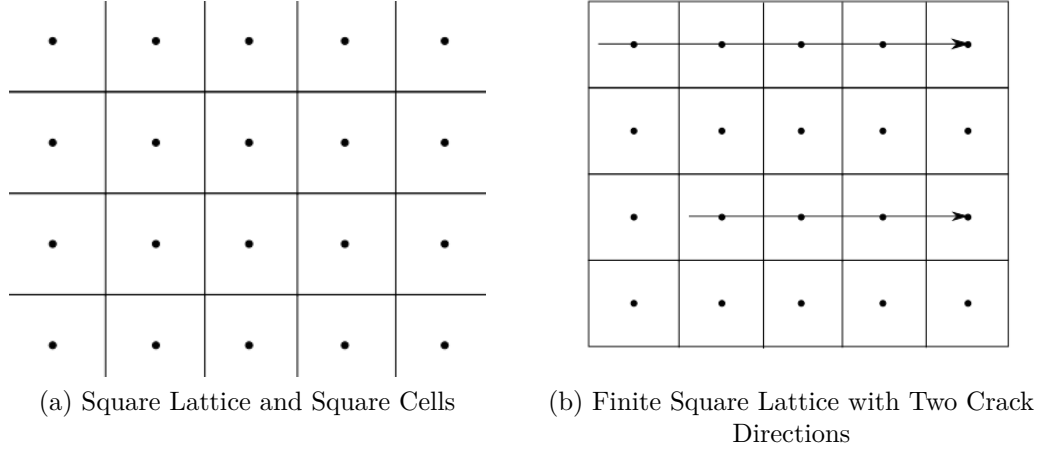


Figure 7.20.: Regular Square Lattice with Two Crack Directions

and therewith the total probability of failure for surface  $A$  divided into  $N$  grains

$$\begin{aligned}
 F_N(n_C, p(n, \sigma)) &= 1 - S_N(n_C, p(n, \sigma)) \\
 &= 1 - (1 - F_{N_2}(n_C, p(n, \sigma)))^{N_1}
 \end{aligned} \tag{7.48}$$

Thus, the partial derivative with respect to lifetime  $n$  of the total crack probability is given by

$$\begin{aligned}
 &\frac{\partial}{\partial n} F_N(n_C, p(n, \sigma)) \\
 &= \frac{\partial}{\partial n} (1 - S_N(n_C, p(n, \sigma))) \\
 &= \frac{\partial}{\partial n} \left( 1 - (1 - F_{N_2}(n_C, p(n, \sigma)))^{N_1} \right) \\
 &= N_1 (1 - F_{N_2}(n_C, p(n, \sigma)))^{N_1-1} \cdot \left( \frac{\partial}{\partial n} F_{N_2}(n_C, p(n, \sigma)) \right) \\
 &= N_1 (1 - F_{N_2}(n_C, p(n, \sigma)))^{N_1-1} \cdot \left( \frac{\partial}{\partial p} C_N(n_C, p(n, \sigma)) \cdot \frac{\partial}{\partial n} p(n, \sigma) \right) \\
 &= N_1 (1 - F_{N_2}(n_C, p(n, \sigma)))^{N_1-1} \cdot \left( \frac{\partial}{\partial p} C_N(n_C, p(n, \sigma)) \cdot f_{SF}(n) \right),
 \end{aligned} \tag{7.49}$$

where  $\frac{\partial}{\partial p} C_{N_2}$  is the result of 7.41. We consider a critical crack size with  $n_C = 2$  and  $N_2 = 5$ . A comparison of the corresponding densities is given in figure 7.21 and 7.21. As expected the density becomes more sharp for multiple layers, since the total crack probability increases strongly for growing  $N_1$ .

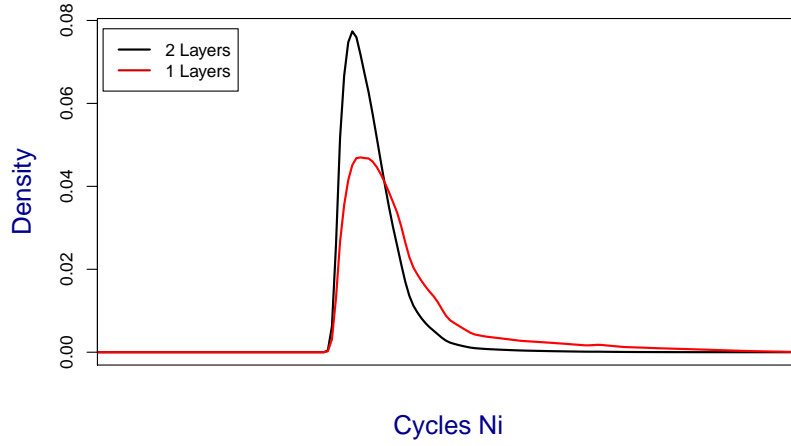


Figure 7.21.: Densities for  $N_1 = 1, 2$ ,  $N_2 = 5$   $n_C = 2$

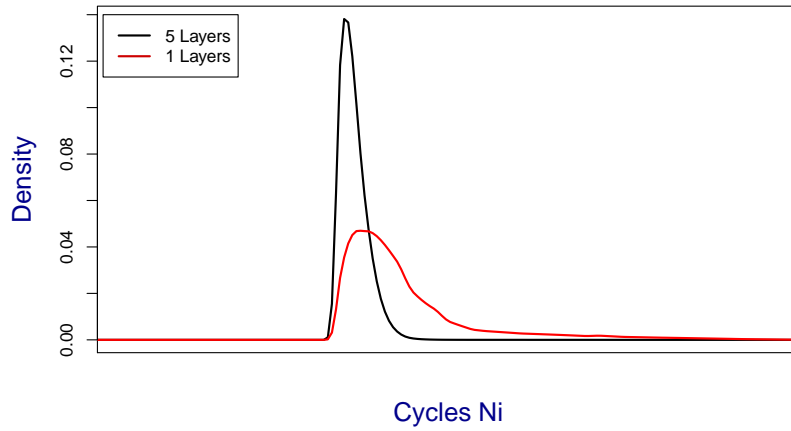


Figure 7.22.: Densities for  $N_1 = 1, 5$ ,  $N_2 = 5$   $n_C = 2$

Once a threshold value for a number of cycles and therewith a single crack probability is reached, the density increases. As

$$F_{N_2}(n_C, p(n, \sigma)) \xrightarrow{n \rightarrow \infty} 1 \quad (7.50)$$

and therewith

$$1 - F_{N_2}(n_C, p(n, \sigma)) \xrightarrow{n \rightarrow \infty} 0, \quad (7.51)$$

the density of the total crack probability converges to 0 for  $N_1 \rightarrow \infty$ , if  $p(n, \sigma) > 0$ . Since we have investigated the lifetime calculations for crack within a given rect-

## 7. Crack Propagation and Grain Morphology

---

angular surface and given edges, the following chapter considers surfaces in form of a rod and introduces an extension of the model by cracks occurring at the whole surface, where both edges are connected.

### 7.2. Approach for Circuit Structures

The introduced percolation model, which fulfills a recurrence relation, illustrates a simple case of a grain structure and the type of crack possibly occurring with regards to the single grain crack probability  $p$  and definition of a critical crack condition.

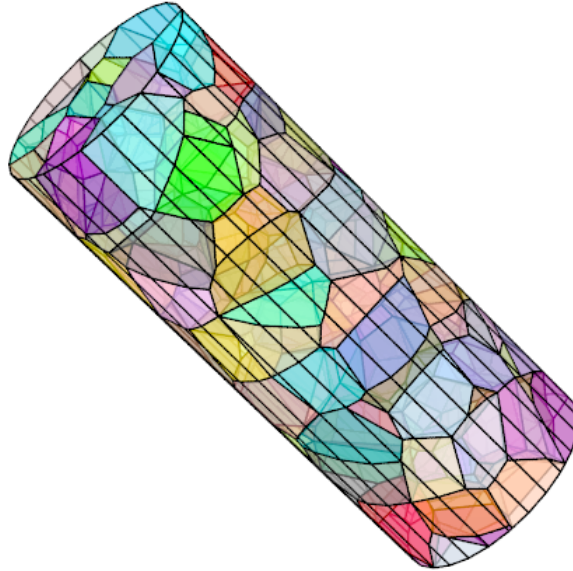


Figure 7.23.: Visualization of the Geometry of the Measuring Section, see [8]

We considered an arbitrary long chain neglecting boundary effects. The geometry of the measuring section of the specimen is cylindrical. An example of this section is given in figure 7.23. Thus, cracks can occur within the whole circumference. We introduce an approach, which considers the geometry of the specimen. Let us assume that both ends are merging into one another, such that there exists an edge  $(v_N, v_1) \in E'$  as given in (7.1). Besides the starting point of an  $s$ -cluster of the non-connected chain, i.e. for  $k = 1, \dots, N - s + 1$ ,

$$C(s, \omega) := \{j | j \in \{1, \dots, N - s + 1\} : X_j(\omega) = 1, \dots, X_{j+s-1}(\omega) = 1\}, \quad (7.52)$$

# Microscopic Damage Accumulation Models

## 7. Crack Propagation and Grain Morphology

---

and the first observed  $n_C$ -cluster again defined by

$$C_{\min}(s, \omega) := \min C(s, \omega). \quad (7.53)$$

we enable the critical crack to begin in a grain  $k \in \{N - n_C + 2, \dots, N\}$  and proceed at the beginning of the chain with  $k \in \{1, \dots, n_C - 1\}$ . Therefore we set for  $k \in \{2, \dots, N - n_C + 1\}$

$$\begin{aligned} M_k(n_C) &:= \{\omega : C_{\min}(n_C, \omega) = k\} \\ &= \{\min k | \omega : X_{k-1}(\omega) = 0, X_k(\omega) = 1, \dots, X_{k+n_C-1}(\omega) = 1\} \end{aligned} \quad (7.54)$$

and

$$M_1(n_C) := \{\omega : X_1(\omega) = 1, \dots, X_{n_C}(\omega) = 1\}. \quad (7.55)$$

Therefore, the last possible critical crack in the chain, which does not overlap the edges, is given by

$$M_{N-n_C+1}(n_C) = \{\omega : C_{\min}(n_C, \omega) = N - n_C + 1\}. \quad (7.56)$$

Let the crack size  $n_C$  be divided, such that

$$n_C = n_C^1 + n_C^2. \quad (7.57)$$

The case that a crack overlaps, such that there is a  $n_C^1$ -crack starting in grain  $k = N - n_C^1 + 1$  and continuing from  $k = 1$  up to at least  $k = n_C^2$  can be illustrated by

$$E_1(n_C^1) := \{\omega : X_{N-n_C^1}(\omega) = 0, X_{N-n_C^1+1}(\omega) = 1, \dots, X_N(\omega) = 1\} \quad (7.58)$$

and

$$E_2(n_C^2) := \{\omega : X_1(\omega) = 1, \dots, X_{n_C^2}(\omega) = 1\}. \quad (7.59)$$

To obtain the probability for a  $n_C$ -crack overlapping on the boundary cells we connect the former given events, namely that there is no  $n_C$ -crack starting until the boundary is reached as well as the case that a  $n_C^1$ -crack begins in grain  $k = N - n_C^1 + 1, \dots, N$  and continues up to  $k = 1, \dots, n_C^2$ .

For  $k \in \{N - n_C + 2, \dots, N\}$  let  $E_1 = E_1(N - k + 1)$  and  $E_2 = E_2(k + n_C - N - 1)$  and compute the  $n_C$ -crack probability for an overlapping crack starting in  $k$  as follows

$$\mathbb{P}(C_{\min}(n_C, \omega) = k) = \mathbb{P}\left(\left(E_1 \cap E_2\right) \setminus \left(\bigcup_{l=1}^{N-n_C+1} M_l\right)\right) \quad (7.60)$$

# Microscopic Damage Accumulation Models

## 7. Crack Propagation and Grain Morphology

---

and can be rearranged the following

$$\begin{aligned}
& \mathbb{P} \left( (E_1 \cap E_2) \setminus \left( \bigcup_{l=1}^{N-n_C+1} M_l \right) \right) \\
&= \mathbb{P} \left( E_1 \cap E_2 \cap \left( \bigcap_{l=1}^{N-n_C+1} M_l^C \right) \right) \\
&= \mathbb{P}(E_2) \cdot \mathbb{P} \left( \bigcap_{l=1}^{N-n_C+1} M_l^C \middle| E_2 \right) \cdot \mathbb{P} \left( E_1 \middle| E_2 \cap \left( \bigcap_{l=1}^{N-n_C+1} M_l^C \right) \right) \\
&= \mathbb{P} \left( E_2 \cap \left( \bigcap_{l=1}^{N-n_C+1} M_l^C \right) \right) \cdot \mathbb{P} \left( E_1 \middle| E_2 \cap \left( \bigcap_{l=1}^{N-n_C+1} M_l^C \right) \right) \tag{7.61} \\
&= \mathbb{P} \left( E_2 \setminus \left( \bigcup_{l=1}^{N-n_C+1} M_l \right) \right) \cdot \mathbb{P} \left( E_1 \middle| E_2 \cap \left( \bigcap_{l=1}^{N-n_C+1} M_l^C \right) \right) \\
&= \left( \mathbb{P}(E_2) - \mathbb{P} \left( E_2 \cap \left( \bigcup_{l=1}^{N-n_C+1} M_l \right) \right) \right) \cdot \mathbb{P} \left( E_1 \middle| E_2 \cap \left( \bigcap_{l=1}^{N-n_C+1} M_l^C \right) \right) \\
&= (\mathbb{P}(E_2) - \mathbb{P}(E_2 \cap M_1) - \mathbb{P}(E_2 \cap M_2) - \dots - \mathbb{P}(E_2 \cap M_{N-n_C+1})) \\
&\quad \cdot \mathbb{P} \left( E_1 \middle| E_2 \cap \left( \bigcap_{l=1}^{N-n_C+1} M_l^C \right) \right),
\end{aligned}$$

where the last equation holds, because the sets  $M_k$  are pairwise disjoint.

Therewith, only the cases are considered, which show a crack in  $k = N - n_C^1 + 1$  up to  $k = n_C^2$ . As we look at the minimal or most left grain where this occurs, it is reduced by the cases of  $n_C$ -crack occurrences (in form of events  $M_k$ ) before the edge is reached according to the calculations for the  $n_C$ -crack probabilities without the edges. This can as well be visualised by a tree structure, where each level stands for a specific grain number.

As the sets  $M_l$  describe the case that the minimal starting point is in  $l$  we can calculate for the case that a  $n_C^2$ -crack starts in the first grain, but does not contain a  $n_C$ -crack (otherwise this would have been the first observed  $n_C$ -crack already), as follows

$$\mathbb{P}(E_2) - \mathbb{P}(E_2 \cap M_1) = p^{n_C^2} - p^{n_C}. \tag{7.62}$$

We see that for the second case it holds that

$$\mathbb{P}(E_2 \cap M_2) = 0, \tag{7.63}$$

## Microscopic Damage Accumulation Models

### 7. Crack Propagation and Grain Morphology

---

as the case  $X_1 = 0$  is not included in  $E_2$ , which is also true for  $M_3, \dots, M_{n_C^2+1}$ , thus

$$\mathbb{P}(E_2) - \mathbb{P}(E_2 \cap M_1) - \dots - \mathbb{P}(E_2 \cap M_{n_C^2+1}) = p^{n_C^2} - p^{n_C}. \quad (7.64)$$

Now let

$$D_l(n_C) := \mathbb{P}(E_2 \cap M_1) + \dots + \mathbb{P}(E_2 \cap M_l) \quad (7.65)$$

for  $l \in \{1, \dots, N - n_C + 1\}$  with  $E_1$  and  $E_2$  as given in (7.58) and (7.59). Therewith,

$$D_1(n_C) = p^{n_C}, \quad (7.66)$$

$$D_l(n_C) = 0 + p^{n_C} \quad (7.67)$$

for grains  $l = 2, \dots, n_C^2 + 1$  and

$$D_{n_C^2+2}(n_C) = p^{n_C^2}(1 - p)p^{n_C}. \quad (7.68)$$

For grains  $l \in \{n_C^2 + 3, \dots, N - n_C - n_C^1\}$  the probability can again be represented via a recurrence relation

$$D_l(n_C) = (p^{n_C^2} - D_{l-2}) (1 - p)p^{n_C} + D_{l-1}, \quad (7.69)$$

as the minimal  $n_C$ -crack starting point follows the same principle as in (7.10) and the cumulated crack possibilities can be formulated recursively as well.

Considering again the whole expression

$$\mathbb{P} \left( (E_1 \cap E_2) \setminus \left( \bigcup_{l=1}^{N-n_C+1} M_l \right) \right), \quad (7.70)$$

we see that the probability of all events can be calculated according to those of  $E_2$  and the junction of  $M_k$ , since we can equivalently write

$$\begin{aligned} & \mathbb{P} \left( (E_1 \cap E_2) \setminus \left( \bigcup_{l=1}^{N-n_C+1} M_l \right) \right) \\ &= \mathbb{P}(E_2 \cap E_1) - \mathbb{P}(E_2 \cap E_1 \cap M_1) - \mathbb{P}(E_2 \cap E_1 \cap M_2) \dots \\ & \dots - \mathbb{P}(E_2 \cap E_1 \cap M_{N-n_C+1}) \end{aligned} \quad (7.71)$$

Since

$$E_1(n_C^1, \omega) := \{X_{N-n_C^1}(\omega) = 0, X_{N-n_C^1+1}(\omega) = 1, \dots, X_N(\omega) = 1\}, \quad (7.72)$$

# Microscopic Damage Accumulation Models

## 7. Crack Propagation and Grain Morphology

---

it follows that

$$\mathbb{P}(E_2 \cap E_1 \cap M_l) = 0 \quad (7.73)$$

for  $l = N - n_C - n_C^1 + 1, \dots, N - n_C + 1$ , as the case that  $X_{N-n_C^1}(\omega) = 0$  is not included in  $M_{N-n_C-n_C^1+1}, \dots, M_{N-n_C+1}$ . Equation (7.61) reduces the following

$$\begin{aligned} & \mathbb{P} \left( (E_1 \cap E_2) \setminus \left( \bigcup_{l=1}^{N-n_C+1} M_l \right) \right) \\ &= \mathbb{P}(E_2 \cap E_1) - \mathbb{P}(E_2 \cap E_1 \cap M_1) - \mathbb{P}(E_2 \cap E_1 \cap M_2) \cdots \\ & \quad \cdots - \mathbb{P}(E_2 \cap E_1 \cap M_{N-n_C+1}) \\ &= \mathbb{P}(E_2 \cap E_1) - \mathbb{P}(E_2 \cap E_1 \cap M_1) - \mathbb{P}(E_2 \cap E_1 \cap M_2) \cdots \\ & \quad \cdots - \mathbb{P}(E_2 \cap E_1 \cap M_{N-n_C-n_C^1}), \end{aligned} \quad (7.74)$$

For the remaining events it is easy to see that  $E_1$  is independent of them, therefore it follows that

$$\begin{aligned} & \mathbb{P} \left( (E_1 \cap E_2) \setminus \left( \bigcup_{l=1}^{N-n_C+1} M_l \right) \right) \\ &= \mathbb{P}(E_2 \cap E_1) - \mathbb{P}(E_2 \cap E_1 \cap M_1) - \mathbb{P}(E_2 \cap E_1 \cap M_2) \cdots \\ & \quad \cdots - \mathbb{P}(E_2 \cap E_1 \cap M_{N-n_C-n_C^1}) \\ &= (\mathbb{P}(E_2) - \mathbb{P}(E_2 \cap M_1) - \mathbb{P}(E_2 \cap M_2) \cdots \\ & \quad \cdots - \mathbb{P}(E_2 \cap M_{N-n_C-n_C^1})) \cdot (1-p)p^{n_C^2} \end{aligned} \quad (7.75)$$

Combining the calculations, we obtain for  $k = N - n_C + 2, \dots, N$  that

$$\begin{aligned} \mathbb{P}(C_{\min}(n_C, \omega) = k) &= \mathbb{P} \left( (E_1 \cap E_2) \setminus \left( \bigcup_{l=1}^{N-n_C+1} M_l \right) \right) \\ &= (\mathbb{P}(E_2) - \mathbb{P}(E_2 \cap M_1) - \mathbb{P}(E_2 \cap M_2) \cdots \\ & \quad \cdots - \mathbb{P}(E_2 \cap M_{N-n_C-n_C^1})) \cdot (1-p)p^{n_C^2} \\ &= (p^{n_C^2} - D_{N-n_C-n_C^1}) (1-p)p^{n_C^1}, \end{aligned} \quad (7.76)$$

where

$$D_l = \begin{cases} p^{n_C}, & l = 1, \dots, n_C^2 + 1 \\ p^{n_C^2} (1-p)p^{n_C} + p^{n_C}, & l = n_C^2 + 2 \\ (p^{n_C^2} - D_{l-2}) (1-p)p^{n_C^1} + D_{l-1}, & l = n_C^2 + 3, \dots, N - n_C - n_C^1. \end{cases} \quad (7.77)$$

# Microscopic Damage Accumulation Models

## 7. Crack Propagation and Grain Morphology

---

Therewith, we can subdivide the probability of an inner  $n_C$ -crack up to grain  $k = N - n_C + 1$  and those of an overlapping  $n_C$ -crack. We see that

$$\mathbb{P}(C_{\min}(n_C, \omega) \leq k) = C_{N-n_C+1} + \sum_{n_C^1=n_C-1}^{N-k+1} \left( p^{n_C^2} - D_{N-n_C-n_C^1} \right) (1-p)p^{n_C^1}, \quad (7.78)$$

for  $k = N - n_C + 2, \dots, N$  and  $n_C^2 = n_C - n_C^1$ .

The probability for a  $n_C$ -crack occurrence up to grain  $N - n_C + 2$  can be calculated as follows

$$\begin{aligned} C_{N-n_C+2}(n_C) &= \mathbb{P}(C_{\min}(n_C, \omega) = N - n_C + 2) + C_{N-n_C+1} \\ &= \left( p^{n_C^2} - D_{N-n_C-n_C^1} \right) (1-p)p^{n_C^1} + C_{N-n_C+1} \\ &= \left( p - D_{N-n_C-(n_C-1)} \right) (1-p)p^{n_C-1} + C_{N-n_C+1}. \end{aligned} \quad (7.79)$$

To obtain the total  $n_C$ -crack probability up to grain  $N$ , i.e. the probability that at least one  $n_C$ -crack occurs in the chain, we compute

$$\begin{aligned} C_N(n_C) &= \mathbb{P}(C_{\min}(n_C, \omega) \leq N) \\ &= \mathbb{P}(C_{\min}(n_C, \omega) \leq N - n_C + 1) \\ &\quad + \sum_{n_C^1=n_C-1}^1 \left( p^{n_C^2} - D_{N-n_C-n_C^1} \right) (1-p)p^{n_C^1} \end{aligned} \quad (7.80)$$

The following we solve the last term, in particular we calculate  $D_l$  to obtain a solution for the cumulated crack probabilities depending on  $n_C$  and  $N$ , which we use to compute the total  $n_C$ -crack probability for a chain of length  $N$ . Afterwards the results are transferred to two-dimensional grain structures.

Analogously to (7.14)  $D_l$  can be represented as an inhomogeneous recurrence equation of second order. To remind,  $\tilde{p} := (1-p)p^{n_C}$ , we rearrange  $D_l$  the following

$$D_l - D_{l-1} + D_{l-2}(1-p)p^{n_C} = (1-p)p^{n_C} = \tilde{p}. \quad (7.81)$$

With

$$(1-p)p^{n_C} = \frac{\tilde{p}}{p^{n_C}} := p^* \quad (7.82)$$

we again set up the equations

$$Ax = b, \quad (7.83)$$

# Microscopic Damage Accumulation Models

## 7. Crack Propagation and Grain Morphology

---

where

$$A := \begin{pmatrix} 1 & 0 & 0 & 0 & \cdots & 0 & 0 & 0 & 0 & 0 & \cdots & 0 & 0 & 0 & 0 \\ 0 & 1 & 0 & 0 & \cdots & 0 & 0 & 0 & 0 & 0 & \cdots & 0 & 0 & 0 & 0 \\ 0 & 0 & 1 & 0 & \cdots & 0 & 0 & 0 & 0 & 0 & \cdots & 0 & 0 & 0 & 0 \\ \vdots & \vdots & \ddots & \ddots & \ddots & \ddots & \vdots \\ 0 & 0 & 0 & 0 & \cdots & 1 & 0 & 0 & 0 & 0 & \cdots & 0 & 0 & 0 & 0 \\ 0 & 0 & 0 & 0 & \cdots & -1 & 1 & 0 & 0 & 0 & \cdots & 0 & 0 & 0 & 0 \\ 0 & 0 & 0 & 0 & \cdots & p^* & -1 & 1 & 0 & 0 & \cdots & 0 & 0 & 0 & 0 \\ 0 & 0 & 0 & 0 & \cdots & 0 & p^* & -1 & 1 & 0 \cdots & 0 & 0 & 0 & 0 & 0 \\ \vdots & \vdots & \ddots & \ddots & \ddots & \ddots & \vdots \\ 0 & 0 & 0 & 0 & \cdots & 0 & 0 & 0 & 0 & 0 & \cdots & 0 & p^* & -1 & 1 \end{pmatrix}, \quad (7.84)$$

$$x := \begin{pmatrix} D_0 \\ D_1 \\ D_2 \\ D_3 \\ \vdots \\ D_{n_C^2+1} \\ D_{n_C^2+2} \\ D_{n_C^2+3} \\ D_{n_C^2+4} \\ \vdots \\ D_{N-n_C-n_C^1} \end{pmatrix}, b := \begin{pmatrix} 0 \\ p^{n_C} \\ p^{n_C} \\ p^{n_C} \\ \vdots \\ p^{n_C} \\ p^{n_C^2} \tilde{p} \\ \tilde{p} \\ \tilde{p} \\ \vdots \\ \tilde{p} \end{pmatrix} \quad (7.85)$$

To assign the probabilities of a critical crack up to grain  $N - n_C - n_C^1$ , which is overlapping the edges, we again calculate

$$x = A^{-1}b, \quad (7.86)$$

# Microscopic Damage Accumulation Models

## 7. Crack Propagation and Grain Morphology

---

and see that the entries of the inverse of  $A$  follow a regular pattern as well. According to the calculations before we easily obtain

$$A^{-1} := \begin{pmatrix} 1 & 0 & 0 & 0 & \cdots & 0 & 0 & 0 & 0 & 0 & \cdots & 0 & 0 & 0 & 0 \\ 0 & 1 & 0 & 0 & \cdots & 0 & 0 & 0 & 0 & 0 & \cdots & 0 & 0 & 0 & 0 \\ 0 & 0 & 1 & 0 & \cdots & 0 & 0 & 0 & 0 & 0 & \cdots & 0 & 0 & 0 & 0 \\ \vdots & \vdots & \ddots & \ddots & \ddots & \ddots & \vdots \\ 0 & 0 & 0 & 0 & \cdots & 1 & 0 & 0 & 0 & 0 & \cdots & 0 & 0 & 0 & 0 \\ 0 & 0 & 0 & 0 & \cdots & 1 & 1 & 0 & 0 & 0 & \cdots & 0 & 0 & 0 & 0 \\ 0 & 0 & 0 & 0 & \cdots & 1 - p^* & 1 & 1 & 0 & 0 & \cdots & 0 & 0 & 0 & 0 \\ 0 & 0 & 0 & 0 & \cdots & 1 - 2p^* & 1 - p^* & 1 & 1 & 0 & \cdots & 0 & 0 & 0 & 0 \\ \vdots & \vdots \end{pmatrix}, \quad (7.87)$$

for whose entries we can set up the recurrence relation

$$a_{ij} = a_{i-1j} - p^* \cdot a_{i-2j} \quad (7.89)$$

and conditions

$$\begin{aligned} (a_{ij})_{j=1, \dots, n}^t &= \vec{e}_i, & \text{for } i = 1, \dots, n_C^2 + 1, \\ (a_{ij})_{j=1, \dots, n}^t &= \vec{e}_{i-1} + \vec{e}_i, & \text{for } i = n_C^2 + 2, \\ a_{ii} &= 1, & \text{for } i = n_C^2 + 3, \dots, N - n_C - n_C^1. \end{aligned} \quad (7.90)$$

This recurrence relation of second order is again homogeneous and the coefficients solve

$$a_{ij} - a_{i-1j} + p^* \cdot a_{i-2j} = 0 \quad (7.91)$$

can be obtained by calculating the zero crossings of

$$P(x) = x^2 - x + p^*, \quad (7.92)$$

which are given by

$$\begin{aligned} x_0 &= \frac{1 + \sqrt{1 - 4p^*}}{2}, \\ x_1 &= \frac{1 - \sqrt{1 - 4p^*}}{2}. \end{aligned} \quad (7.93)$$

# Microscopic Damage Accumulation Models

## 7. Crack Propagation and Grain Morphology

---

Plugging in the initial conditions in the general solution as given before in (7.27), namely

$$t_0 = 0, \quad t_1 = 1, \quad (7.94)$$

we obtain

$$\begin{aligned} c_0 + c_1 &= 0 \\ c_0 x_0 + c_1 x_1 &= 1. \end{aligned} \quad (7.95)$$

With the constants

$$\begin{aligned} c_0 &= -c_1 \\ c_1 &= \frac{1}{\sqrt{1-4\bar{p}}}, \end{aligned} \quad (7.96)$$

which results in the relation

$$\begin{aligned} t_n &= \left( \frac{1}{\sqrt{1-4\bar{p}^*}} \right) \cdot \left( \frac{1 + \sqrt{1-4\bar{p}^*}}{2} \right)^n - \left( \frac{1}{\sqrt{1-4\bar{p}^*}} \right) \cdot \left( \frac{1 - \sqrt{1-4\bar{p}^*}}{2} \right)^n \\ &= \frac{1}{\sqrt{1-4\bar{p}^*}} \left[ \left( \frac{1 + \sqrt{1-4\bar{p}^*}}{2} \right)^n - \left( \frac{1 - \sqrt{1-4\bar{p}^*}}{2} \right)^n \right]. \end{aligned} \quad (7.97)$$

This leads to the  $(N - n_C - n_C^1 + 1) \times (N - n_C - n_C^1 + 1)$ -matrix

$$A^{-1} := \begin{pmatrix} t_1 & t_0 & 0 & 0 & \cdots & 0 & 0 & 0 & \cdots & 0 & 0 \\ 0 & t_1 & t_0 & 0 & \cdots & 0 & 0 & 0 & \cdots & 0 & 0 \\ 0 & 0 & t_1 & t_0 & \cdots & 0 & 0 & 0 & \cdots & 0 & 0 \\ \vdots & \vdots & \ddots & \ddots & \vdots \\ 0 & 0 & 0 & 0 & \cdots & t_1 & t_0 & 0 & \cdots & 0 & 0 \\ 0 & 0 & 0 & 0 & \cdots & t_1 & t_1 & t_0 & \cdots & 0 & 0 \\ 0 & 0 & 0 & 0 & \cdots & t_2 & t_1 & t_1 & \cdots & 0 & 0 \\ 0 & 0 & 0 & 0 & \cdots & t_3 & t_2 & t_1 & \cdots & 0 & 0 \\ \vdots & \vdots \\ 0 & 0 & 0 & 0 & \cdots & t_{N-2n_C-1} & t_{N-2n_C-2} & t_{N-2n_C-3} & \cdots & t_1 & t_1 \end{pmatrix}, \quad (7.98)$$

## Microscopic Damage Accumulation Models

### 7. Crack Propagation and Grain Morphology

---

Therefore, the results for  $D_l$ ,  $l \in 1, \dots, N - n_C + 1$  can be calculated via

$$\begin{pmatrix} D_0 \\ D_1 \\ \vdots \\ D_{n_C^2+1} \\ D_{n_C^2+2} \\ D_{n_C^2+3} \\ \vdots \\ D_{N-n_C-n_C^1} \end{pmatrix} = \begin{pmatrix} t_1 & t_0 & \cdots & 0 & 0 & 0 & \cdots & 0 \\ 0 & t_1 & \cdots & 0 & 0 & 0 & \cdots & 0 \\ 0 & 0 & \cdots & 0 & 0 & 0 & \cdots & 0 \\ \vdots & \vdots & \ddots & \vdots & \vdots & \vdots & \ddots & \vdots \\ 0 & 0 & \cdots & t_1 & t_0 & 0 & \cdots & 0 \\ 0 & 0 & \cdots & t_1 & t_1 & t_0 & \cdots & 0 \\ 0 & 0 & \cdots & t_2 & t_1 & t_1 & \cdots & 0 \\ \vdots & \vdots & \ddots & \ddots & \ddots & \ddots & \ddots & \vdots \\ 0 & 0 & \cdots & t_{N-2n_C-1} & t_{N-2n_C-2} & t_{N-2n_C-3} & \cdots & t_1 \end{pmatrix} \cdot \begin{pmatrix} 0 \\ p^{n_C} \\ \vdots \\ p^{n_C} \\ p^{n_C^2} \tilde{p} \\ \tilde{p} \\ \vdots \\ \tilde{p} \end{pmatrix} \quad (7.99)$$

So we obtain  $D_{N-n_C-n_C^1}$  depending on  $n_C$  and  $n_C^1$  as follows

$$\begin{aligned} D_{N-n_C-n_C^1} &= t_{N-2n_C-1} \cdot p^{n_C^2} \tilde{p} + t_{N-2n_C-2} \cdot \tilde{p} + \cdots + t_1 \cdot \tilde{p} + t_1 \cdot \tilde{p} \\ &= \tilde{p} \left( p^{n_C-n_C^1} t_{N-2n_C-1} + \sum_{j=1}^{N-2n_C-2} t_j + t_1 \right) \end{aligned} \quad (7.100)$$

and

$$t_j = \frac{1}{\sqrt{1-4p^*}} \left[ \left( \frac{1 + \sqrt{1-4p^*}}{2} \right)^j - \left( \frac{1 - \sqrt{1-4p^*}}{2} \right)^j \right]. \quad (7.101)$$

Thus we can compute the probability of observing at least one  $n_C$ -crack in a chain of length  $N$  via

$$\begin{aligned} & C_N(n_C) \\ &= \mathbb{P}(C_{\min}(n_C, \omega) \leq N - n_C + 1) \\ &+ \sum_{n_C^1=n_C-1}^1 \left( p^{n_C^2} - D_{N-n_C-n_C^1} \right) (1-p) p^{n_C^1} \\ &= \sum_{k=1}^{N-n_C-2} t_k \tilde{p} + t_{N-n_C-1} p^{n_C} \\ &+ \sum_{n_C^1=n_C-1}^1 \left( p^{n_C^2} - \tilde{p} \left( p^{n_C-n_C^1} t_{N-2n_C-1} + \sum_{j=1}^{N-2n_C-2} t_j + t_1 \right) \right) (1-p) p^{n_C^1} \end{aligned} \quad (7.102)$$

Let us consider a given critical crack length  $L_C$  leading to failure of the component. Given the grain size we can therewith calculate the probability of failure of a chain

## Microscopic Damage Accumulation Models

### 7. Crack Propagation and Grain Morphology

---

with  $N$  grains, also considering crack growth all around. We now again compute the partial derivative of the total crack probability with respect to  $p$  and use the results in the following chapter to obtain the lifetime results and for fitting the model.

$$\begin{aligned}
& \frac{\partial}{\partial p} C_N \\
&= \frac{\partial}{\partial p} \left( \mathbb{P}(C_{\min}(n_C, \omega) \leq N - n_C + 1) + \sum_{n_C^1 = n_C - 1}^1 (p^{n_C^2} - D_{N - n_C - n_C^1}) (1 - p) p^{n_C^1} \right) \\
&= \frac{\partial}{\partial p} (\mathbb{P}(C_{\min}(n_C, \omega) \leq N - n_C + 1)) \\
&\quad + \sum_{n_C^1 = n_C - 1}^1 \frac{\partial}{\partial p} \left( (p^{n_C^2} - D_{N - n_C - n_C^1}) (1 - p) p^{n_C^1} \right) \\
&= \frac{\partial}{\partial p} \left( \sum_{k=1}^{N - n_C - 2} t_k \tilde{p} + t_{N - n_C - 1} p^{n_C} \right) \\
&\quad + \sum_{n_C^1 = n_C - 1}^1 \frac{\partial}{\partial p} \left( \left( p^{n_C^2} - \tilde{p} \left( p^{n_C - n_C^1} t_{N - 2n_C - 1} + \sum_{j=1}^{N - 2n_C - 2} t_j + t_1 \right) \right) (1 - p) p^{n_C^1} \right).
\end{aligned} \tag{7.103}$$

In equation (7.41) we have already calculated

$$\frac{\partial}{\partial p} (\mathbb{P}(C_{\min}(n_C, \omega) \leq N - n_C + 1)), \tag{7.104}$$

so we now compute the left part of the partial derivative with respect to  $p$

$$\begin{aligned}
& \sum_{n_C^1 = n_C - 1}^1 \frac{\partial}{\partial p} \left( (p^{n_C^2} - D_{N - n_C - n_C^1}) (1 - p) p^{n_C^1} \right) \\
&= \sum_{n_C^1 = n_C - 1}^1 \frac{\partial}{\partial p} \left( \left( p^{n_C^2} - \tilde{p} \left( p^{n_C - n_C^1} t_{N - 2n_C - 1} + \sum_{j=1}^{N - 2n_C - 2} t_j + t_1 \right) \right) (1 - p) p^{n_C^1} \right).
\end{aligned} \tag{7.105}$$

## Microscopic Damage Accumulation Models

### 7. Crack Propagation and Grain Morphology

---

Let again  $j$  and  $n_C^1$  be fixed. We compute the partial derivative for one addend in the following

$$\begin{aligned}
 & \frac{\partial}{\partial p} \left( \left( p^{n_C^1} - \tilde{p} \left( p^{n_C^1 - n_C^1} t_{N-2n_C-1} + \sum_{j=1}^{N-2n_C-2} t_j + t_1 \right) \right) (1-p)p^{n_C^1} \right) \\
 &= \frac{\partial}{\partial p} \left( p^{n_C^1} (1-p)p^{n_C^1} - \tilde{p} p^{n_C^1} (1-p)p^{n_C^1} t_{N-2n_C-1} - \tilde{p} (1-p)p^{n_C^1} (t_j + t_1) \right) \quad (7.106) \\
 &= \frac{\partial}{\partial p} \left( \tilde{p} - \tilde{p}^2 t_{N-2n_C-1} - \tilde{p} p^*(t_j + t_1) \right).
 \end{aligned}$$

We use the results from the previous section and obtain

$$\begin{aligned}
 & \frac{\partial}{\partial p} t_j \\
 &= \frac{\partial}{\partial p} \left( \left( \frac{1 + \sqrt{1-4p^*}}{2} \right)^j - \left( \frac{1 - \sqrt{1-4p^*}}{2} \right)^j \right) \quad (7.107) \\
 &= j \frac{(n_C^1 + 1)p^{n_C^1} - n_C^1 p^{n_C^1-1}}{\sqrt{1-4p^*}} \left[ \left( \frac{1 + \sqrt{1-4p^*}}{2} \right)^{j-1} + \left( \frac{1 - \sqrt{1-4p^*}}{2} \right)^{j-1} \right]
 \end{aligned}$$

and further

$$\begin{aligned}
 & \frac{\partial}{\partial p} t_{N-2n_C-1} \\
 &= (N - n_C - 2) \frac{(n_C^1 + 1)p^{n_C^1} - n_C^1 p^{n_C^1-1}}{\sqrt{1-4p^*}} \quad (7.108) \\
 & \quad \cdot \left[ \left( \frac{1 + \sqrt{1-4p^*}}{2} \right)^{N-n_C-3} + \left( \frac{1 - \sqrt{1-4p^*}}{2} \right)^{N-n_C-3} \right],
 \end{aligned}$$

as well as

$$\begin{aligned}
 & \frac{\partial}{\partial p} t_1 \\
 &= \frac{(n_C^1 + 1)p^{n_C^1} - n_C^1 p^{n_C^1-1}}{\sqrt{1-4p^*}} \left[ \left( \frac{1 + \sqrt{1-4p^*}}{2} \right) + \left( \frac{1 - \sqrt{1-4p^*}}{2} \right) \right]. \quad (7.109)
 \end{aligned}$$

# Microscopic Damage Accumulation Models

## 7. Crack Propagation and Grain Morphology

---

We obtain for the partial derivative of the whole expression

$$\begin{aligned}
& \frac{\partial}{\partial p} \left( \tilde{p} - \tilde{p}^2 t_{N-2n_C-1} - \tilde{p} p^* (t_j + t_1) \right) \\
&= n_C p^{n_C-1} - (n_C + 1) p^{n_C} \\
&\quad - \left( 2n_C p^{2n_C-1} - (4n_C + 2) p^{2n_C} + (2n_C + 2) p^{2n_C+1} \right) t_{N-2n_C-1} + \tilde{p}^2 \frac{\partial}{\partial p} t_{N-2n_C-1} \\
&\quad + \left( (n_C + n_C^1) p^{n_C+n_C^1-1} - 2(n_C + n_C^1 + 1) p^{n_C+n_C^1} + (n_C + n_C^1 + 2) p^{n_C+n_C^1+1} \right) \\
&\quad \cdot (t_j + t_1) + \tilde{p} p^* \frac{\partial}{\partial p} (t_j + t_1)
\end{aligned} \tag{7.110}$$

Similar to the first approach we can use the derivative with respect to  $p$  to obtain the derivative of the total crack probability with respect to  $n$

$$\begin{aligned}
f_N(n) &= \frac{\partial}{\partial n} F_N(n) \\
&= \frac{\partial}{\partial n} F_N(n_C, p(n, \sigma)) \\
&= \frac{\partial}{\partial p} C_N(n_C, p(n, \sigma)) \cdot f_{SF}(n)
\end{aligned} \tag{7.111}$$

where

$$\begin{aligned}
p(n) &= F_{SF}(n) \\
&= \mathbb{P} \left( CMB^{-1} \left( RO \left( RO^{-1}(\epsilon_a) \cdot \frac{m(U)}{\lambda} \right) \right) \leq n \right)
\end{aligned} \tag{7.112}$$

and

$$f_{SF}(n) = \frac{\partial}{\partial n} F_{SF}(n) \tag{7.113}$$

denote the single grain crack probability and the according density based on the Schmid factor distribution as well as  $\frac{\partial}{\partial p} C_N$  as calculated before. This approach is again enlarged to two dimensions similar to (7.41), wherefore we again consider a grid of size  $N = N_1 \times N_2$ . We are still focussing on cracks growth in one direction considering cracks on the whole circumference, which can occur in each of the grain layers.

Transferring the probability distributions of one to multiple layers we obtain analogously to the model without edges

$$F_N(n_C, p(n, \sigma)) = 1 - (1 - F_{N_2}(n_C, p(n, \sigma)))^{N_1} \tag{7.114}$$

# Microscopic Damage Accumulation Models

## 7. Crack Propagation and Grain Morphology

---

and

$$\frac{\partial}{\partial n} F_N(n_C, p(n, \sigma)) = N_1 (1 - F_{N_2}(n_C, p(n, \sigma)))^{N_1 - 1} \cdot \left( \frac{\partial}{\partial p} C_N(n_C, p(n, \sigma)) \cdot f_{SF}(n) \right), \quad (7.115)$$

where  $C_N$  is the probability of an  $n_C$  crack of one layer with connected edges.

We now briefly look at the differences between both distributions.

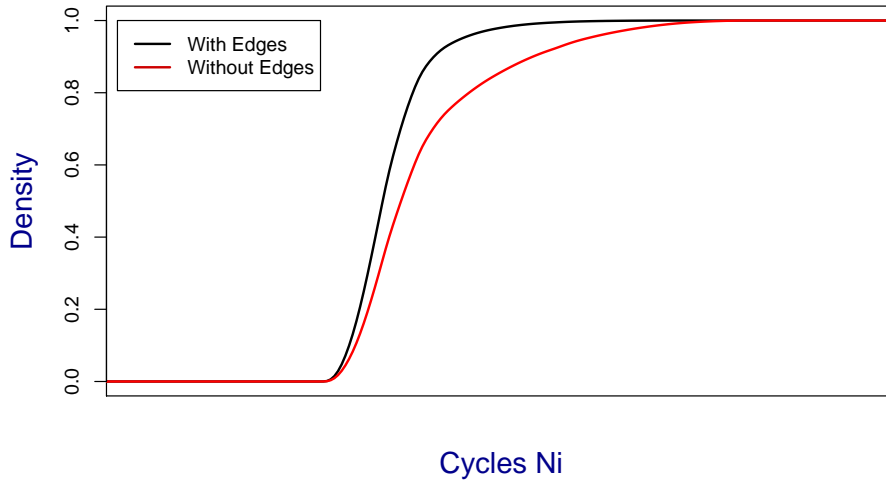


Figure 7.24.: Distributions with and without Edges -  $N = 5$ ,  $n_c = 3$

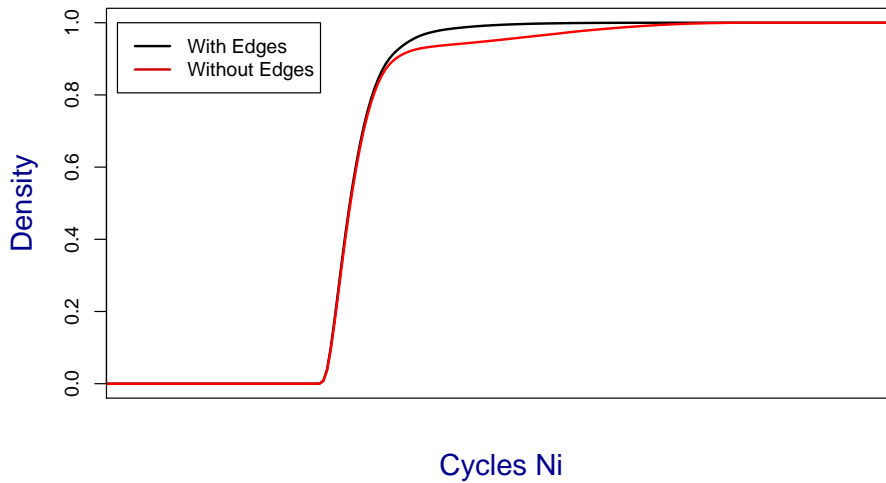


Figure 7.25.: Distributions with and without Edges -  $N = 10$ ,  $n_c = 2$

## Microscopic Damage Accumulation Models

### 7. Crack Propagation and Grain Morphology

---

As assumed the distribution without considering the edges is lower compared to the other one enabling crack around the whole circumference. As the crack is not restricted to given edges and therewith a limited start and end point, there are more possibilities.

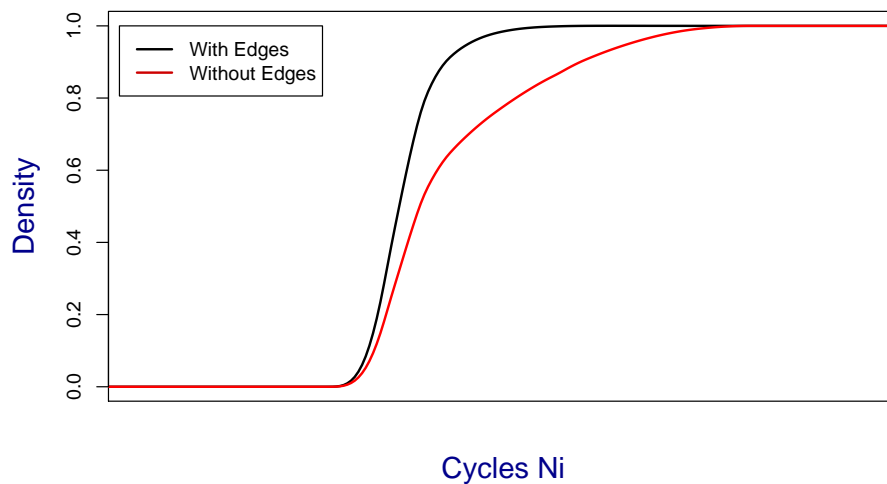


Figure 7.26.: Distributions with and without Edges -  $n_C = 5$ ,  $N = 10$

For a given number of grains  $N$  the deviations between both distributions increases for growing sizes of cracks, since the position of the crack is more and more limited. We can see in figure 7.26 that the distribution for the model without edges is more flat in comparison to the first model.

7. Crack Propagation and Grain Morphology

---

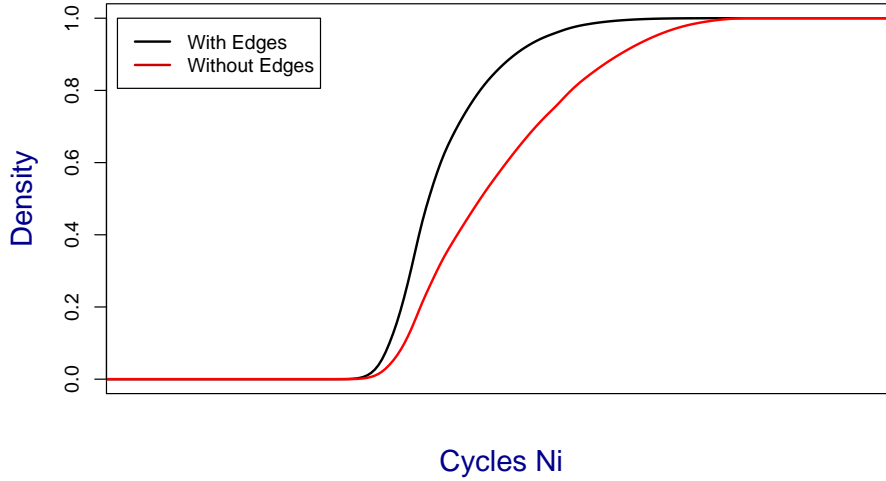


Figure 7.27.: Distributions with and without Edges -  $n_C = 8$ ,  $N = 10$

These results are used to compute the probability of failure for a discretized component and for fitting the model. Therefore, the hazard rate  $h_A$  of a given surface  $A$  needs to be calculated locally. Now let  $A = N_1 \cdot N_2$ . The cumulative hazard for a given surface  $A$  is

$$\begin{aligned} H_A(n, \sigma) &= -\log S_A(n, \sigma) \\ &= -\log (1 - F_{N_2}(n_C, p(n, \sigma)))^{N_1}. \end{aligned} \quad (7.116)$$

We can approximate

$$H(\sigma, n) \approx \frac{H_A(\sigma, n)}{A} \quad (7.117)$$

as local cumulative hazard function. Therefore, we calculate  $H_A(n, \sigma)$  for growing surface  $A$  and different combinations of  $n_C$  and  $\sigma$ . Depending on the combination we obtain different slopes of the hazards, which is shown in figure 7.28.

7. Crack Propagation and Grain Morphology

---

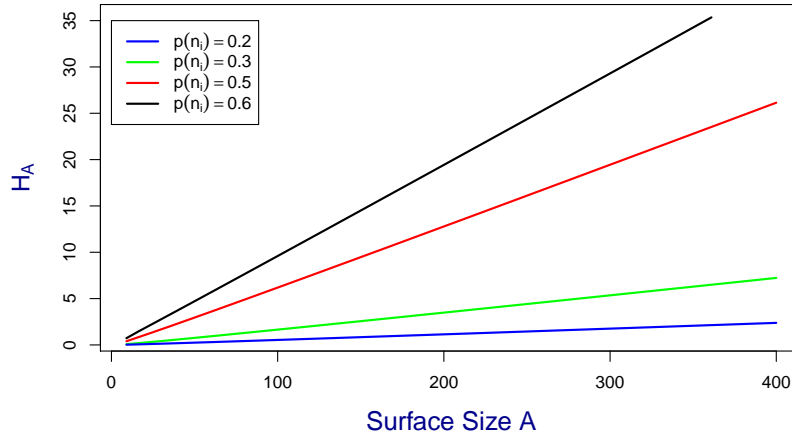


Figure 7.28.: Dependency of Size and Hazard Function for Different  $p(n, \sigma)$

Considering the individual size effect of each combination we can compute the local hazard, which can be transferred to arbitrary surfaces  $A$  to obtain the probability of failure

$$PoF(n) = 1 - e^{-\int_A H(\sigma(x), n) dA}. \tag{7.118}$$

### 7.3. Voronoi Polycrystal Model

To describe polycrystalline material with regards to the introduced cell model approach Voronoi diagrams are frequently used and offer several advantages, since there are many well-known questions and according applications. The main structure is closely related to the cell model we have introduced before.

The Voronoi diagram subdivides an area with given points into convex polygons. The so-called bisector represents the border between two different cells containing the according point. This border has the same distance to each of the points of the neighbored cells. The Voronoi cells are therewith generated in dependency of the point set.

In our case the point set is simulated according to a given region and size distribution for the grains, such that we can transfer the results to the standard specimen with given grain structures.

7. Crack Propagation and Grain Morphology

---

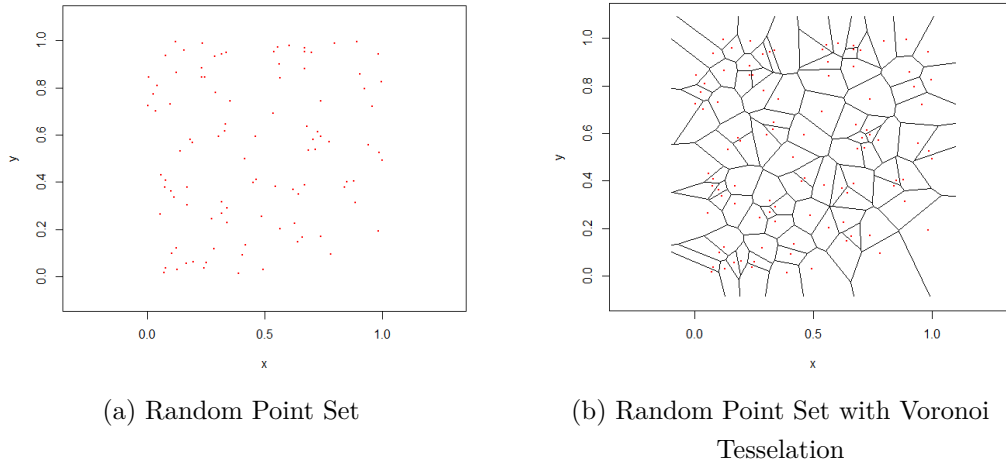


Figure 7.29.: Voronoi Tessellation for Random Point Set

Let us consider an area  $A = [0, 1] \times [0, 1]$ , which we intend to subdivide into different regions, each one representing a grain. In general we consider a set of  $N$  points with positions  $r_1, r_2, \dots, r_N$  in two dimensions. Associated to the  $i$ th point let  $r_i$  be the Voronoi cell and therewith the region of space being nearer to the point than to any other point in the set.

To randomly subdivide the region  $A$  let us consider the coordinates to be uniformly distributed on  $A$ . Figure 7.29a shows an example of a simulated set of points on the given surface. In this case there are 100 Voronoi cells. The resulting Voronoi diagram is shown in figure 7.29b. Let the crack probability of a single grain be  $p \in [0, 1]$ , which will be replaced by the single crack probability depending on given stress states, material constants and number of proceeded cycles. Based on the single crack probability for each grain, we randomly select grains to be cracked. In figure 7.29b we simulated random occurring cracks with probability  $p = 0.2$  for each of the 100 grains and highlighted them. Thus,

$$\mathbb{P}(X_k = 1) = 0.2, \quad \mathbb{P}(X_k = 0) = 0.8, \quad (7.119)$$

where  $k = 1, \dots, 100$ . In our case we are looking for subgraphs showing a certain property, namely being cracked. Therefore we need the following definition.

**Definition 7.1** (Connected Components). *An undirected graph  $G = (V, E)$  is **connected**, if for each vertex  $v \in V$  there exists a path to every other vertex  $u \in V$ . A **connected component** is defined as the maximal connected subgraph  $G' \subseteq G$  of an undirected graph  $G$ .*

# Microscopic Damage Accumulation Models

## 7. Crack Propagation and Grain Morphology

---

We are interested in cracks growing throughout the grains. We consider nearest neighbored cells, i.e. cells that share a Voronoi edge, showing a crack to belong to one connected component. In figure 7.30 the adjacent grains, which are cracked, are connected by their edges. The connected components correspond to the clusters of the previous chapter, varying in terms of the fact, that the distances in the previous cell models are equidistant and the lattices are regular.

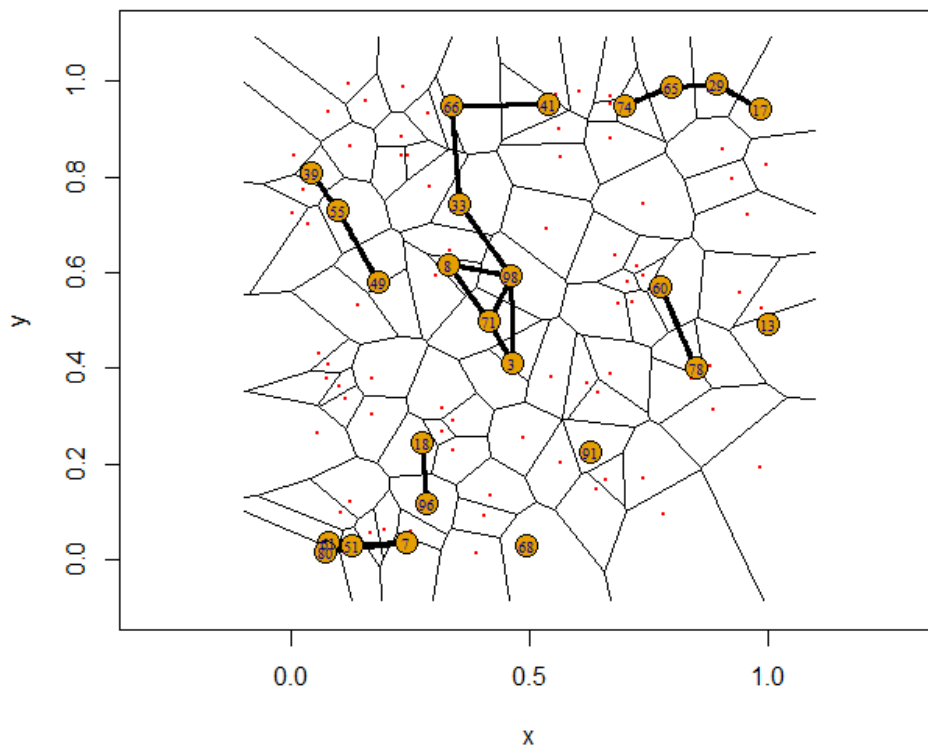


Figure 7.30.: Voronoi Tessellation with Subgraphs

Algorithm 5 shows the procedure of generating the voronoi graph and finding subgraphs in more detail.

Figure 7.31 shows the graph with highlighted cracked grains, such that the sizes of the connected components and therewith the crack sizes are visualized.

7. Crack Propagation and Grain Morphology

**Algorithmus 5** : Generation of Random Graphs and Connected Sub-graphs

**Data** : Single Grain Crack Propability  $p$ , Number of Grains  $N_G$ , Surface  $A = [x_-, x_+] \times [y_-, y_+]$ , Number of simulated Graphs  $N_{MC}$

**Result** : List of  $N_{MC}$  Graphs with Node Lists for connected Clusters each

```

for all simulation steps  $k = 1, \dots, N_{MC}$  do
1 |   Generate  $N_G$  randomly uniform distributed points  $g_i$  with
   |    $i = 1, \dots, N_G$ ;
2 |   Create Voronoi diagram and graph  $G = \{V, E\}$  for surface  $S$  and
   |   points  $g_i$ ;
   |   for all points  $g_i$   $i = 1, \dots, N_G$  do
   |   |   Generate crack property  $z$  with  $z \sim B_p$  with single grain crack
   |   |   probability  $p$ 
   |   end
3 |   Find all connected components with  $z = 1$ ;
4 |   Store list of graph information and node list of connected components;
end
    
```

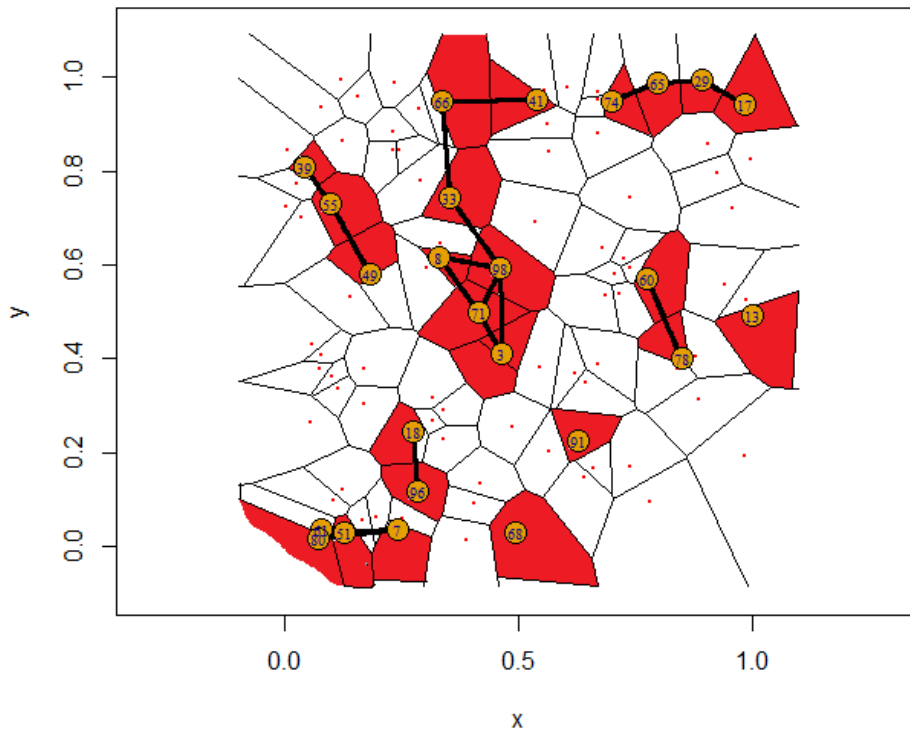


Figure 7.31.: Voronoi Tessellation with Subgraphs

Depending on the size of the surface, the grain size and the underlying stress states, the individual crack sizes and directions need to be assessed with regard to their

# Microscopic Damage Accumulation Models

## 7. Crack Propagation and Grain Morphology

---

contribution on occurring damage. In the following we introduce different failure criteria and thereby follow [28] and [3].

The calculations are made for each possible pair of two nodes  $r_i$  and  $r_j$ ,  $i, j = 1, \dots, k$ , belonging to one subgraph. We introduce two crack criteria, which are closely related. The first crack criteria is the maximum crack opening stress of one connected component

$$\sigma_s = |t_{ij}| \frac{\pi}{2} n_{ij}^T \sigma n_{ij}, \quad (7.120)$$

where  $t_{ij} = r_i - r_j$ ,  $i, j = 1, \dots, k$ , is the vector between two grains of one subgraph and  $n_{ij}$  is the according normal vector. The second failure criteria is the so-called stress intensity factor, or simply K-factor

$$K_I = 1.1215 \cdot n_{ij}^T \sigma n_{ij} \cdot \sqrt{\pi \frac{|t_{ij}|}{2}}, \quad (7.121)$$

where  $K_I$  is the K-factor including cracks of mode I, which we are interested in. It describes the stress distribution at its crack tip. Thereby the factor of 1.1215 is dependent on the geometry and the crack position we are considering. To obtain maximum possible values within one cluster we calculate

$$\sigma_s^* = \max_{i,j=1,\dots,k} |t_{ij}| \frac{\pi}{2} n_{ij}^T \sigma n_{ij}, \quad (7.122)$$

and

$$K_I^* = \max_{i,j=1,\dots,k} 1.1215 \cdot n_{ij}^T \sigma n_{ij} \cdot \sqrt{\pi \frac{|t_{ij}|}{2}}, \quad (7.123)$$

so we maximize over all possible combinations between two grains in one subgraph. Both crack criteria consider stress and the direction of the crack. Additionally we can calculate the crack size in total and in  $x$ -direction only, which, in the case of uniaxial load, corresponds to mode I cracks. We consider for each cluster

$$C = \max_{i,j=1,\dots,k} |t_{ij}| \quad (7.124)$$

and

$$C_x = \max_{i,j=1,\dots,k} |e_1 r_i - e_1 r_j|. \quad (7.125)$$

In the following we use these failure criteria to decide whether a generated graph is critical or not. We need to define a limit for each and consider real conditions of our specimen. Let the gauge length be 18mm, diameter  $d = 7$  and the circumference 22mm. We consider a penny shaped crack and calculate the crack length along the circumference, which needs to be reached for a critical crack size by considering a

## Microscopic Damage Accumulation Models

### 7. Crack Propagation and Grain Morphology

---

failure criteria of 5% drop in stress. Therewith, we obtain the critical crack length by solving

$$\frac{\varphi}{2\pi} - \left| \frac{\sin \varphi}{2\pi} \right| = 2.5\% \quad (7.126)$$

and computing

$$C^* := 3.5\pi \frac{\varphi}{\pi} mm. \quad (7.127)$$

In our case we obtain a critical crack length of  $C^* = 3.022618$ . Depending on the grain size and number we can generate a graph with the required properties as described before via algorithm 5 and evaluate the crack clusters with respect to the given criteria. Per grain number and single grain crack probability  $p \in [0, 1]$  we randomly generate 1000 graphs each. Since the percolation threshold is at 0.5, it is sufficient to generate the graphs for  $p \in [0, 0.5]$ . The single grains crack with probability according to the probabilities of the analytical percolation models is given by

$$\begin{aligned} p(n) &= F_{SF}(n) \\ &= \mathbb{P} \left( CMB^{-1} \left( RO \left( RO^{-1}(\epsilon_a) \cdot \frac{m(U)}{\lambda} \right) \right) \leq n \right) \end{aligned} \quad (7.128)$$

with number of cycles to failure  $n$  and Schmid factor  $m(U)$ . We can generate a sufficient large amount of Monte Carlo samples for each crack probability and number of grains for a given surface. These samples serve as a basis for the values of (7.128). Once the state of each Voronoi cell is fixed, the subgraphs are filtered and evaluated according to the given failure criteria to calculate the number of sufficiently cracked graphs. A method to find the subgraphs and compute the criteria is given in algorithm 5.

The following we look at the resulting distributions depending on grain size and number. With the conditions as given before we consider a circumferential surface of approximately  $374mm^2$  and compare the distributions for grain numbers  $N = 50, 75, 100$  and different crack criteria.

Let the failure criteria be  $C = 3$  and the Voronoi region fixed and as given above. Figure 7.32 shows the densities for different numbers of grains.

# Microscopic Damage Accumulation Models

## 7. Crack Propagation and Grain Morphology

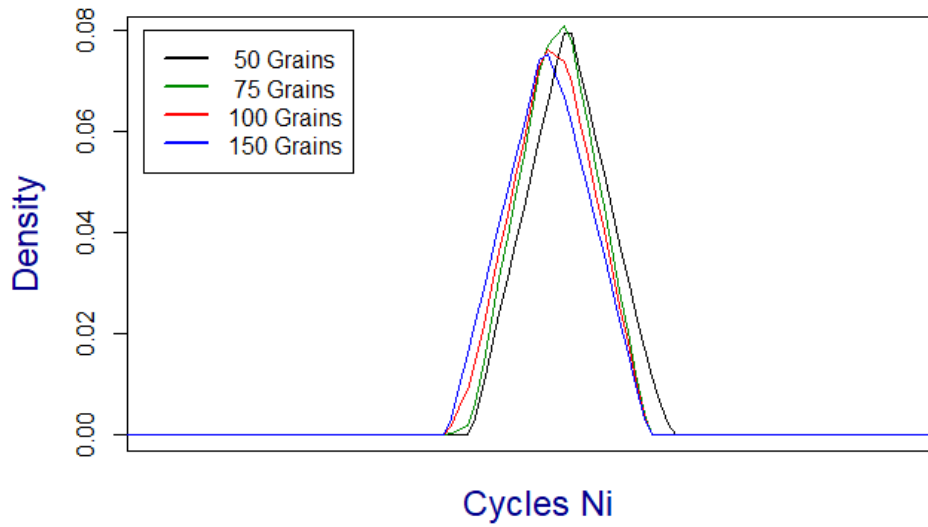


Figure 7.32.: Lifetime Densities resulting from Sample Voronoi Tessellation

With an increasing number of grains the densities are shifted to the left.

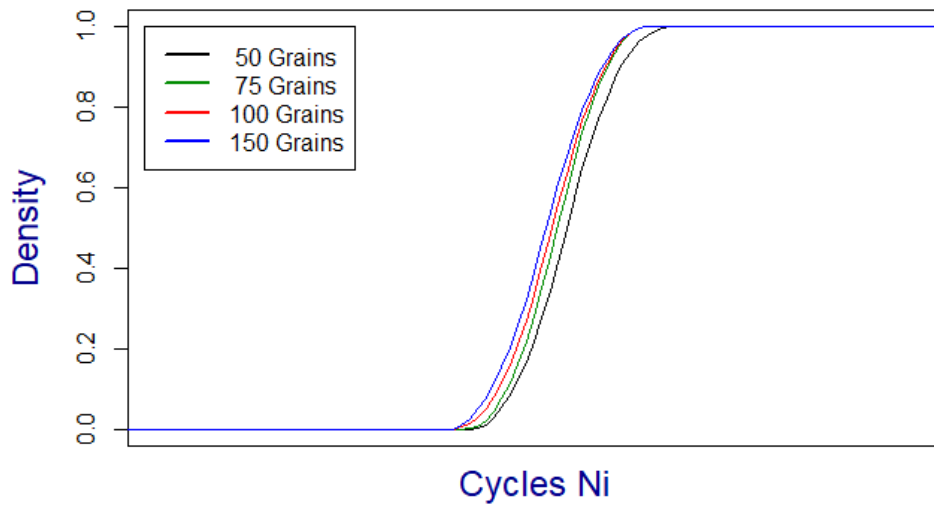


Figure 7.33.: Distributions Voronoi Tessellation for  $C = 3$

The mean number of cycles, which are given in table 7.1, deviate. The density of the analytical model with 50 grains lies above both calculated according to the sample Voronoi tessellations.

Grain Number	50 Grains Vor.	150 Grains Vor.	50 Grains Ana.
Mean	7 579	6 300	10 968

Table 7.1.: Summary of Fatigue Life - Uniaxial and Multiaxial

# Microscopic Damage Accumulation Models

## 7. Crack Propagation and Grain Morphology

---

There is a longer LCF Lifetime in case of the analytical model compared to the Voronoi based models with a crack criteria of  $C = 3$  mm. An increasing number of grains results in a shorter LCF lifetime.

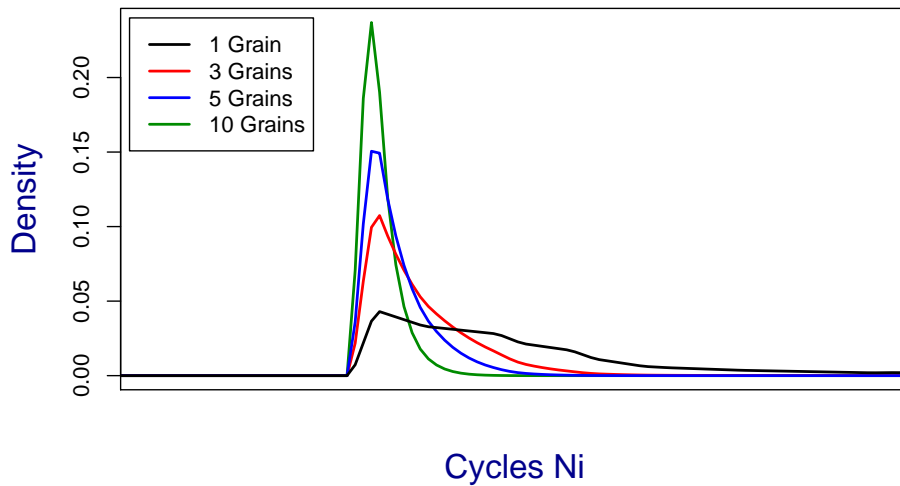


Figure 7.34.: LCF Lifetime Densities for Different Grain Numbers

Comparing this to the density change under an increasing number of grains in case of the analytical model, we see that in the latter one, the scatter of LCF lifetime becomes smaller and the form more sharp, but the minimum value is nearly equal. LCF lifetime density is more concentrated on shorter life for more grains.

Using the Voronoi tessellation the densities are shifted to shorter LCF life considering a higher amount of grains. The scatter is similar, but the mean value becomes lower, as table 7.1 shows.

7. Crack Propagation and Grain Morphology

---

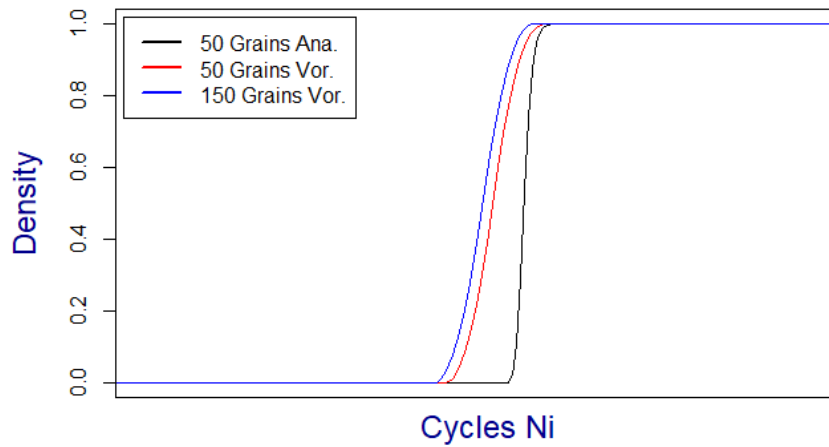


Figure 7.35.: Distributions Voronoi Tessellation for  $C = 3$  mm

The following we consider the results of the analytical model with  $N_1 = N_2 = 10$  and compare them to the sample Voronoi Tessellations with  $N = 100$ , both under uniaxial loading. We can see in figure 7.36 that the analytical model leads to longer LCF life. The increase is very sharp, as we have already seen before for a large number of grains. The mean value is approximately 5.000 cycles higher than with the same number of grains using Voronoi tessellation.

Looking at the densities the deviation in mean value is clearly noticeable. Also the fact that both densities of the Voronoi tessellation show a similar course, but are shifted to the left for an increasing grain number.

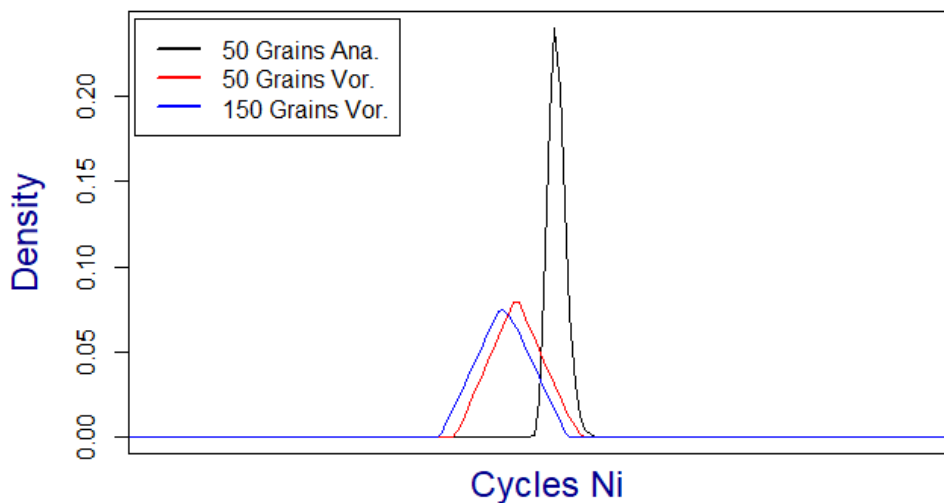


Figure 7.36.: Densities Voronoi Tessellation for  $C = 3$

## Microscopic Damage Accumulation Models

### *7. Crack Propagation and Grain Morphology*

---

We have seen that the models result in different LCF lifetime distributions. With the analytical models and the sample Voronoi tessellation it is possible to generate the probabilities of failure and hazard rates according to several conditions. We can vary the number and size of grains, the surface size, the loading state to be applied including uniaxial and multiaxial loadings, as well as different criteria to set and evaluate the amount damage.

The next chapter shows the application and transfer to the component, followed by fitting of the model to real data.

## 8. Fitting to Experimental LCF Lifetime Data

We introduced an approach to calculate probabilistic LCF fatigue lifetime based on cell models. Therefore we can vary the amount of stress and its level of multiaxiality. Additionally, we can modify the number and size of grains as well as the underlying surface area. The following we use the shown models to fit parameters of the Ramberg-Osgood equation 2.1 and Coffin-Manson-Basquin equation 3.2 to obtain material parameters fitting to given data, such that appropriate calculations of LCF fatigue life can be made.

We consider a given set of experimental data resulting from fatigue tests of Rene80 specimen applying different loading strengths. The initial material parameters, which we used for the fit, were provided by Siemens and will not be stated explicitly. Figure 8.1 shows a sample of 22 data points  $(n_{i,1}, \dots, n_{i,22})$ , where again both axes are in log – log scale.

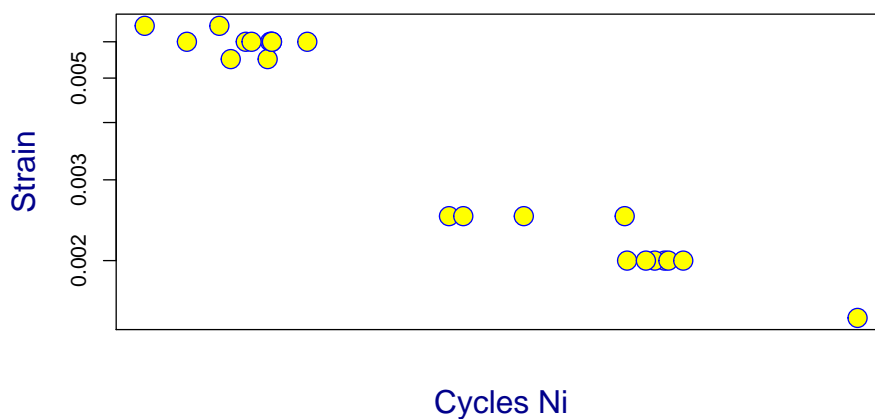


Figure 8.1.: Experimental Data at Different Strain Levels

# Microscopic Damage Accumulation Models

## 8. Fitting to Experimental LCF Lifetime Data

Our aim is to fit the material parameters  $\theta = (\sigma_f, \epsilon_f, c, b)$  to the given set of data. Based on this parameters and the according CMB relation the probability of failure can be calculated and transferred to the component. As a starting point  $\theta_0$  we consider parameters resulting in the CMB relation as given in figure 8.2.

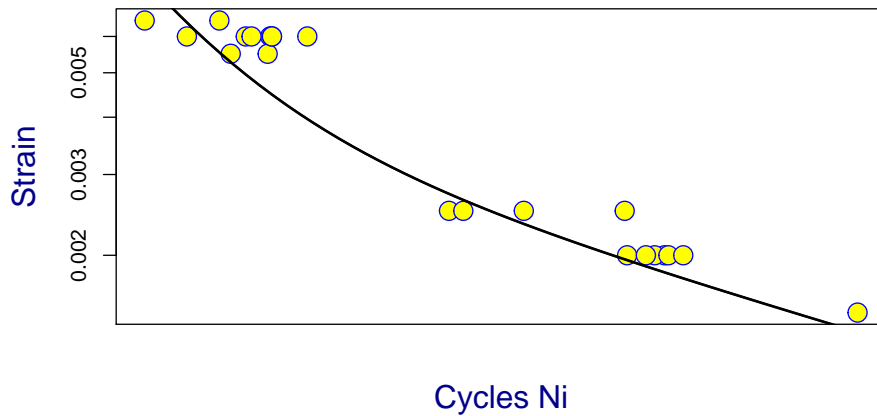


Figure 8.2.: Experimental Data with CMB at Initial Value

We consider the analytical model to calculate LCF fatigue life and the real size and grain number to optimize the parameters. We consider experiments with a length of the measuring section (gauge length) of 18mm, diameter  $d = 7\text{mm}$  and circumference of 21.991mm. We chose a grain size of 3mm based on assumptions on the material. Figure 8.3 shows an engineering drawing of the specimen.

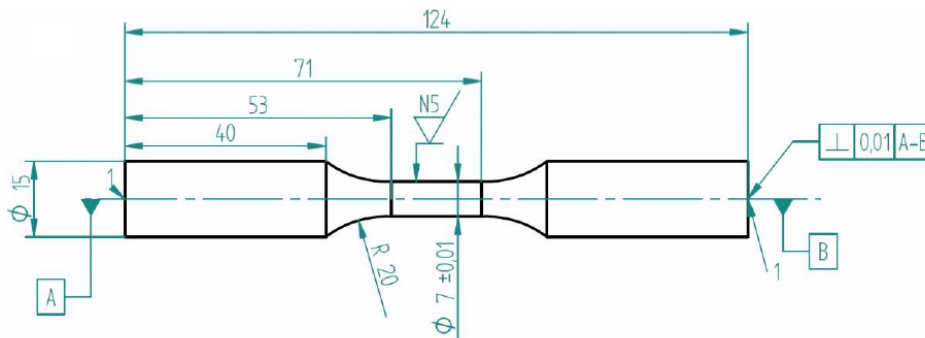


Figure 8.3.: Technical Drawing of Specimen, see also [8]

# Microscopic Damage Accumulation Models

## 8. Fitting to Experimental LCF Lifetime Data

---

According to the analytical model we consider

$$\begin{aligned}
 f_N(n|\theta) &= \frac{\partial}{\partial n} F_N(n|\theta) \\
 &= \frac{\partial}{\partial n} F_N(n_C, p(n, \sigma, \theta)|\theta) \\
 &= \frac{\partial}{\partial p} C_N(n_C, p(n, \sigma, \theta)|\theta) \cdot f_{SF}(n|\theta)
 \end{aligned} \tag{8.1}$$

where

$$\begin{aligned}
 p(n|\theta) &= F_{SF}(n|\theta) \\
 &= \mathbb{P} \left( CMB^{-1} \left( RO \left( RO^{-1}(\epsilon_a) \cdot \frac{m(U)}{\lambda} \right), \theta \right) \leq n | \theta \right)
 \end{aligned} \tag{8.2}$$

and

$$f_{SF}(n|\theta) = \frac{\partial}{\partial n} F_{SF}(n|\theta) \tag{8.3}$$

denote the single grain crack probability and the according density based on the Schmid factor distribution as well as  $\frac{\partial}{\partial p} C_N$  as calculated in section 7.2. We consider a grid of size  $N = N_1 \times N_2$  and multiple layers and therewith

$$F_N(n_C, p(n, \sigma, \theta)|\theta) = 1 - (1 - F_{N_2}(n_C, p(n, \sigma, \theta)|\theta))^{N_1} \tag{8.4}$$

and

$$\begin{aligned}
 \frac{\partial}{\partial n} F_N(n_C, p(n, \sigma, \theta)|\theta) &= N_1 (1 - F_{N_2}(n_C, p(n, \sigma, \theta)|\theta))^{N_1-1} \\
 &\quad \cdot \left( \frac{\partial}{\partial p} C_N(n_C, p(n, \sigma, \theta)|\theta) \cdot f_{SF}(n|\theta) \right),
 \end{aligned} \tag{8.5}$$

where  $N_1 = 7$  and  $N_2 = 6$ . Now let the density according to given parameters  $\theta \in \Theta$  be shortly denoted by  $f_N(n|\sigma, \theta)$ . The Likelihood function is defined as follows

$$\mathcal{L}(\theta) = \mathcal{L}(n_{i,1}, n_{i,2}, \dots, n_{i,l}|\theta) = f_N(n_{i,1}|\sigma_1, \theta) \cdot \dots \cdot f_N(n_{i,l}|\sigma_l, \theta) \tag{8.6}$$

and the according log-Likelihood is given as

$$\log \mathcal{L}(\theta) = \log \mathcal{L}(n_{i,1}, n_{i,2}, \dots, n_{i,l}|\sigma_1, \dots, \sigma_l, \theta) = \sum_{k=1}^l \log f_N(n_{i,k}|\sigma_k, \theta) \tag{8.7}$$

The parameters in our case are given as  $\theta = (\sigma_f, \epsilon_f, c, b)$ . We are looking for parameters, which maximize the underlying density value at each given data point and

# Microscopic Damage Accumulation Models

## 8. Fitting to Experimental LCF Lifetime Data

---

in total maximizes the probability of all fatigue test realizations. Therefore we are looking for values maximizing the log-Likelihood function, i.e.

$$\log \mathcal{L}(\theta) \rightarrow \max . \quad (8.8)$$

The Maximum Likelihood Estimator (MLE) is therewith given by

$$\hat{\theta}_{ML} = \operatorname{argmax}_{\theta \in \Theta} \log \mathcal{L}(\theta). \quad (8.9)$$

The densities  $f_N(n_{i,k}|\sigma_k, \theta)$  vary for each group of specimen not having an equal strain or stress level, as we can see in figure 8.4 and 8.5.

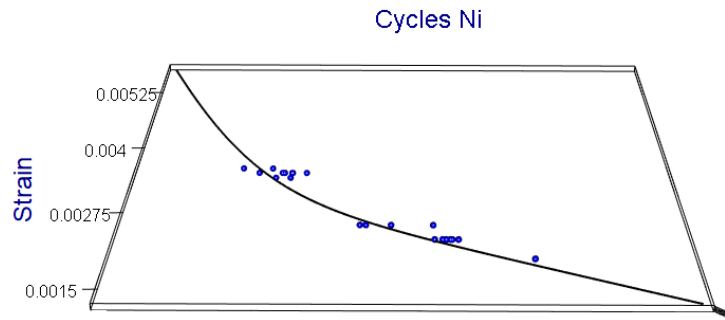


Figure 8.4.: LCF Fatigue Life Data and Initial CMB Relation

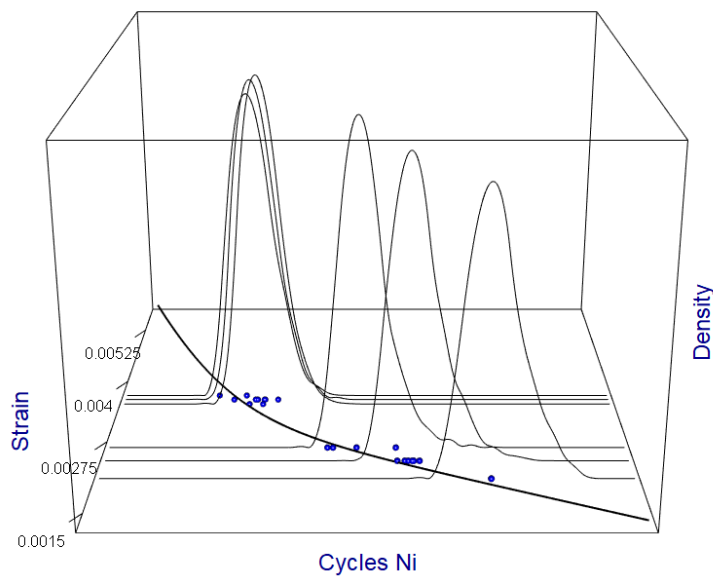


Figure 8.5.: Initial CMB Relation with LCF Life Densities,  $N_1 = 7$ ,  $N_2 = 6$ ,  $n_C = 2$

# Microscopic Damage Accumulation Models

## 8. Fitting to Experimental LCF Lifetime Data

As the values of critical number of cracked grains in a row  $n_C$  are discrete in the analytical model, we estimate one MLE for each  $n_C = 1, \dots, 7$  and compare the end values of the log-Likelihood function. The initial values and the corresponding function is shown by the dashed black line.

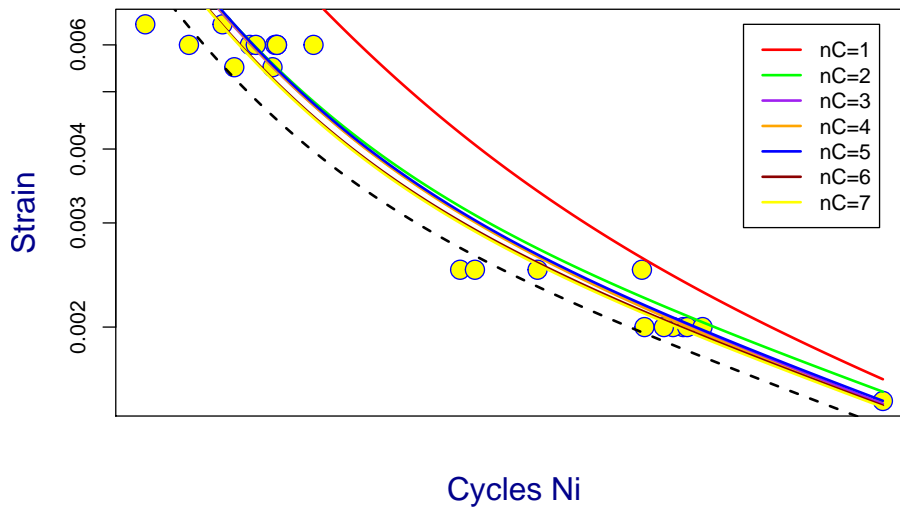


Figure 8.6.: Estimated CMB Parameters for Different Crack Sizes

The CMB relations with the estimated parameters show deviations for each crack length  $n_C$ . We can see that the red line with  $n_C = 1$  has the largest distance to the other CMB relations. This is due to the sharp shape of the density for such a large number of grains and layers, as visible in 7.36. The other lines, apart from the initial one, are very close to each other. If we evaluate all log-Likelihood functions with the estimated parameters of each critical crack number, we obtain the values shown in table 8.1.

$n_C$	1	2.	3	4	5	6	7
$-\log \mathcal{L}(n_C, \hat{\theta})$	225.58	180.72	149.55	103.16	89.64	85.25	82.99

Table 8.1.: Values of negative log-Likelihood functions for different  $n_C$

The highest value is given at  $n_C = 1$ , the lowest at  $n_C = 7$ . All values are in a range of 226 to 80. This is due to the fact that densities with higher critical crack number  $n_C$  are wider and cover the data points better. As the range of the densities are quite close to the scatter of specimen of one strain group, a change of CMB

## Microscopic Damage Accumulation Models

### *8. Fitting to Experimental LCF Lifetime Data*

---

parameters and therewith a shift of all densities leads to some data points being not covered. Thus, the values of negative log-Likelihood decrease for larger critical crack length.

## 9. Finite Elements Discretization and Transfer to Component

To calculate the probability of failure for a component, we use finite element discretization. To discretize the elasticity PDE in (3.5) we first introduce some fundamentals of finite element analysis [14], [2]. Let  $K \subseteq \mathbb{R}^3$  be a compact, connected Lipschitz set with non-empty interior called element domain. Further let  $P$  be a finite vector space of polynomials  $p : K \rightarrow \mathbb{R}$  and  $\Sigma(K) = \{\vartheta_1, \dots, \vartheta_{n_s}\}$  be linear functionals  $\vartheta_l : P(K) \rightarrow \mathbb{R}$  with  $\vartheta_{K,j}(p) = p(X_j)$ , which are also called the local degrees of freedom. A finite element is denoted by the triple  $\{K, P(K), \Sigma(K)\}$ .

The local shape functions  $\{\gamma_1, \dots, \gamma_{n_s}\}$  are basis functions  $\gamma_{K,k} \in P(K)$  satisfying  $\vartheta_{K,j}(\gamma_{K,k}) = \delta_{j,k}$ ,  $j, k \in \{1, \dots, n_s\}$ . If there are nodes  $\{X_1^K, \dots, X_{n_s}^K\} \in K$ , such that for all  $p \in P(K)$  it holds that  $\vartheta_{K,j}(p) = p(X_j^K)$ ,  $j \in \{1, \dots, n_s\}$ , we call it a Lagrange finite element.

Let  $\Delta_h$  be a finite element mesh on  $\Omega$  containing elements  $K_m$ ,  $m \in \{1, \dots, M_{el}\}$ , with non-empty interior and  $\{K_m\}_{1 \leq m \leq M_{el}}$  representing a partition of  $\Omega$ . By  $H_D^1(\Omega, \mathbb{R}^3)$  we denote the Sobolev space of  $L^2(\Omega, \mathbb{R})$  functions  $u$  with first derivatives  $\nabla u \in L^2(\Omega, \mathbb{R}^{3 \times 3})$ , such that  $u = 0$  on  $\partial\Omega_D$ . We consider a reference element  $\{\hat{K}, \hat{P}, \hat{\Sigma}(\hat{K})\}$  with a finite dimensional linear space of reference polynomials  $\hat{P}$ . Further considering a bijective transformation  $T_K : \hat{K} \rightarrow K$  for each  $K \in \Delta_h$ , such that  $\hat{P} = P \circ T_K$ ,  $\hat{\gamma}_j = \gamma_j \circ T_K$  and  $\hat{\vartheta}_j(p) = \vartheta_j(p \circ T_K)$  where  $j \in \{1, \dots, n_s\}$ , we can write

$$T_K(\hat{\psi}) = T_K(\hat{\psi}, X) = \sum_{j=1}^{n_s} \hat{\gamma}_j(\hat{\psi}) X_j^K, \quad \hat{\psi} \in \hat{K}. \quad (9.1)$$

Let  $X = \{X_1, \dots, X_M\} = \bigcup_{K \in \Delta_h} \{X_1^K, \dots, X_{n_s}^K\}$  be the set of all Lagrange nodes with index mapping

$$\begin{aligned} \Delta_h \times \{1, \dots, n_s\} &\rightarrow \{1, \dots, N\} \\ (K, r) &\rightarrow \hat{l}(K, r). \end{aligned} \quad (9.2)$$

# Microscopic Damage Accumulation Models

## 9. Finite Elements Discretization and Transfer to Component

---

We consider the set of global shape functions  $\{\vartheta_j : j \in \{1, \dots, M\}\}$ ,  $\vartheta_j : \Omega \rightarrow \mathbb{R}$ . Restricted to  $K \in \Delta_h$  the functions are in  $P(K)$  and if  $\exists k \in \{1, \dots, n_s\}$  such that  $\hat{l}(K, k) = j$ , then

$$\vartheta_{j|K} \left( X_m^K \right) = \delta_{mk}. \quad (9.3)$$

Thus,  $\vartheta_j(X_m) = \delta_{jm}$  for  $j, m \in \{1, \dots, N\}$ . Now let the volume force density be  $f \in \mathcal{L}^2(\Omega, \mathbb{R}^2)$  and surface load  $g \in \mathcal{L}^2(\partial\Omega_N, \mathbb{R}^2)$  as described in (2.2.1). The global finite element space  $H_h^1(\Omega, \mathbb{R})$  is the linear span of  $\{\vartheta_j : j \in \{1, \dots, M\}\}$ . Let  $H_h^1(\Omega, \mathbb{R}^3) = H_h^1(\Omega, \mathbb{R})^{\times 3}$ , then  $H_h^1(\Omega, \mathbb{R}^3) \subseteq H^1(\Omega, \mathbb{R}^3)$ . Let  $H_{D,h}^1(\Omega, \mathbb{R}^3)$  be the subspace of  $H_h^1(\Omega, \mathbb{R}^3)$  with  $H_{D,h}^1(\Omega, \mathbb{R}^3) = \{u \in H_h^1(\Omega, \mathbb{R}^3) | u = 0 \text{ on } \overline{\partial\Omega_D} \cap \{X_1, \dots, X_M\}\}$ , i.e. vanishing of  $u$  on boundary nodes. We are looking for a solution  $u \in H_{D,h}^1(\Omega, \mathbb{R}^3)$  to the discretized elasticity PDE fullfilling

$$B(u, v) = \int_{\Omega} f \cdot v dx + \int_{\partial\Omega_N} g \cdot v dA, \forall v \in H_{D,h}^1(\Omega, \mathbb{R}^3). \quad (9.4)$$

Because of the coercivity of the bilinear form, such a solution always exists and this also holds on  $H_{D,h}^1(\Omega, \mathbb{R}^3)$ .

To transfer the probability of failure  $PoF(t) = 1 - S(t) = 1 - e^{-J(\Omega, u)}$  to the component, the functional  $J(\Omega, u)$  needs to be discretized. This is given as an integral of the surface  $\partial\Omega$  with

$$J(\Omega, u) = \int_{\partial\Omega} H(\sigma(x), n, N, L_C) dA, \quad (9.5)$$

where  $H(\sigma(x), n, N, L_C)$  is obtained according to (7.117) and following. Let  $\mathcal{M}_h$  be the set of all  $M^f$  faces  $F$  of finite elements  $K = K(F) \in \Delta_h$  which are in  $\partial\Omega$ . Let the according face of the reference element  $\hat{K}$  be  $\hat{F}$  such that  $T_K : \hat{F} \rightarrow F$ . We consider quadrature points  $\hat{\psi}_l^F$  with weights  $\hat{\omega}_l^F$  on  $\hat{F}$ . The computation of the surface integral reduces to the evaluation of integrals over each element lying in  $\mathcal{M}_h$ , therewith

$$\begin{aligned} J(\Omega, u) &= \sum_{F \in \mathcal{M}_h} \int_F H(\sigma(x), n, N, L_C) dA \\ &= \sum_{F \in \mathcal{M}_h} \int_{\hat{F}} H(\sigma(\hat{T}_{K(F)}(\hat{x})), n, N, L_C) \sqrt{\det(g_F(\hat{x}))} d\hat{A} \\ &\approx \sum_{F \in \mathcal{M}_h} \sum_{l=1}^{l_q^F} \hat{\omega}_l^F H(\sigma(\hat{T}_{K(F)}(\hat{\psi}_l^F)), n, N, L_C) \sqrt{\det(g_F(\hat{\psi}))} d\hat{A}, \end{aligned} \quad (9.6)$$

with  $l_q^F$  Gauß points  $\{\hat{\psi}_l^F, \dots, \hat{\psi}_{l_q^F}^F\}$  and weights  $\{\hat{\omega}_l^F, \dots, \hat{\omega}_{l_q^F}^F\}$  being a quadrature on  $\hat{F}$ .  $\det(g_F(\hat{\psi}))$  denotes the Gram determinant, i.e. the determinant of the Gram

## Microscopic Damage Accumulation Models

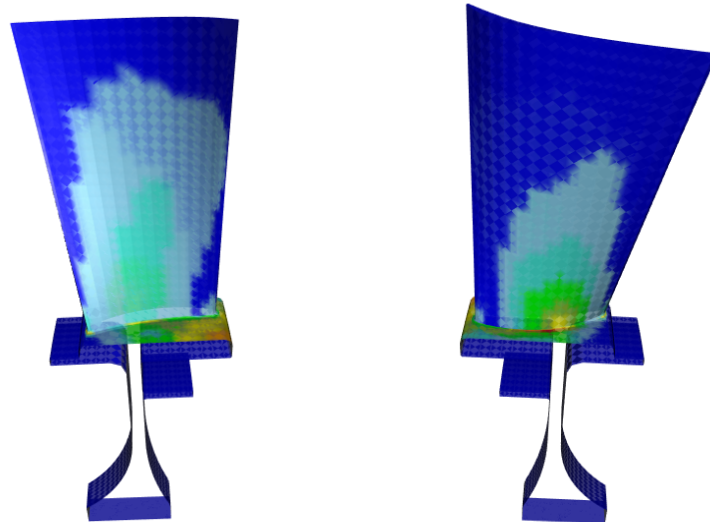
### 9. Finite Elements Discretization and Transfer to Component

---

matrix  $F(\hat{\psi}) = (J_F(\hat{\psi}))^T J_F(\hat{\psi})$  with  $J_F(\hat{\psi}) = \frac{\partial T_F(\hat{\psi})}{\partial \hat{\psi}}$  being the Jacobian matrix of  $T_F$ .

#### 9.1. Example: Application to a Blisk-Geometry

As an example, we show the results of probabilistical lifetime calculation for a Bladed Disk. We consider a volume force resulting from centrifugal load from a rotation. Air pressure surface loads are not considered. The FEA discretization consists of 13 682 nodes with 1 838 brick elements with 20 degrees of freedom and reduced quadrature  $l_q = 8$ . The surface quadrature points are selected such that  $l_q^F = 16$ .



(a) Stress State of Blade - front

(b) Stress State of Blade - back

Figure 9.1.: Front and back view of a blisk with according von Mises stress under centrifugal loading resulting from a rotation

Figures 10.2a and 10.2b show the von Mises stress of the component. For the calculation of crack intensity we use (7.117) and (7.116), respectively. For (7.128) we use the fitted CMB and RO parameters of the Voronoi percolation model as given in 8. We determine the failure criteria  $C^* = 3$  mm according to material properties of (7.36) to apply realistic conditions. The direction of stress and factor of multi-axiality are also taken into consideration of the model. The crack intensity increases with the number of loading cycles. The intensity is colored from blue to red. At the beginning of the loading there is no damage (9.3a, 9.3b).

*9. Finite Elements Discretization and Transfer to Component*

---

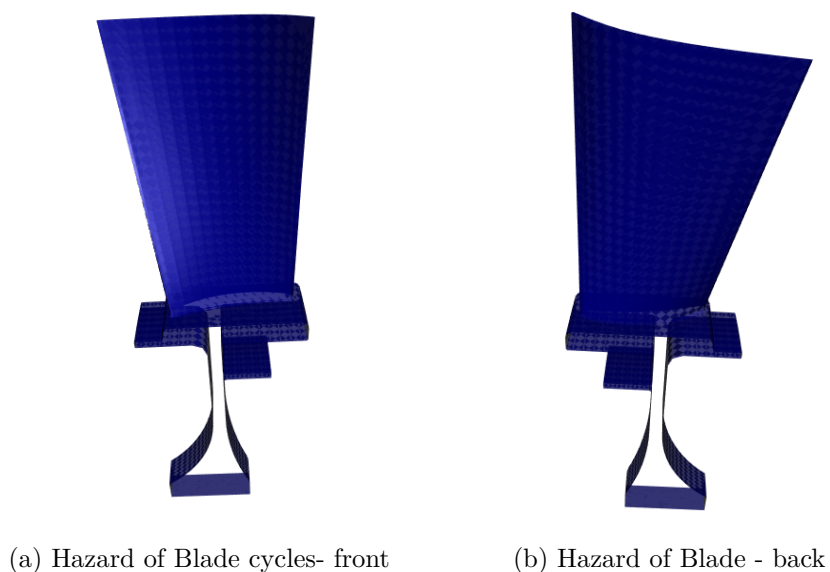


Figure 9.2.: Cumulative hazard previous to the loading, figure 9.3a shows the front, 9.3b the back side of the component, intensity from blue to red

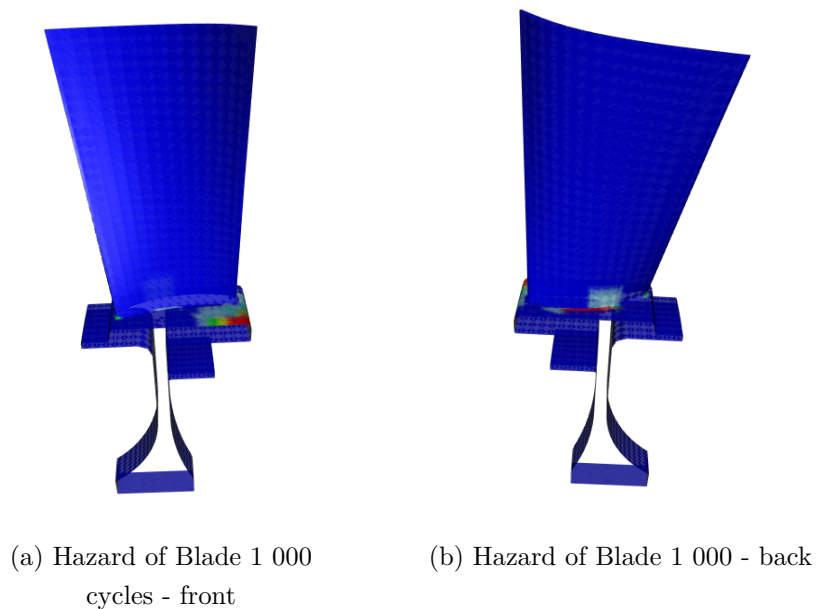


Figure 9.3.: Cumulative hazard after a number of 1 000 cycles, figure 9.4a shows the front, 9.4b the back side of the component, intensity from blue to red

## Microscopic Damage Accumulation Models

### *9. Finite Elements Discretization and Transfer to Component*

---

After 1 000 loading cycles there is a high crack intensity at the transition between blade and blade root at the back of the component as well as at the right edge in the front.

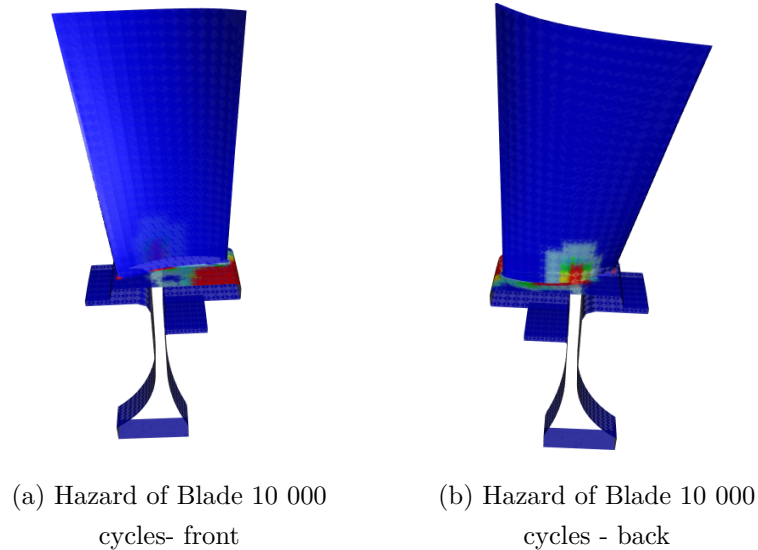


Figure 9.4.: Cumulative hazard after a number of 10 000 cycles, figure 9.4a shows the front, 9.4b the back of the component, intensity from blue to red

An increasing number of loading cycles leads to an expand of the area and a strengthening of crack intensity in the front and in the back.

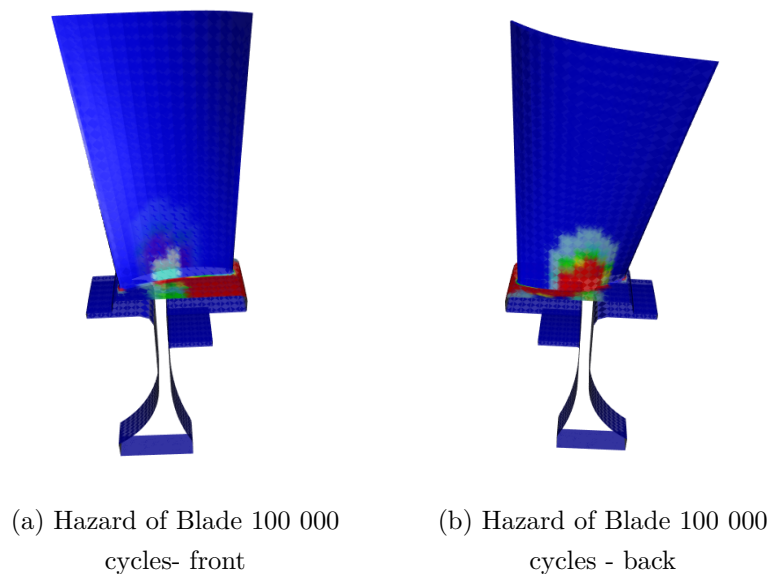


Figure 9.5.: Cumulative hazard after a number of 100 000 cycles, figure 9.5a shows the front, 9.5b the back side of the blade, intensity from blue to red

## 10. Probabilistic Damage Accumulation and Rainflow Counting

To evaluate loading cycles with respect to their individual size and intensity, damage parameter can be used. Applying a deterministic approach hysteresis loops can be classified and counted according to their strength by the Rainflow counting method, which we have already introduced in chapter 3.3.1. We have shown a slip system based approach and a counting algorithm for 3 different stress states and a face-centered cubic crystal.

In the following, we combine the slip system based approach with random orientation of the grains and transfer it to the random Schmid factor model. Therewith, we obtain a probabilistic damage parameter dependend on different stress states with according levels of multiaxiality. The methods for calculating probablistic damage parameter as well as the results are shown in the following.

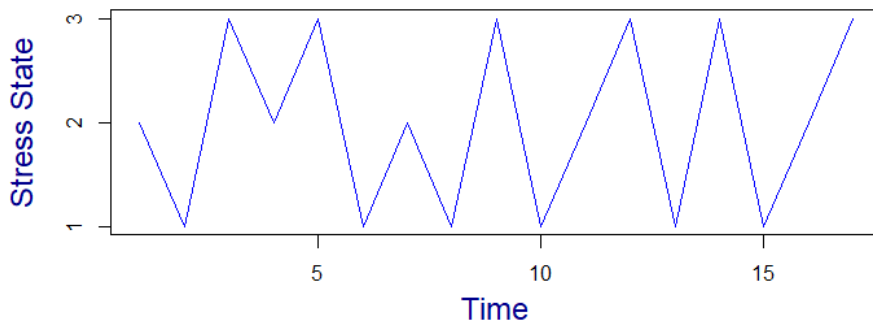


Figure 10.1.: Stress History with  $T = 17$

According to the procedure shown in 3.3.1 we consider 3 different stress states  $\sigma_{rep,1}, \sigma_{rep,2}, \sigma_{rep,1}$  and the appropriate sequence of stress scenarios

$$\sigma_{hist} = \begin{pmatrix} \sigma_{hist,0} \\ \sigma_{hist,1} \\ \vdots \\ \sigma_{hist,T} \end{pmatrix} \quad (10.1)$$

## Microscopic Damage Accumulation Models

### 10. Probabilistic Damage Accumulation and Rainflow Counting

---

with  $\sigma_{hist,t} \in \{\sigma_{rep,1}, \sigma_{rep,2}, \sigma_{rep,3}\}$ ,  $t = 0, 1, \dots, T$ . Figure 10.1 shows an example course with time  $T = 17$ . The sequence is given by

$$\sigma_{hist} = \begin{pmatrix} \sigma_{rep,2} \\ \sigma_{rep,1} \\ \sigma_{rep,3} \\ \vdots \\ \sigma_{rep,3} \end{pmatrix} \quad (10.2)$$

We follow a slip system based approach and use the shear stress each slip system experiences. Per slip system, those are categorised in different damage collectives according to their strength. We consider randomly distributed grains and recall the probabilistic shear stress  $\tau_{i,j}(U)$ ,  $i = 1, 2, 3, 4$  and  $j = 1, 2, 3$  for a face-centered cubic crystal. Applying the calculation of shear stress for randomly oriented grains to the stress history in 10.2, we obtain 3 shear stress values for each of the 12 slip systems

$$\tau_{i,j}(U, \sigma_{rep,l}) = U n_i \cdot \sigma_{rep,l} \cdot U s_{i,j}, \quad (10.3)$$

with  $\sigma_{hist,t} \in \{\sigma_{rep,1}, \sigma_{rep,2}, \sigma_{rep,3}\}$ ,  $t = 0, 1, \dots, T$ . The calculation of shear stress of the whole loading history is calculated for each random orientation, since the orientation remains unchanged during the time. To accumulate the damage we apply the 3 loading states according to the history to the different slip systems and calculate the shear stress amplitudes, which are classified in damage collectives afterwards.

We reduce the given historical load course and apply the following:

To evaluate the load history with regards to 12 slip systems in this case, the stress amplitudes are calculated for each  $i$  and  $j$ .

As there are 3 stress scenarios  $\sigma_{rep,1}$ ,  $\sigma_{rep,2}$  and  $\sigma_{rep,3}$ , there are 3 different situations of resulting shear stress, namely  $\tau_{i,j}(U, \sigma_{rep,1})$ ,  $\tau_{i,j}(U, \sigma_{rep,2})$  or  $\tau_{i,j}(U, \sigma_{rep,3})$ .

This results in the following possible stress amplitudes for a given time point  $m$ :

$$\tau_{a,i,j}(U, \sigma_m^*) = \begin{cases} (\tau_{i,j}(U, \sigma_{rep,1}) - \tau_{i,j}(U, \sigma_{rep,2}))/2, & \text{if } \sigma_m^* = \sigma_{rep,1}, \sigma_{m-1}^* = \sigma_{rep,2} \text{ or v.v.}, \\ (\tau_{i,j}(U, \sigma_{rep,2}) - \tau_{i,j}(U, \sigma_{rep,3}))/2, & \text{if } \sigma_m^* = \sigma_{rep,2}, \sigma_{m-1}^* = \sigma_{rep,3} \text{ or v.v.}, \\ (\tau_{i,j}(U, \sigma_{rep,1}) - \tau_{i,j}(U, \sigma_{rep,3}))/2, & \text{if } \sigma_m^* = \sigma_{rep,1}, \sigma_{m-1}^* = \sigma_{rep,3} \text{ or v.v.} \end{cases}$$

## Microscopic Damage Accumulation Models

### 10. Probabilistic Damage Accumulation and Rainflow Counting

<b>Algorithmus 6</b> : Reduce History for Random Rainflow Counting with 3 Load States	
<b>Data</b> : $\sigma_{hist}$ ( $T + 1 \times 3 \times 3$ ) tensor with $\sigma_{hist,m} \in \{\sigma_{rep,1}, \sigma_{rep,2}, \sigma_{rep,3}\}$ $\forall m \in \{0, 1, \dots, T\}$ , Slip Plane Normals $n_i$ , Slip Systems $s_{i,j}$ , $i = 1, 2, 3, 4, j = 1, 2, 3$ , orientation $U$	
<b>Result</b> : $\sigma^*$ ( $T' \times 3 \times 3$ ) tensor containing the reduced stress history	
<b>for</b>	<i>all slip planes</i> $i = 1, 2, 3, 4$ <b>do</b>
	<b>for</b> <i>all slip systems</i> $j = 1, 2, 3$ <b>do</b>
1	Let $\tau_{a,i,j}(U, \sigma_{hist,m}) := \tau_{i,j}(U, \sigma_{hist,m}) -$ $\tau_{i,j}(U, \sigma_{hist,m-1})$ <b>for</b> <i>all changing points</i> $m = 1, \dots, T$ <b>do</b>
2	<b>if</b> $\text{sgn}(\tau_{a,i,j}(U, \sigma_{hist,m}) \cdot \tau_{a,i,j}(U, \sigma_{hist,m+1})) == +1$ <b>then</b>
	Delete $\sigma_{hist,m}$ ;
	<b>end</b>
	<b>end</b>
	<b>end</b>
	<b>end</b>
3	Store new load history with $T'$ points as $\sigma^*$

To visualize the effect that the same loading states result in different strengths and therewith different order for each slip system, we first use stress states with

$$\|\sigma'_{rep,1}\|_F = \|\sigma'_{rep,2}\|_F = \|\sigma'_{rep,3}\|_F. \quad (10.4)$$

So we use 3 loading states with equal von Mises equivalent stress, but different levels of multiaxiality. For each slip system the stress states are ordered according to their resulting shear stress. The y-axis gives the according shear stress state being ordered ascending, which means in the example loading history that

$$\tau_{1,1}(U, \sigma_{rep,3}) < \tau_{1,1}(U, \sigma_{rep,2}) < \tau_{1,1}(U, \sigma_{rep,1}) \quad (10.5)$$

and

$$\tau_{2,1}(U, \sigma_{rep,1}) < \tau_{2,1}(U, \sigma_{rep,2}) < \tau_{2,1}(U, \sigma_{rep,3}). \quad (10.6)$$

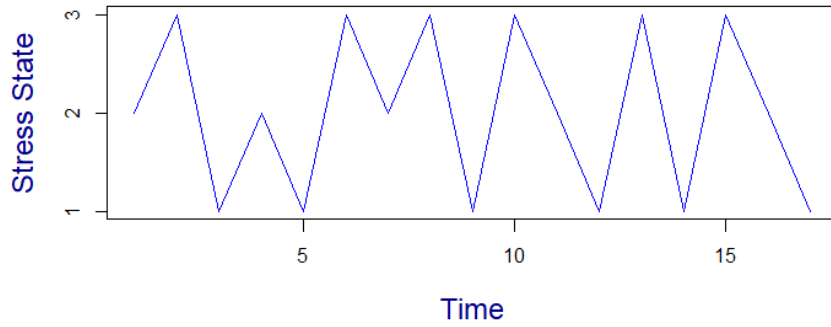
So for example at time  $t = 5$ , where  $\sigma_{hist,5} = \sigma_{rep,1}$ , we reach the stress state 3 for slip system 2 and therewith the loading state resulting in the highest shear stress, whereas for slip system 1 the applied stress leads to the lowest shear stress. Figures 10.2a and 10.2b show the stress history for those 2 different slip systems.

The level of multiaxiality and therewith the different combinations of principal stress lead to deviating results for the slip systems. Therewith even under loading states having equivalent von Mises stress there are different loading histories for each slip

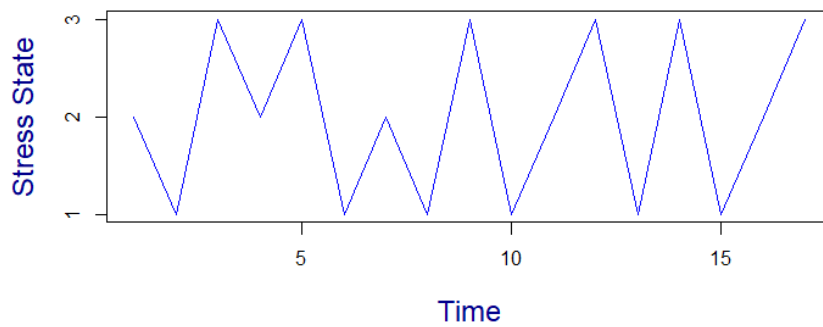
## Microscopic Damage Accumulation Models

### 10. Probabilistic Damage Accumulation and Rainflow Counting

system, as the strengths are depending on the orientation between slip system and stress tensor.



(a) Stress History for  $s_{1,1}$



(b) Stress History for  $s_{2,1}$

Figure 10.2.: Different Loading Histories per Slip System with  $T = 17$

Algorithm 2 shows the method to obtain the individual shear stress histories per slip system. In order to calculate a probabilistic damage parameter based on the loading histories for each slip system we compute probabilistic lifetime first using the stress history depending on the random orientation.

Therefore we use the stress amplitudes to calculate the amount of damage. First we use Neuber shake down as given in 3.7 to convert the elastic stress amplitudes to elastic plastical ones via  $SD(\tau_a^{el}(U)) = \tau_a^{el-pl}(U)$ . We use the Ramberg-Osgood equation given in 2.23 to obtain strain according to the given stress amplitudes and compute

$$\epsilon_a^{el-pl}(U) = RO(\tau_a^{el-pl}). \quad (10.7)$$

The probabilistic number of cycles for the given stress states can be calculated via

$$\begin{aligned} N_i(U) &= CMB^{-1}(\epsilon_a^{el-pl}(U)) \\ &= CMB^{-1}(RO(SD(\tau_a^{el}(U))))). \end{aligned} \quad (10.8)$$

## Microscopic Damage Accumulation Models

### 10. Probabilistic Damage Accumulation and Rainflow Counting

---

The loading states of the stress course are subdivided into several groups of different amplitudes and evaluated with a damage each. Therefore we use the number of cycles depending on the random orientation  $U$  as given in 10.8 and compute the number of cycles to failure according to the shear stress amplitudes for each slip system. Algorithm 7 shows the procedure to obtain the number of realized cycles using slip system based rainflow counting under random grain orientation.

With the resulting tensors of algorithm 7 we can apply the Miners rule as given in 3.4. Therefore we consider the results  $n_{rain}$  to compute a damage parameter, whose calculation is given by the following definition.

**Definition 10.1.** *Let  $U \in SO(3)$  and consider a loading history  $\sigma_{hist,M}$  with according random shear stress amplitudes denoted by  $\tau_{a,i,j}(U, \sigma_{hist,m})$ , where  $m = 1, \dots, M$  and  $M \in \mathbb{N}$ . Further consider the number of repetitions  $n_{rain,k,i,j}(U)$  in group  $k$  of the  $i$ -th slip plane in  $j$ -th direction and  $N_{k,i,j}(U)$  the calculated number of cycles to failure depending on random orientation  $U$ . The probabilistic damage of collective  $k$  can be calculated as*

$$D_{k,i,j}(U) = \frac{n_{rain,k,i,j}(U)}{N_{k,i,j}(U)}. \quad (10.9)$$

With the probabilistic damage parameter, we have the possibility to transfer the deterministic method of Rainflow counting to a random grain orientation and calculate slip system based damage parameters. We add up the part damages of all stress collectives to obtain a total damage parameter depending on the orientation  $U$ . As we consider the grain to have the same orientation during the whole loading history, the total damage is calculated for each orientation. According to **Miners rule** we are interested in the probability of the damage parameter reaching 1, i.e.

$$\begin{aligned} \mathbb{P}\left(\sum_{k=1}^M D_{k,i,j}(U) \geq 1\right) &= \mathbb{P}\left(\sum_{k=1}^M \frac{n_{rain,k,i,j}(U)}{N_{k,i,j}(U)} \geq 1\right) \\ &= 1 - \mathbb{P}\left(\sum_{k=1}^M \frac{n_{rain,k,i,j}(U)}{N_{k,i,j}(U)} < 1\right), \end{aligned} \quad (10.10)$$

respectively, taking into account all 12 slip systems at the same time,

$$\mathbb{P}\left(\max_{i,j} \left(\sum_{k=1}^M D_{k,i,j}(U)\right) \geq 1\right) = 1 - \mathbb{P}\left(\max_{i,j} \left(\sum_{k=1}^M \frac{n_{rain,k,i,j}(U)}{N_{k,i,j}(U)}\right) < 1\right). \quad (10.11)$$

So for each slip system and stress component the number of realized cycles to a given stress amplitude is evaluated in relation to its admissible number of cycles until failure according to the Coffin-Manson Basquin equation, whereby we consider

## 10. Probabilistic Damage Accumulation and Rainflow Counting

<b>Algorithmus 7</b> : Probabilistic Rainflow Counting	
<b>Data</b> :	$\sigma_{hist}^*$ ( $T' + 1 \times 3 \times 3$ ) tensor with $\sigma_m^* \in \{\sigma_{rep,1}, \sigma_{rep,2}, \sigma_{rep,3}\}$ $\forall m \in \{0, 1, \dots, T\}$ , Slip Plane Normals $n_i$ , Slip Systems $s_{i,j}$ , $i = 1, 2, 3, 4, j = 1, 2, 3$ , Number of Grid Points for Euler Angles $N_a$
<b>Result</b> :	$n_{rain}$ ( $3 \times 3 \times 4$ ) tensor containing the rainflow counts of 3 stress states for a fcc crystal (12 slip systems), $N$ ( $3 \times 3 \times 4$ ) tensor containing the rainflow counts
1	Initialize $I := [0, 2\pi] \times [0, 2\pi] \times [0, \pi]$ ;
2	Set number of grid points $N_q := (N_a - 1)^3$ ;
3	Initialize grid points $x_1, \dots, x_{N_q} \in I$ for Euler angle discretization;
4	Initialize a $N_q \times 3 \times 3 \times 4$ tensor $n_{rain} := 0$ ;
5	Initialize a $N_q \times 3 \times 3 \times 4$ tensor $N := 0$ ;
	<b>for</b> all grid points $x_l, l = 1, \dots, N_q$ <b>do</b>
6	Set Euler angles $(\varphi_1, \varphi_2, \theta) := x_l$ ;
7	Compute rotation matrix $U(\varphi_1, \varphi_2, \theta)$ ;
	<b>for</b> all slip planes $i = 1, 2, 3, 4$ <b>do</b>
	<b>for</b> all slip systems $j = 1, 2, 3$ <b>do</b>
8	Sort shear stress amplitudes according to size, such that $\tau_{aI} :=  \tau_{i,j}(U, \sigma_{rep,1}) - \tau_{i,j}(U, \sigma_{rep,3}) $ , $\tau_{aII} :=  \tau_{i,j}(U, \sigma_{rep,1}) - \tau_{i,j}(U, \sigma_{rep,2}) $ and $\tau_{aIII} :=  \tau_{i,j}(U, \sigma_{rep,2}) - \tau_{i,j}(U, \sigma_{rep,3}) $ with $\tau_{aI} \geq \tau_{aII} \geq \tau_{aIII}$ ;
	<b>for</b> all changing points $m = 1, \dots, T$ <b>do</b>
9	Calculate shear stress amplitudes $\tau_{a,i,j}(U, \sigma_m^*) := \tau_{i,j}(U, \sigma_m^*) - \tau_{i,j}(U, \sigma_{m-1}^*)$ ;
10	<b>if</b> $\tau_{a,i,j}(U, \sigma_m^*) == \tau_{aI}(U)$ <b>then</b>
	$n_{rain,1,i,j} := n_{rain,1,i,j} + 1$ ;
	<b>else if</b> $\tau_{a,i,j}(U, \sigma_m^*) == \tau_{aII}(U)$ <b>then</b>
	$n_{rain,2,i,j} := n_{rain,2,i,j} + 1$ ;
	<b>else</b>
	$n_{rain,3,i,j} := n_{rain,3,i,j} + 1$ ;
	<b>end</b>
	<b>end</b>
11	$N_{1,i,j,l} := CMB^{-1}(RO(SD(\tau_{aI}(U))))$ ;
12	$N_{2,i,j,l} := CMB^{-1}(RO(SD(\tau_{aII}(U))))$ ;
13	$N_{3,i,j,l} := CMB^{-1}(RO(SD(\tau_{aIII}(U))))$ ;
	<b>end</b>
	<b>end</b>
	<b>end</b>

## Microscopic Damage Accumulation Models

### *10. Probabilistic Damage Accumulation and Rainflow Counting*

---

random orientation of grains. Once the sum of all groups reaches a value of 1, hundred percent of allowed cycle numbers is exploited and the component is considered to fail.

We are interested in the distribution of the damage parameter, especially in the intensity of change during the loading history. As noticeable, the damage parameter changes during time for each slip system, as  $n_{rain,k,i,j}(U)$  and  $N_{k,i,j}(U)$  depend on the number of cycles. With algorithm 7 the probabilistic damage parameters for arbitrary loading histories can be generated using again discretization of Euler angles. Please note that the resulting values are afterwards weighted according to the Haar measure, similar to algorithm 4.

The following we are looking at the different distributions of damage parameters depending on  $\sigma_{hist,m}$  where  $m = 1, \dots, M$  and compare them after different numbers of cycles. Therefore we subdivide the loading history into several time periods to see the development of the damage parameter.

To obtain significant damage we set the stress states as follows:

$$\begin{aligned} \sigma_{rep,1} &= \begin{pmatrix} 1.329531 & 0 & 0 \\ 0 & -0.6647655 & 0 \\ 0 & 0 & -0.6647655 \end{pmatrix}, \\ \sigma_{rep,2} &= \begin{pmatrix} -558.41202 & 363.574605 & 20.831985 \\ 181.80920 & 279.375863 & -2.377382 \\ -10.02646 & 3.689832 & -333.162072 \end{pmatrix}, \\ \sigma_{rep,3} &= \begin{pmatrix} -2363.1118 & -17.92722 & 1168.7057 \\ 165.6428 & 1258.84897 & 354.2381 \\ -560.4561 & 390.94992 & -1127.2400 \end{pmatrix}. \end{aligned} \quad (10.12)$$

We consider a loading history with Time  $T = 30$ , which is sampled, and stop at times  $t = 10, 20, 30$ . First we look at the damage parameter at time  $t = 10$  for 2 different slip systems. Obviously, the 2 densities differ slightly already at this time, as the loading states have different impacts on the damage parameter of each slip system.

## Microscopic Damage Accumulation Models

### 10. Probabilistic Damage Accumulation and Rainflow Counting

---

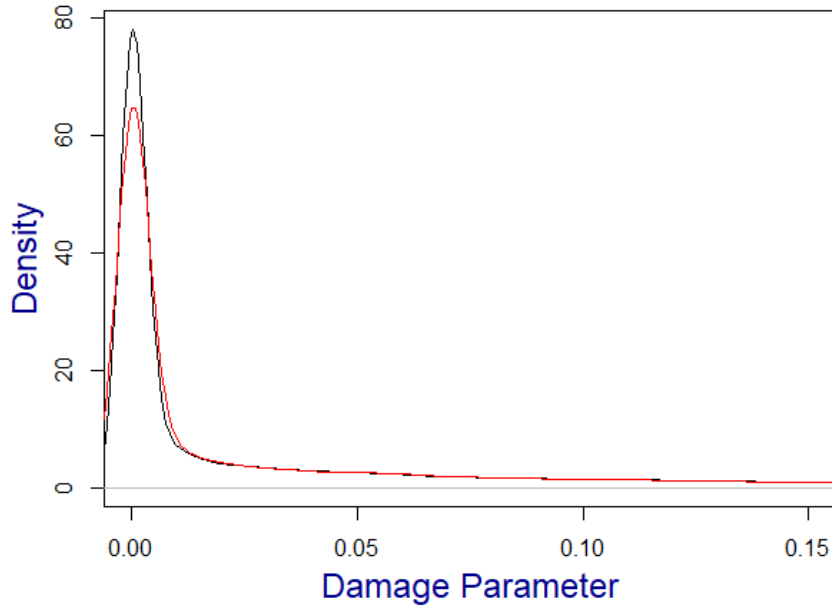


Figure 10.3.: Densities of Damage Parameter at  $t = 10$  - 2 Slip Systems

Figure 10.3 shows the 2 densities. The damage parameters are much lower than the threshold of 1, since there are only 5 cycles that have been repeated combined with sufficiently low stress states.

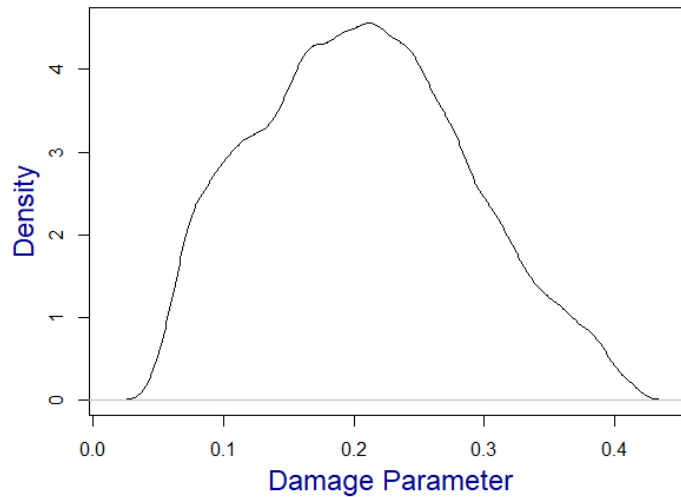


Figure 10.4.: Density of Maximum Parameter at  $t = 10$

The maximum parameter  $\max_{i,j} \left( \sum_{k=1}^M \frac{n_{rain,k,i,j}(U)}{N_{k,i,j}(U)} \right)$  scatters much wider as we notice on figure 10.4. The width of the density is significantly higher than the one of  $\sum_{k=1}^M \frac{n_{rain,k,i,j}(U)}{N_{k,i,j}(U)}$ . The scatter and right shift of damage parameter values occurs

# Microscopic Damage Accumulation Models

## *10. Probabilistic Damage Accumulation and Rainflow Counting*

---

due to the fact that we maximize over slip systems for each rotation.

We focus on the maximum damage parameter, as we are interested in the slip system experiencing the maximum damage during loading course, due to the fact that this is the critical one.

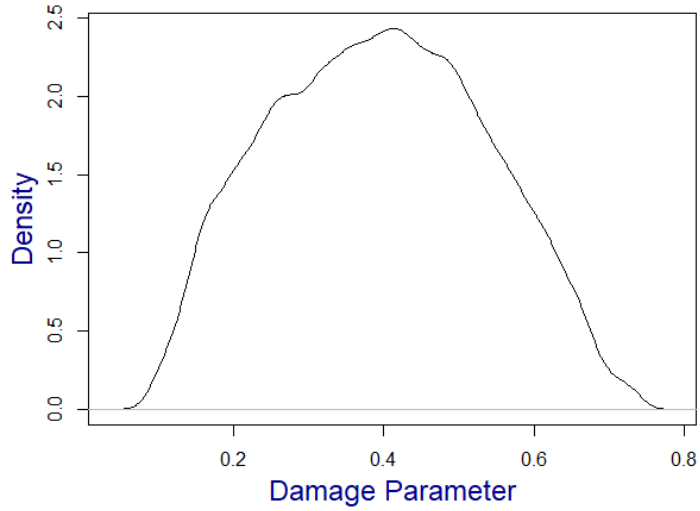


Figure 10.5.: Density of Maximum Parameter at  $t = 20$

In figure 10.5 we can see the density of the maximum damage parameter after 20 loading states. The shape looks similar, the function is shifted to the right, as the higher number of cycles causes a higher amount of damage.

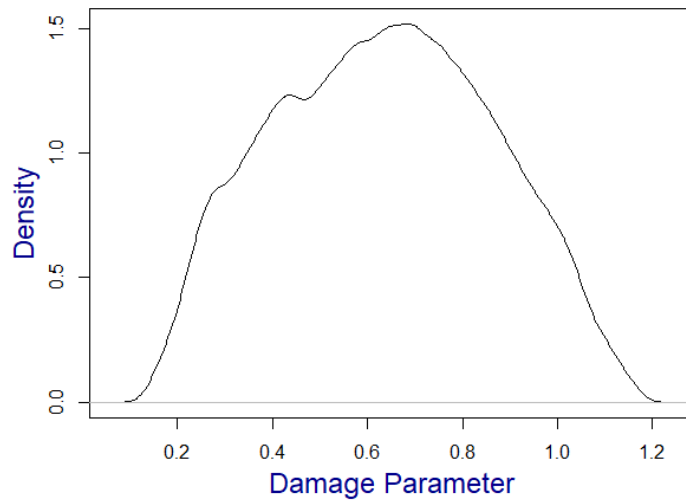


Figure 10.6.: Density of Maximum Parameter at  $t = 30$

## Microscopic Damage Accumulation Models

### *10. Probabilistic Damage Accumulation and Rainflow Counting*

---

Over the period until  $t = 40$  we notice the same effects. For this period we have

$$\begin{aligned} \mathbb{P}\left(\max_{i,j}\left(\sum_{k=1}^M D_{k,i,j}(U)\right) \geq 1\right) &= 1 - \mathbb{P}\left(\max_{i,j}\left(\sum_{k=1}^M \frac{n_{rain,k,i,j}(U)}{N_{k,i,j}(U)}\right) < 1\right) \\ &= 0.27. \end{aligned} \quad (10.13)$$

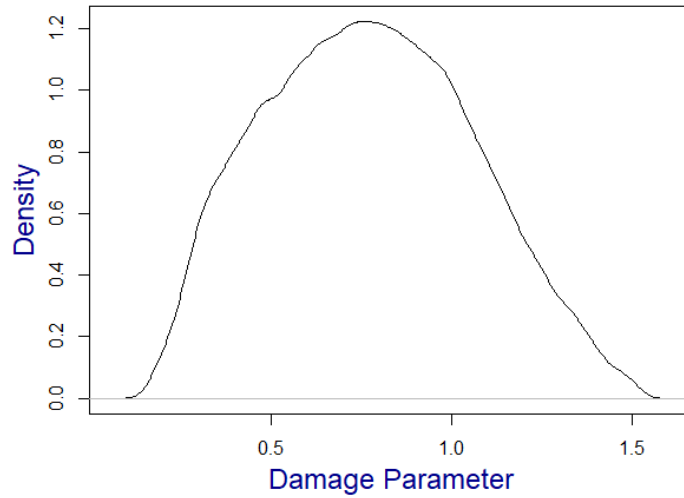


Figure 10.7.: Density of Maximum Parameter at  $t = 40$

With this procedure, we have the possibility to calculate probabilistic damage parameter for arbitrary loading histories to make an assumption on the amount of damage for given stress states. Therewith we can evaluate the course of loading states with respect to their damage and make estimations on their possible damage and the failure of the component.

## **11. Conclusion and Outlook**

In this thesis, we have shown, that it is possible to model LCF life, using an approach, which is based on the physical damage mechanisms and the material characteristics. We have introduced a probabilistic LCF life model for single grains, which uses the assumption, that the scatter in LCF life results from the scatter of shear stress, acting on the randomly oriented slip systems.

With the model, it is possible to compute LCF lifetime distributions also for loading states with different levels of multiaxiality. We have shown, that the level of multiaxiality has an impact on the lifetime, the scatter increases and the mean tends to lower values.

A method for anisotropic elasticity has been introduced. For those lifetime distributions we have seen, that the means are lower and the scatter is larger, in comparison to the isotropic ones.

We have presented two approaches to enlarge the single grain life to model the crack propagation. First, we used a cell model to describe the crack percolation within polycrystalline material. Therewith, it was possible to compute the probability of failure analytically for varying amounts and sizes of grains and for different critical crack lengths. Additionally, a Voronoi polycrystal model was introduced.

In chapter 8, we have fitted the parameters of the analytical percolation model to real LCF life data, using a maximum likelihood method. We have seen, that the models do reflect the scatter of experimental data appropriately and that the quality of estimation differs for different input parameters.

The analytical percolation model has been transferred to the geometry of a bladed disk. We have shown an exemplary calculation of cumulative hazard for a chosen stress state after different numbers of loading cycles.

We have presented an approach for a probabilistic damage accumulation and a Rain-flow counting method, where multiaxial loadings states can also be considered. A procedure for arbitrary loading histories with 3 different stress states was introduced. We have seen the change of the distribution of a probabilistic damage parameter, depending on the number of cycles. Therewith, we can evaluate the course of loading

## Microscopic Damage Accumulation Models

### *11. Conclusion and Outlook*

---

states with respect to their damage and can make assumptions on the failure of a component.

It would be possible to combine the presented models with a thermo-mechanical fatigue model, which are mostly based on an empirical approach. A more detailed investigation and comparison between the analytical and the Voronoi model would also be interesting.

## **Bibliography**

- 1 3. Ausgabe. *FKM-Richtlinie, Bruchmechanischer Festigkeitsnachweis für Maschinenbauteile*. VDMA Verlag GmbH, 2006. 1.1
- 2 M. G.Larson F. Bengzon. *The Finite Element Method: Theory, Implementation and Applications*. Springer, 2013. 9
- 3 J. Rösler H. Harders M. Bäker. *Mechanisches Verhalten der Werkstoffe*. Teubner, 2006. 1.1, 2.2, 2.2.1, 2.2.3.2, 3, 4
- 4 M. A. Meggiolaro J. T. P. de Castro H. Wu. *Invariant-Based and Critical-Plane Rainflow Approaches for Fatigue Life Prediction under Multiaxial Variable Amplitude Loading*. 3rd International Conference on Material and Component Performance under Variable Amplitude Loading, VAL2015, 2015. 3.3.1.1
- 5 J.B. de Jonge. *The Analysis of Load-Time Histories by Means of Counting Methods, Helicopter Fatigue Design Guide*. AGARDograph No 292, Advisory Group for Aerospace Research and Development, 1983. 3.3.1
- 6 J. Elstrodt. *Maß- und Integrationstheorie*. Springer, 2011. 4.1, 4.7, 4.8, 4.1, 4.9, 4.10, A.1, A.2
- 7 M. Matsuishi T. Endo. *Fatigue of Metals Subjected to Varying Stress*. Japan Soc. Mech. Engineering, 1968. 3.3.1
- 8 B. Engel. *Einfluss der lokalen Kornorientierung auf das Verformungs- und Ermüdungsverhalten von Nickelbasis Superlegierungen*. Technische Universität Kaiserslautern, 2018. 1.1, 2.3, 3.2, 3.7, 3.8, 3.9, 3.10, 3.11, 3.12, 7.23, 8.3
- 9 B. Fedelich. *A stochastic theory for the problem of multiple surface crack coalescence*. International Journal of Fracture - Vol. 91, 1998. 1.1
- 10 P. Frey. *Numerical simulation of complex PDE problems*. University of Chile, 2008. A.1
- 11 R.I. Stephens A. Fatemi R.R. Stephens H.O. Fuchs. *Metal Fatigue in Engineering*. John Wiley Sons, Inc, 2001. 1.1

# Microscopic Damage Accumulation Models

## *Bibliography*

---

- 12** L. Mäde S. Schmitz T. Beck H. Gottschalk. *Combined notch and size effect modeling in a local probabilistic approach for LCF*. Computational Materials Science 142, 2018. 1.1
- 13** S. Schmitz T. Seibel T. Beck G. Rollmann R. Krause H. Gottschalk. *A Probabilistic Model for LCF*. Computational Material Science 79, 2013. 1.1
- 14** A. Ern J.-L. Guermond. *Theory and Practice of Finite Elements*. Springer, 2004. 9
- 15** P. R. Halmos. *Measure Theory*. Springer Science+Business Media, LLC, 1970. 4.1
- 16** R. F. P. Hartmann. *Lösen von linearen Rekursionsgleichungen*. Technische Universität Clausthal, 2007. 7.1.1
- 17** J. Böhm K. Heckel. *Die Vorhersage der Dauerschwingfestigkeit unter Berücksichtigung des statistischen Größeneinflusses*. Journal of Materials Technology, 1982. 1.1
- 18** R. Herzog. *Optimale Steuerung partieller Differentialgleichungen*. TU Chemnitz, 2011. A.1
- 19** G. Härtler. *Statistik für Ausfalldaten*. Springer-Verlag Berlin Heidelberg, 2016. 1.1, 6
- 20** T. Theobald S. Ilman. *Einführung in die computerorientierte Mathematik mit Sage*. Springer Spektrum, 2016. 4.2, 4.14
- 21** K. Jänich. *Topologie*. Springer, 2001. A.1
- 22** S.J. Maddox. *Fatigue Strength of Welded Structures*. Abington Publ. Cambridge, 1991. 3.3.1
- 23** M.A. Miner. *Cumulative Damage in Fatigue*. J. Appl. Mech. (ASME) 12 / 3, 1945. 3.3.1
- 24** B. Bollobás O. Riordan. *Percolation*. Cambridge University Press, 2006. 7.1
- 25** E. Castillo A. Fernandez-Canteli J.R. Ruiz-Tolosa J. M. Sarabia. *Statistical Models for Analysis of Fatigue Life of Long Elements*. Journal of Engineering Mechanics, 1990. 1.1
- 26** H. Gottschalk N. Moch T. Beck B. Engel S. Schmitz. *Von Mikroskopischen Modellen der Schadensakkumulation zur Ausfallwahrscheinlichkeit von Gasturbinen*. 2018. 1.1

# Microscopic Damage Accumulation Models

## *Bibliography*

---

- 27** S. Schmitz. *A Local and Probabilistic Model for Low-Cycle Fatigue*. Doctoral Dissertation, University of Wuppertal, 2014. 1.1, 6
- 28** D. Gross T. Seelig. *Bruchmechanik*. Springer-Verlag Berlin Heidelberg, 2007. 1.1, 2.2, 3, 4
- 29** T. Seibel. *Influence of specimen size and grain orientation on the LCF crack initiation life of a Ni-based superalloy*. RWTH Aachen University 2014, Schriften des Forschungszentrums Jülich : Reihe Energie Umwelt, 2014. 3.9, 3.11
- 30** A. Steger. *Diskrete Strukturen - Band 1: Kombinatorik, Graphentheorie, Algebra, 2. Auflage*. Springer-Verlag Berlin Heidelberg New York, 2007. 4.2
- 31** L. Tartar. *An Introduction to Sobolev Spaces and Interpolation Spaces*. Springer, 2007. A.1
- 32** I. Babuska S. Sawlan M. Scavino B. Szabo R. Tempone. *Spatial Poisson processes for fatigue crack initiation*. Elsevier B. V., 2018. 1.1
- 33** S. Torquato. *Random Heterogeneous Materials - Microstructure and Macroscopic Properties*. Springer, 2002. 7
- 34** O. Hertel M. Vormwald. *Statistical and geometrical size effects in notched members based on weakest-link and short-crack modelling*. Engineering Fracture Mechanics, 2012. 1.1
- 35** M. W. Brown C. H. Wang. *Life Prediction Techniques for Variable Amplitude Multiaxial Fatigue—Part 1: Theories*. Journal of Engineering Materials and Technology, 1996. 3.3.1.1

## **A. Appendix**

## A.1. Further Definitions

**Definition A.1** (3.7, [6]). *A function  $f : G \rightarrow \mathbb{K}$  is left uniformly continuous, if  $\forall \epsilon > 0 \exists V \in \mathcal{V}$ , such that  $|f(x) - f(y)| < \epsilon$ ,  $x, y \in G$  with  $x^{-1}y \in V$ , so with  $|f(x) - f(xv)| < \epsilon \forall x \in G, v \in V$ . If  $\forall \epsilon > 0 \exists V \in \mathcal{V}$ , such that  $|f(x) - f(y)| < \epsilon$ ,  $x, y \in G$  with  $yx^{-1} \in V$ , so with  $|f(x) - f(vx)| < \epsilon \forall x \in G, v \in V$ ,  $f$  is called right uniformly continuous.*

**Theorem A.2** (3.11, [6]). *Let  $\Gamma$  be a locally compact Hausdorff topological group. There exists a left invariant positive linear form  $I : C_C(\Gamma) \rightarrow \mathbb{K}$ ,  $I \neq 0$ , and  $I$  is uniquely determined except for a positive factor.  $I$  is called left Haar integral on  $C_C(\Gamma)$ .*

**[Proof]** First we show existence: Let  $f, g \in C_C^+(\Gamma)$ ,  $g \neq 0$ . Then  $V := \{g > \frac{1}{2}\|g\|_\infty\}$  is a non-empty open set. There exists a finite number of  $x_1, \dots, x_m \in \Gamma$ ,  $m \in \mathbb{N}$ , with  $\text{supp } f \subset \bigcup_{k=1}^m x_k V$ , by this

$$f \leq 2 \left( \frac{\|f\|_\infty}{\|g\|_\infty} \right) \sum_{k=1}^m g \circ L(x_k^{-1}) \quad (\text{A.1})$$

Therewith it holds that

$$f \leq \sum_{k=1}^m c_k g \circ L(x_k^{-1}), \quad (\text{A.2})$$

$c_1, \dots, c_m \geq 0$ . It follows for each positive left invariant linear form  $J : C_C(\Gamma) \rightarrow \mathcal{K}$ ,  $J \neq 0$ , that

$$J(f) \leq \sum_{k=1}^m c_k J(g), \quad (\text{A.3})$$

therewith  $\sum_{k=1}^m c_k \geq \frac{J(f)}{J(g)}$ . Now let  $(f : g)$  be the infimum of all sums  $\sum_{k=1}^m c_k$  of all coefficients  $c_1, \dots, c_m$  in inequations of type (A.2). The form  $(f : g)$  has the following properties:

1.  $(f \circ L(y) : g) = (f : g)$ ,  $y \in \Gamma$ ,
2.  $(\lambda f : g) = \lambda (f : g)$ ,  $\lambda \geq 0$ ,
3.  $(f_1 + f_2 : g) \leq (f_1 : g) + (f_2 : g)$ ,  $f_1, f_2 \in C_C^+(\Gamma)$ ,
4.  $(f : g) \geq \frac{\|f\|_\infty}{\|g\|_\infty}$ ,
5.  $(f : h) \leq (f : g)(g : h)$ ,  $h \in C_C^+(\Gamma), h \neq 0$ ,
6.  $\frac{1}{(h:f)} \leq \frac{(f:g)}{(h:g)} \leq (f : h)$ ,  $f, g, h \in C_C^+(\Gamma) \setminus \{0\}$ .

# Microscopic Damage Accumulation Models

## A. Appendix

---

Properties 1. – 3. are resulting from the definition of  $(f : g)$ . For property 4 we consider (A.2) and obtain  $\|f\|_\infty \leq \sum_{k=1}^m c_k \|g\|_\infty$ , therewith  $\sum_{k=1}^m c_k \geq \frac{\|f\|_\infty}{\|g\|_\infty}$ . To obtain 5. let  $x_1, \dots, x_m \in \Gamma$  and  $c_1, \dots, c_m \geq 0$  as per (A.2) and  $y_1, \dots, y_n \in \Gamma$ ,  $d_1, \dots, d_n \geq 0$  according to  $g, h$  such that  $g \leq \sum_{l=1}^n d_l h \circ L(y_l^{-1})$ . We use (A.2) and use the last inequality to obtain

$$f \leq \sum_{k=1}^m \sum_{l=1}^n c_k d_l h \circ L((x_k y_l)^{-1}) \quad (\text{A.4})$$

and therewith  $(f : h) \leq \sum_{k=1}^m c_k \sum_{l=1}^n d_l$ . Computing the infimum on the right side of the inequality results in 6. and 6. follows directly, noting that the denominators are positive, since  $f, g, h \neq 0$ . The further approach yields in reducing the support of  $g$  to identity element  $e$  and at the same time control  $(f : g)$ . Therefore we determine a comparison function  $f_0 \in C_C(\Gamma)$ ,  $f_0 \neq 0$  and consider

$$I_g(f) := \frac{(f : g)}{(f_0 : g)}, \quad (\text{A.5})$$

$f, g \in C_C^+(\Gamma)$ ,  $g \neq 0$ . With properties 1. – 3. we obtain

$$\begin{aligned} I_g(f \circ L(y)) &= I_g(f), \quad y \in \Gamma \\ I_g(\lambda f) &= \lambda I_g(f), \quad \lambda \geq 0 \\ I_g(f_1 + f_2) &\leq I_g(f_1) + I_g(f_2), \quad f_1, f_2 \in C_C^+(\Gamma) \end{aligned} \quad (\text{A.6})$$

and 7. yields

$$I_g(f) \in \left[ \frac{1}{(f_0 : f)}, (f : f_0) \right], \quad (\text{A.7})$$

$f \neq 0$ . We consider  $I_g(f)$  to approximate  $I(f)$ . For all  $f_1, f_2 \in C_C^+(\Gamma)$  and  $\epsilon \geq 0 \exists V \in \mathcal{U}$ ,<sup>5</sup> such that

$$I_g(f_1) + I_g(f_2) \leq I_g(f_1 + f_2) + \epsilon \quad (\text{A.8})$$

for all  $g \in C_C^+(\Gamma)$ ,  $g \neq 0$  and  $\text{supp } g \subset V$ . To show this let  $K := \text{supp}(f_1 + f_2)_C^+(\Gamma)$  and  $h_C^+(\Gamma)$  with  $h|_K = 1$ . Further let  $F := f_1 + f_2 + \delta h$  with  $\delta > 0$  sufficiently small, such that  $2\delta(h : f_0) < \frac{\epsilon}{2}$ . For  $j = 1, 2$  let

$$\varphi_j(x) := \begin{cases} \frac{f_j(x)}{F(x)}, & \text{for } x \in \{F > 0\} \\ 0, & \text{for } x \in K^C. \end{cases} \quad (\text{A.9})$$

Therewith  $\varphi_1, \varphi_2$  are well-defined, since  $K \subset \{F > 0\}$  and  $\varphi_1(x) = \varphi_2(x) = 0$  for all  $x \in K^C \cap \{F > 0\}$ . Both functions are continuous, as they are continuous on open sets  $\{F > 0\}$  and  $K^C$ . Therewith it holds that  $\varphi_1, \varphi_2 \in C_C^+(\Gamma)$ ,  $0 \leq \varphi_1 + \varphi_2 \leq 1$  and  $F\varphi_j = f_j$ ,  $j = 1, 2$ . As per (4.7) are uniformly continuous from the left. We set

---

<sup>5</sup> $\mathcal{U}$  is the neighbourhood system of the identity element  $e$

# Microscopic Damage Accumulation Models

## A. Appendix

---

$0 < \eta < \frac{1}{2}$  sufficiently small, such that  $2\eta(f_1 + f_2 : f_0) < \frac{\epsilon}{2}$ . There exists a  $V \in \mathcal{U}$ , such that  $|\varphi_j(x) - \varphi_j(xv)| < \eta \forall x \in \Gamma, v \in V, j = 1, 2$ . Now let  $g \in C_C^+(\Gamma), g \neq 0$ ,  $\text{supp } g \subset V$  and  $x_1, \dots, x_m \in \Gamma, c_1, \dots, c_m \geq 0$ , such that

$$F \leq \sum_{k=1}^m c_k g \circ L(x_k^{-1}). \quad (\text{A.10})$$

With  $g \circ L(x_k^{-1}) \neq 0$  it holds that  $x \in x_k V$ , and  $\varphi_j(x) \leq \varphi_j(x_k) + \eta$ . Thus,

$$f_j(x) = \varphi_j(x)F(x) \leq \sum_{k=1}^m c_k (\varphi_j(x_k) + \eta) g(x_k^{-1}x), \quad (\text{A.11})$$

$x \in \Gamma, j = 1, 2$ . Summing up of the resulting inequalities for  $(f_1 : g), (f_2 : g)$  yields

$$(f_1 : g) + (f_2 : g) \leq \sum_{k=1}^m c_k (\varphi_1(x_k) + \varphi_2(x_k) + 2\eta) \leq \sum_{k=1}^m c_k (1 + 2\eta), \quad (\text{A.12})$$

considering  $\varphi_1 + \varphi_2 \leq 1$ . Applying (A.6) and (A.10) we obtain

$$\begin{aligned} (f_1 : g) + (f_2 : g) &\leq (F : g)(1 + 2\eta) \leq ((f_1 + f_2 : g) + \delta(h : g))(1 + 2\eta), \\ I_g(f_1) + I_g(f_2) &\leq (I_g(f_1 + f_2) + \delta I_g(h))(1 + 2\delta). \end{aligned} \quad (\text{A.13})$$

We determine  $\delta, \eta$  sufficiently and see that

$$\begin{aligned} 2\eta I_g(f_1 + f_2) &\leq 2\eta(f_1 + f_2 : f_0) < \frac{\epsilon}{2}, \\ \delta I_g(h)(1 + 2\eta) &\leq 2\delta(h : f_0) < \frac{\epsilon}{2}. \end{aligned} \quad (\text{A.14})$$

We now consider  $X := \prod_f \left[ \frac{1}{(f_0 : f), (f : f_0)} \right]$ , the product of all  $f \in C_C^+(\Gamma), f \neq 0$ . According to the theorem of Tychonoff [21, 10.1]  $X$  is compact. It follows from (A.7) that  $I_g \in X$  for all  $g \in C_C^+(X), g \neq 0$ . Now for  $V \in \mathcal{U}$  let  $F(V)$  be the closure of  $\{I_g : g \in C_C^+(\Gamma), g \neq 0, \text{supp } g \subset V\}$  in  $X$ . For  $V_1, \dots, V_n \in \mathcal{U}$   $F(V_1) \cap \dots \cap F(V_n) = F(V_1 \cap \dots \cap V_n)$ . Since  $X$  is compact, the intersection of  $F(V), V \in \mathcal{U}$ , is not empty. Let  $I \in F(V)$  for all  $V \in \mathcal{U}$ . For each  $f_1, \dots, f_n \in C_C^+(\Gamma) \setminus \{0\}, n \in \mathbb{N}, \epsilon > 0$  and  $V \in \mathcal{U}$  there exists  $g \in C_C^+(\Gamma), g \neq 0$  with  $\text{supp } g \subset V$ , such that

$$|I(f_j) - I_g(f_j)| < \epsilon, \quad (\text{A.15})$$

# Microscopic Damage Accumulation Models

## A. Appendix

---

for all  $j = 1, \dots, n$ . With properties (A.6) we obtain the following for  $I : C_C^+(\Gamma) \setminus \{0\} \rightarrow (0, \infty)$ ,  $f, f_1, f_2 \in C_C^+(\Gamma) \setminus \{0\}$ :

$$\begin{aligned} I(f \circ L(y)) &= I(f), \quad y \in \Gamma, \\ I(\lambda f) &= \lambda I(f), \quad \lambda > 0, \\ I(f_1 + f_2) &= I(f_1) + I(f_2), \\ \frac{1}{(f_0 : f)} &\leq I(f) \leq (f : f_0). \end{aligned} \tag{A.16}$$

Therewith  $I$  can be continued to a left invariant positive linear form  $I : C_C(\Gamma) \rightarrow \mathbb{K}$ . Due to (4)  $(f_0 : f_0) = 1$  and following  $I(f_0) = 1$ . Due to the last properties it holds that  $I \neq 0$ .

Now we show uniqueness: Let  $J : C_C(\Gamma) \rightarrow \mathbb{K}$  be a left Haar integral and  $f, g \in C_C^+(\Gamma)$ ,  $g \neq 0$ . It results from (A.3), i.e.  $J(f) \leq \sum_{k=1}^m c_k J(g)$ , so

$$J(f) \leq (f : g)J(g) \tag{A.17}$$

$J(g) \neq 0$ . Further let  $f \in C_C^+(\Gamma)$ ,  $\epsilon > 0$ . As  $f$  is left uniformly continuous, there exists  $U \in \mathcal{U}$ , such that  $|f(x) - f(y)| < \epsilon$  for all  $x, y \in \Gamma$  with  $x^{-1}y \in U$ . Let  $g \in C_C^+(\Gamma)$ ,  $g \neq 0$  with  $\text{supp } g \subset U$ , such that  $g(x) = g(x^{-1})$ ,  $x \in \Gamma$ . For  $x \in \Gamma$  fixed we consider  $\Gamma \rightarrow \mathbb{R}$ ,  $y \mapsto f(y)g(y^{-1}x)$ ,  $y \in \Gamma$ . For  $y^{-1}x \in U$  it holds that  $g(y^{-1}x) = 0$  and for  $y^{-1}x \in U$   $f(y) \geq f(x) - \epsilon$ . Since  $g$  is symmetric and  $J$  is left invariant,

$$\begin{aligned} J(f(y)g(y^{-1}x)) &\geq (f(x) - \epsilon)J(g(y^{-1}x)) \\ &= (f(x) - \epsilon)J(g(x^{-1}y)) \\ &= (f(x) - \epsilon)J(g), \end{aligned} \tag{A.18}$$

and

$$f(x) - \epsilon \leq \frac{J(f(y)g(y^{-1}x))}{J(g)}. \tag{A.19}$$

Function  $g$  is right uniformly continuous. Considering a  $\eta > 0$  there is  $W \in \mathcal{U}$  open with  $|g(y) - g(z)| < \eta$  for all  $y, z \in \Gamma$  and  $yz^{-1} \in W$ . Let  $K := \text{supp}(f + f_0)$ . There exists a finite number of  $y_1, \dots, y_n \in \Gamma$  and  $\varphi_1, \dots, \varphi_n \in C_C^+(\Gamma)$  with  $\sum_{k=1}^n \varphi_k|_K = 1$  and  $\text{supp } \varphi_k \subset y_k W$ ,  $k = 1, \dots, n$ . The right side of (A.19)

$$J(f(y)g(y^{-1}x)) = \sum_{k=1}^n J(f(y)\varphi_k(y)g(y^{-1}x)). \tag{A.20}$$

# Microscopic Damage Accumulation Models

## A. Appendix

---

Here  $\varphi_k(y) = 0$  for  $y_k W$  and  $y_k^{-1}x \in W y^{-1}$  for  $y \in y_k W$ , therewith  $g(y^{-1}x) \leq g(y_k^{-1}x) + \eta$ . Now let  $\gamma_k := \frac{J(f\varphi_k)}{J(g)}$ , then  $\sum_{k=1}^n \gamma_k = \frac{J(f)}{J(g)}$ . Considering (A.19) and (A.20), we obtain

$$f(x) \leq \epsilon + \sum_{k=1}^n \gamma_k (g(y_k^{-1}x) + \eta) = +\eta \frac{J(f)}{J(g)} + \sum_{k=1}^n \gamma_k g(y_k^{-1}x). \quad (\text{A.21})$$

We set  $\eta$  sufficiently small, such that  $\eta \frac{J(f)}{J(g)} < \epsilon$  and  $h \in C_C^+(\Gamma)$  with  $h|K = 1$ . Therewith

$$f(x) \leq 2\epsilon h(x) + \sum_{k=1}^n \gamma_k g(y_k^{-1}x) \quad (\text{A.22})$$

and

$$(f : g) \leq 2\epsilon(h : g) + \sum_{k=1}^n \gamma_k = 2\epsilon(h : g) + \frac{J(f)}{J(g)}. \quad (\text{A.23})$$

Dividing by  $(f_0 : g)$  yields with property 6 of  $(f : g)$  and (A.17)

$$I_g(f) = \frac{f : g}{f_0 : g} \leq 2\epsilon \frac{h : g}{f_0 : g} + \frac{J(f)}{(f_0 : g)J(g)} \leq 2\epsilon(h : f_0) + \frac{J(f)}{J(f_0)}. \quad (\text{A.24})$$

Let  $U$  be sufficiently small, such that  $|f_0(x) - f_0(y)| < \epsilon$  for all  $x, y \in \Gamma$  with  $x^{-1}y \in U$ . We can apply (A.23) to  $f_0$  instead of  $f$  and (A.17) and obtain

$$I_g(f) = \frac{f : g}{f_0 : g} \geq \frac{J(f)}{2\epsilon(h : g)J(g) + J(f_0)}. \quad (\text{A.25})$$

We now estimate  $(h : g)J(g)$  upwards. Therefore we set  $h^* \in C_C^+(\Gamma)$  with  $h^*|K = 1$  and  $\epsilon^* := (4(h^* : h)^{-1})$ . Additionally, we choose  $U$  sufficiently small, such that  $|h(x) - h(y)| < \epsilon^*$  for all  $x, y \in \Gamma$  with  $x^{-1}y \in U$ . It holds (A.23) also for  $h, h^*$  and  $\epsilon^*$  for all symmetric  $g \in C_C^+(\Gamma)$ ,  $g \neq 0$  and  $\text{supp } g \subset U$ , i.e.

$$\begin{aligned} (h : g) &\leq 2\epsilon^*(h^* : g) + \frac{J(h)}{J(g)} \\ &\leq \frac{1}{2} \frac{(h^* : g)}{(h^* : h)} + \frac{J(h)}{J(g)} \\ &\leq \frac{1}{2}(h : g) + \frac{J(h)}{J(g)}. \end{aligned} \quad (\text{A.26})$$

We obtain

$$(h : g)J(g) \leq 2J(h) \quad (\text{A.27})$$

and with (A.25)

$$I_g(f) \geq \frac{J(f)}{4\epsilon J(h) + J(f_0)}. \quad (\text{A.28})$$

# Microscopic Damage Accumulation Models

## A. Appendix

---

As per to (A.24) and (A.28) there is a  $V \in \mathcal{U}$  for each  $\delta > 0$ , such that  $|I_g - \frac{J(f)}{J(f_0)}| < \delta$  for all symmetric  $g \in C_C^+(\Gamma)$ ,  $g \neq 0$  with  $\text{supp } g \subset V$ . Therewith  $\frac{J(f)}{J(f_0)}$  is uniquely determined. ■

The definition of Sobolev spaces can be found e.g. in [31; 10; 18].

**Definition A.3** (Sobolev Space of 1st Order). *Let  $\Omega \subset \mathbb{R}^d$ . We denote the Sobolev space of order 1 by*

$$H^1(\Omega) = \{v \in L^2(\Omega), \partial_{x_i} v \in L^2(\Omega), 1 \leq i \leq d\}. \quad (\text{A.29})$$

$H^1$  is endowed with the norm

$$\langle u, v \rangle_{H^1(\Omega)} = \int_{\Omega} \left( uv + \sum_{i=1}^d \partial_{x_i} u \partial_{x_i} v \right) dx, \quad (\text{A.30})$$

and we denote the according norm by  $\|v\|_{H^1(\Omega)} = \sqrt{\langle v, v \rangle} = \left( \int_{\Omega} |u|^2 dx + \int_{\Omega} |\nabla u|^2 dx \right)^{\frac{1}{2}}$ .